Combined Cohesin-Runx1 Deficiency Synergistically Perturbs Chromatin Looping and Causes Myelodysplastic Syndromes

Yotaro Ochi[1,2], Ayana Kon[1], Toyonori Sakata[3], Masahiro M Nakagawa[1], Naotaka Nakazawa[4], Masanori Kakuta[5], Keisuke Kataoka[1], Haruhiko Koseki[6], Manabu Nakayama[7], Daisuke Morishita[8], Tatsuaki Tsuruyama[9], Ryunosuke Saiki[1], Akinori Yoda[1], Rurika Okuda[1], Tetsuichi Yoshizato[1], Kenichi Yoshida[1], Yusuke Shiozawa[1], Yasuhito Nannya[1], Shinichi Kotani[1,2], Yasunori Kogure[1], Nobuyuki Kakiuchi[1], Tomomi Nishimura[1], Hideki Makishima[1], Luca Malcovati[10,11], Akihiko Yokoyama[12], Kengo Takeuchi[13], Eiji Sugihara[14], Taka-aki Sato[14], Masashi Sanada[15], Akifumi Takaori-Kondo[2], Mario Cazzola[10,11], Mineko Kengaku[4,16], Satoru Miyano[5], Katsuhiko Shirahige[3], Hiroshi I Suzuki[17*], and Seishi Ogawa[1,18,19*]

[1]Department of Pathology and Tumor Biology, Graduate School of Medicine, Kyoto University, Kyoto, Japan

[2]Department of Hematology and Oncology, Graduate School of Medicine, Kyoto University, Kyoto, Japan

[3]Laboratory of Genome Structure and Function, Research Division for Quantitative Life Sciences, Institute for Quantitative Biosciences, The University of Tokyo, Tokyo, Japan

[4]Institute for Integrated Cell-Material Sciences (WPI-iCeMS), Kyoto University, Kyoto, Japan

[5]Laboratory of DNA Information Analysis, Human Genome Center, Institute of Medical Science, The University of Tokyo, Tokyo, Japan

[6]Laboratory for Developmental Genetics, RIKEN Center for Integrative Medical Sciences, Yokohama, Japan

[7]Laboratory of Medical Omics Research, Department of Frontier Research and Development, Kazusa DNA Research Institute, Kisarazu, Japan

[8]Chordia Therapeutics Inc., Kanagawa, Japan

[9]Department of Drug and Discovery Medicine, Pathology Division, Graduate School of Medicine, Kyoto University, Kyoto, Japan

[10]Department of Molecular Medicine, University of Pavia, Pavia, Italy

[11]Department of Hematology Oncology, Fondazione IRCCS Policlinico San Matteo, Pavia, Italy

[12]Tsuruoka Metabolomics Laboratory, National Cancer Center, Yamagata, Japan

[13]Pathology Project for Molecular Targets, Cancer Institute, Japanese Foundation for Cancer Research, Tokyo, Japan

[14]Research and Development Center for Precision Medicine, University of Tsukuba, Ibaraki, Japan

[15]Department of Advanced Diagnosis, Clinical Research Center, National Hospital Organization Nagoya Medical Center, Nagoya, Japan

[16]Graduate School of Biostudies, Kyoto University, Kyoto, Japan

[17]David H. Koch Institute for Integrative Cancer Research, Massachusetts Institute of Technology, Cambridge, MA, USA

[18]Institute for the Advanced Study of Human Biology (WPI-ASHBi), Kyoto University, Kyoto, Japan

[19]Department of Medicine, Centre for Haematology and Regenerative Medicine, Karolinska Institute, Stockholm, Sweden

Running title: MDS induced by combined cohesin-Runx1 deficiency

Keywords: myelodysplastic syndrome, cohesin, chromatin loop, transcriptional pausing, leukemogenesis

***Contact information for correspondence:**

Seishi Ogawa (sogawa-tky@umin.ac.jp) and Hiroshi I Suzuki (hisuzuki-tky@umin.ac.jp).

S.O.: Department of Pathology and Tumor Biology, Graduate School of Medicine, Kyoto University F-building, Yoshida-Konoe-cho, Sakyo-ku, Kyoto 606-8501, Japan

TEL: +81-75-753-9285, FAX: +81-75-753-9282

H.I.S.: David H. Koch Institute for Integrative Cancer Research, Massachusetts Institute of Technology, 500 Main St., 76-461A, Cambridge, MA 02139, USA

TEL: +1-617-253-6457

Conflict of interest disclosure:

The authors declare no conflict of interest.

Abstract

STAG2 encodes a cohesin component and is frequently mutated in myeloid neoplasms, showing highly significant co-mutation patterns with other drivers, including *RUNX1*. However, the molecular basis of cohesin-mutated leukemogenesis remains poorly understood. Here we show a critical role of an interplay between Stag2 and Runx1 in the regulation of enhancer-promoter looping and transcription in hematopoiesis. Combined loss of Stag2 and Runx1, which co-localize at enhancer-rich, Ctcf-deficient sites, synergistically attenuates enhancer-promoter loops, particularly at sites enriched for RNA polymerase II and Mediator, and deregulates gene expression, leading to myeloid-skewed expansion of hematopoietic stem/progenitor cells (HSPCs) and myelodysplastic syndromes (MDS). Attenuated enhancer-promoter loops in Stag2/Runx1-deficient cells are associated with downregulation of genes with high basal transcriptional pausing, which are important for regulation of HSPCs. Down-regulation of high-pausing genes is also confirmed in STAG2/cohesin-mutated primary leukemia samples. Our results highlight a unique STAG2/RUNX1 interplay in gene regulation and provide insights into cohesin-mutated leukemogenesis.

Significance

We demonstrate a critical role of an interplay between Stag2 and a master transcription factor of hematopoiesis, Runx1, in MDS development, and further reveal their contribution to regulation of high-order chromatin structures, particularly enhancer-promoter looping, and the link between transcriptional pausing and selective gene dysregulation caused by cohesin deficiency.

Introduction

Myelodysplastic syndromes (MDS) and related disorders are heterogeneous groups of myeloid neoplasms showing varying degrees of cytopenia due to ineffective hematopoiesis and a high propensity to progression to acute myeloid leukemia (AML) (1). During the past two decades, a complete registry of recurrent mutational targets, or driver genes, has been identified using advanced genomics (2-4). However, the functional basis of mutations has not fully been elucidated in many of those drivers. Among these are *STAG2* and other members of the cohesin complex, including *SMC1*, *SMC3*, and *RAD21*, which are a new class of driver genes mutated in ~10% of MDS and other myeloid neoplasms with *STAG2* being most frequently affected (5-7). Most mutations in *STAG2* are nonsense or frameshift, leading to protein truncation and loss-of-function (5). Involved in different cellular processes, such as sister chromatid cohesion during cell division and DNA repair (8), cohesin is also implicated in transcriptional control (9-12), possibly through regulating high-order chromatin structures (13). However, it is largely unknown how mutated cohesin contributes to myeloid leukemogenesis. In this study, through the analysis of interactions of gene mutations in a large cohort of MDS followed by the analysis of relevant mouse models, we show a strong functional interplay between Stag2 and Runx1 in the regulation of chromatin structures and gene expression in the hematopoietic compartment, providing novel insight into the leukemogenic mechanism of a unique subset of myeloid neoplasms characterized by *STAG2* and mutually highly correlated mutations.

Results

Genetic interaction of mutations in human MDS/AML

In MDS/AML, *STAG2* mutations are rarely seen as a solitary mutation, but almost always accompanied by other mutations, frequently involving *SRSF2, RUNX1, ASXL1, CEBPA, BCOR, EZH2, IDH2,* and *NRAS* (2-4). To see this in more detail, we investigated significant mutational correlations in MDS and related myeloid neoplasms, using in-house or publicly available mutation data sets from 3,047 cases with MDS (n=2,498) and related myeloid neoplasms (n=549) (2,3,14-18). After exhaustively evaluating correlations across all pair-wise combinations among 42 major drivers commonly mutated in MDS/AML, we detected a number of significant positive and negative correlations (**Fig. 1A, and Supplementary Tables S1-3**). Remarkably, the top-ranked 6 correlations were exhausted by all possible pair-wise combinations among four genes, *STAG2, RUNX1, SRSF2*, and *ASXL1* (‘*SRSA*’ genes), which are involved in gene regulation, and were

co-mutated at significantly higher frequencies than expected only by chance (**Fig. 1A-B**). One or more of these genes accounted for 31.8% (n=970) of MDS/AML, of which 346 (35.7%) had mutations in ≥2 of these genes and 75 (7.7%) and 33 (3.4%) carried mutations in three and all four genes, respectively (**Fig. 1B and Supplementary Fig. S1A-B**). Patients with ≥2 *SRSA* mutations had a significantly poor overall survival, compared with those with just one, which still negatively affected the survival (**Fig. 1C**). Numbers of other driver mutations did not differ according to the number of *SRSA* mutations, suggesting that *SRSA* combination is not just a consequence of increased total mutations (**Supplementary Fig. S2A).** No significant difference was observed in the frequency of missense vs non-sense or frameshift mutations in the *RUNX1* gene between *STAG2*-WT and mutated cases (**Supplementary Fig. S2B**). Analysis of variant allele frequency suggests that *SRSF2* mutations are acquired earlier than other 3 mutations, followed by *RUNX1* mutations and then *STAG2* and *ASXL1* mutations (**Fig. 1D and Supplementary Fig. S2C**). We also observed high frequency of converging evolution by way of 'parallel' *STAG2* mutations; multiple, as many as four, independent *STAG2*-mutated subclones were detected in 17 (22%) of 76 evaluable cases with *STAG2* mutations, of which 16 carried *RUNX1, SRSF2*, and/or *ASXL1* mutations in the major tumor population, indicating that *STAG2* mutations should confer a strong selective advantage in these mutational contexts (**Fig. 1E**). Combined, these findings suggest strong functional interactions among *SRSA* mutations in positive selection that underlie the development/progression of MDS.

Expanded HSPC pools and differentiation block in *Stag2* knockout mice

To understand the leukemogenic mechanism of *SRSA*-mutated MDS, particularly focusing on *STAG2* mutation, which showed a unique converging evolution pattern (**Fig. 1E**) and has been less studied in terms of functional consequence compared to other *SRSA* genes, we first generated a mouse model having a conditional *Stag2* knockout allele with an *Mx1-Cre* transgene (*Mx1-Cre*$^{+}$ *Stag2*$^{fl/-}$; SKO) (**Supplementary Fig. S3A-C; see Methods**). After polyinosinic-polycytidylic acid (pIpC) injection, SKO mice exhibited a slightly decreased white blood cell (WBC) with a large reduction in B-lymphocytes (B220^{+}), compared with littermate wild-type (WT) mice (*Mx1-Cre*$^{-}$ *Stag2*$^{fl/-}$) (**Fig. 2A**). While no significant changes were observed in hemoglobin level and platelet count between SKO and WT mice, SKO mice showed significantly increased red cell distribution width (RDW), suggestive of dyserythropoiesis (19) and pathological examination revealed mild tri-lineage bone marrow (BM) dysplasia and a slightly enlarged spleen with evidence of

extramedullary hematopoiesis in SKO mice (**Fig. 2A and Supplementary Fig. S3D-E**). Collectively these findings support the presence of a mild MDS-like phenotype in SKO mice, although overall survival did not differ between SKO and WT mice (**Supplementary Fig. S3F**). In BM, SKO mice had a higher frequency of $Lin^-/Sca1^+/c\text{-}Kit^+$ (LSK) cells, compared with WT littermate, where all major subfractions of LSK cells were increased (**Fig. 2B and Supplementary Fig. S4A**), indicating expanded hematopoietic stem/progenitor cell (HSPC) pools. The increase was most prominent in myeloid-biased progenitors, including multipotent progenitor (MPP)-2 ($Lin^-/c\text{-}Kit^+/Sca\text{-}1^+/CD135^-/CD150^+/CD48^+$) and MPP-3 ($Lin^-/c\text{-}Kit^+/Sca\text{-}1^+/CD135^-/CD150^-/CD48^+$), followed by LT-HSC ($Lin^-/c\text{-}Kit^+/Sca\text{-}1^+/CD135^-/CD150^+/CD48^-$) and ST-HSC ($Lin^-/c\text{-}Kit^+/Sca\text{-}1^+/CD135^-/CD150^-/CD48^-$), suggesting the presence of myeloid skewing (20). The myeloid skewing was also evident in more differentiated progenitors as evident from increased common myeloid progenitors (CMPs; $Lin^-/c\text{-}Kit^+/Sca\text{-}1^-/CD34^+/FcγR^{med}$) and granulocyte-macrophage progenitors (GMPs; $Lin^-/c\text{-}Kit^+/Sca\text{-}1^-/CD34^+/FcγR^{high}$), and decreased common lymphoid progenitors (CLPs; $Lin^-/c\text{-}Kit^{med}/Sca\text{-}1^{med}/IL\text{-}7Rα^+/Flt3^+$) (**Fig. 2C and Supplementary Fig. S4B**). Of note, SKO mice showed decreased frequencies of megakaryocyte/erythrocyte lineage-restricted progenitors (MEPs; $Lin^-/c\text{-}Kit^+/Sca\text{-}1^-/CD34^-/FcγR^{low}$) and erythroid progenitors ($Ter119^+/CD71^+$), suggesting a blocked differentiation into erythromegakaryocyte lineages (**Fig. 2C and Supplementary Fig. S4B-D**). Mature cells were also skewed to myeloid lineages with increased granulocytes/monocytes ($CD11b^+$) and decreased B-lymphocytes in the BM and spleen (**Fig. 2D and Supplementary Fig. S4E-F**). Extramedullary hematopoiesis was evident from increased frequencies of erythroid progenitors in the spleen (**Supplementary Fig. S4C-D**). In agreement with expanded HSPC pools, SKO-derived BM cells showed an enhanced clonogenicity in replating assay (**Fig. 2E**). HSCs ($CD150^+/CD48^-$ LSK cells) from SKO mice showed a decreased frequency of apoptotic cells ($Annexin^+/7\text{-}AAD^-$) and an enhanced cell cycling (S/G2/M; $Ki\text{-}67^+/Hoechst^+$) with decreased quiescent (G0; $Ki\text{-}67^-/Hoechst^-$) cells, compared with those from WT mice (**Fig. 2F-G and Supplementary Fig. S4G-H**). In competitive repopulation assay, SKO-derived cells showed enhanced chimerism within the LSK fraction, although the chimerism of SKO-derived cells was not significantly changed in total BM and even reduced in peripheral blood, particularly within lymphocytes (**Fig. 2H**). These results suggest an enhanced self-renewal and repopulation capacity of SKO-derived progenitors with a block in lymphoid differentiation.

As expected from the myeloid skewing in SKO mice, transcriptome analysis demonstrated up- and downregulation of genes implicated in myeloid and lymphoid programs in SKO, respectively, including a number of transcription factors (TFs) (**Fig. 2I-J and Supplementary Fig. S4I**). Among these, we noted the elevated expression of *Runx1* in SKO-derived LSK and CMP cells (**Fig. 2K**) (21). The following ATAC sequencing analysis (22) showed enrichment of the binding motifs of Runx1 and Gata2 in enhanced ATAC peaks and enrichment of the binding motifs of interferon regulatory factors (IRFs) in reduced ATAC peaks in SKO-derived LSK and CMP cells (**Fig. 2L-M and Supplementary Fig. S5A-C**). Furthermore, we confirmed an increased Runx1 binding to its consensus motifs in SKO cells by ChIP-seq (**Supplementary Fig. S5D**). These findings suggest upregulated expression of Runx1-regulated genes. However, interestingly, genes down-regulated in SKO-derived LSK cells showed a highly significant enrichment in genes down-regulated in *Runx1*-knockout mice (*Mx1-Cre*$^{+}$ *Runx1*$^{fl/fl}$; RKO) and vice versa (**Fig. 2N**), suggesting a functional interplay between Stag2 and Runx1, a typical *SRSA* combination.

***Stag2*/*Runx1* codeficiency induces MDS in mice**

To see the interplay between both proteins, we investigated the effects of *Stag2/Runx1* double knockout (*Mx1-Cre*$^{+}$ *Stag2*$^{fl/-}$*Runx1*$^{fl/fl}$; DKO) on hematological phenotype in transplantation setting, in which DKO- as well as single KO-derived BM cells were transplanted into lethally irradiated mice, followed by pIpC injection. Compared with single KO-transplanted mice, in which cytopenia was confined to lymphocytes (SKO and RKO) and platelets (RKO), DKO-transplanted mice exhibited more profound cytopenia (**Fig. 3A**). WBC was markedly reduced and the reduction was seen not only in lymphocytes but also in granulocytes and monocytes. Although not apparent in single-KO-transplanted mice, anemia was evident with markedly increased MCV and RDW (**Fig. 3A and Supplementary Fig. S6A**). In contrast to severely reduced peripheral blood counts, the frequency of immature BM progenitors (LSK cells) was almost doubled compared with that in single-KO-transplanted mice, where the increase was mostly explained by MPP2 and MPP3, although LT- and ST-HSC were significantly reduced compared with those in SKO-transplanted mice (**Fig. 3B-C and Supplementary Fig. S6B**). While more mature progenitors exhibited variable profiles depending on genotype, they were largely maintained in DKO-transplanted mice, except for severely reduced frequency of colony-forming unit erythroid cells (CFUe) and Ter119^{+}CD71^{+} erythroid progenitors (**Fig. 3D-F and Supplementary Fig. S6C-F**). Lineage-committed mature cells were synergistically skewed to myeloid lineages by *Stag2*/*Runx1* deletion (**Fig. 3G and**

Supplementary Fig. S6E). Prolonged clonogenicity was also observed in replating assay (**Supplementary Fig. S6G**). In competitive repopulation assay, the peripheral blood chimerism was severely impaired, even though the chimerism in the progenitor (LSK) fraction was not significantly affected, which was compatible with severe peripheral blood cytopenias (**Supplementary Fig. S6H**). Conspicuously, all mice transplanted with DKO-derived BM cells developed overt MDS mostly within a half year after pIpC injection, with a severe cytopenia and marked trilineage dysplasia, while none of the animals transplanted with SKO- or RKO-cells developed MDS, although a number of deaths were also observed in RKO-transplanted mice with no exacerbation of blood cell counts (**Fig. 3H-I and Supplementary Fig. S6I-L**). In transcriptome analysis and ATAC-seq of LSK cells, DKO-derived LSK cells showed more extensive alterations in gene expression and chromatin accessibility, compared with single-KO-derived cells; DKO cells showed a much higher number of differentially expressed genes (DEGs) and differentially enhanced or attenuated chromatin accessibility sites, compared with single-KO (**Fig. 3J-K and Supplementary Fig. S6M**). These findings in the phenotype of DKO mice further support the functional interplay between Stag2 and Runx1.

Unique binding of Stag2-cohesin and Runx1 to enhancers

To understand the molecular basis of the interplay between Stag2 and Runx1, we performed an extensive ChIP-sequencing analysis, in which genomic localization of Stag2 and other cohesin components (Stag1 and Smc1), Runx1, Ctcf, and major histone marks was investigated in WT-derived HSPCs (c-Kit$^+$ BM cells). We identified a total of 27,997 cohesin binding sites that showed signal peaks in Stag1 and/or Stag2. On the basis of relative ChIP signals for Ctcf and H3K27ac, indicative for insulator and enhancer sites, respectively, these cohesin binding sites were separated into two discrete groups showing high relative Ctcf signals (cohesin binding cluster-I (CC-I) sites) and high relative H3K27ac signals (cohesin binding cluster-II (CC-II) sites) (**Fig. 4A and Supplementary Fig. S7A-B**). Explaining most of the cohesin-binding sites (n=24,364, 87%), CC-I sites generally had comparable Stag1 and Stag2 signal intensities with discrete signal peaks and were characterized by the paucity of active histone marks (**Fig. 4A**). By contrast, accounting for only 13% (n=3,633) of all cohesin binding sites detected, CC-II sites had stronger Stag2 than Stag1 signals showing broader chromatin binding peaks (**Fig. 4A-B**). As expected from their association with high H3K27ac signals, most CC-II sites also had abundant signals of other active histone marks, including H3K4me1, H3K4me3, with scarcity of H3K27me3 signals, suggesting their

enrichment in active promoters and enhancers (23). Conspicuously, CC-II sites were highly enriched for Runx1-binding (**Fig. 4A**). In accordance with this, a subset (~10%) of Stag2/STAG2 signals were colocalized with Runx1/RUNX1 signals in immunofluorescence of mouse HSPCs and human K562 leukemia cell lines using super-resolution microscopy (**Fig. 4C**). Moreover, Runx1/RUNX1 and Stag2/STAG2 were shown to be co-immunoprecipitated with Smc1/SMC1 and Smc3/SMC3 in mouse (32Dcl3) and human (K562) myeloid leukemia cell lines (**Supplementary Fig. S7C-D**). Additionally, according to the published ChIP-seq data from a murine HSPC cell line (HPC-7) (24), CC-II sites were highly enriched not only for Runx1 binding but also for binding of other TFs implicated in hematopoiesis as well as Asxl1 (25), RNA polymerase II (Pol II) and Med12 (26) (**Supplementary Fig. S7E-F**), which was also supported by an enrichment of consensus motifs of many hematopoietic TFs in CC-II sites compared with CC-I sites (**Supplementary Fig. S7G**). The distinct role of Stag2 at CC-II sites, as compared with at CC-I sites was further supported by ChIP-seq analysis in SKO-derived cells, in which only slight changes in Stag1 binding were observed at CC-II sites in contrast to remarkably increased binding of Stag1 at CC-I sites. This suggests that Stag1-cohesin does not replace Stag2-cohesin on CC-II sites, even in the face of Stag2 deficiency (**Fig. 4D**). Ctcf signals slightly decreased at CC-I sites but not at CC-II sites, consistent with specific binding of Ctcf at CC-I sites (**Fig. 4D**). These findings in ChIP-sequencing suggest a distinct role of Stag2 and Runx1 bindings at CC-II sites, in which active enhancers are enriched (**Fig. 4E**).

***Stag2*/*Runx1* codeficiency disrupts enhancer-promoter loops**

We next investigated the effects of Stag2 and/or Runx1 deletion on chromatin structures, using deep in situ Hi-C analysis of c-Kit$^+$ HSPCs from mice with different genotypes (27), which yielded 1.79 billion valid interactions per genotype on average. Overall, *Stag2*/*Runx1* deletions did not substantially affect boundaries of the large genomic structures that are known as compartment A/B, which largely correspond to transcriptionally active/inactive genomic regions, respectively (**Supplementary Fig. S8A-C**). However, insulations at boundaries of all topologically associating domains (TADs) were slightly enhanced in SKO and DKO cells, compared with those in WT cells (**Supplementary Fig. S8D**). Cohesin binding sites, CC-I and CC-II, were highly enriched at boundaries and inside regions of TADs, especially those located in compartment A ('A-TADs'), respectively (**Fig. 5A and Supplementary Fig. S8E**) and as expected, most of the DEGs in SKO-, RKO-, or DKO-derived LSK cells, as compared with WT-derived cells, were mapped within A-TADs (**Fig. 5B**). Thus, we calculated average difference in Hi-C contacts between mutant and WT cells,

focusing on A-TADs (n=3,295) after their size was normalized (**Fig. 5C**). SKO-derived cells showed slightly reduced short-range contacts in the vicinity of the bottom line, while the contacts were slightly enhanced at the TAD corner. By contrast, chromatin contacts in the corresponding A-TADs exhibited a more profound and wide-spread reduction in DKO cells, even though RKO alone minimally influence intra-TAD chromatin contacts. When the analysis was stratified for TAD hierarchy, the contacts tended to be more attenuated in nested TADs than the parental TADs (**Fig. 5D**).

We also evaluated the effects of *Stag2/Runx1* KO on the number of chromatin loops. Consistent with relative spatial distribution of CC-I and CC-II sites (**Supplementary Fig. S8E**), CC-II-anchored loops were shorter than CC-I-anchored loops (**Fig. 5E**). The number of loops originating from CC-II sites was reduced in SKO-derived cells and further decreased in DKO-derived cells, whereas the effects on loops originating from CC-I sites remained minimum across the genotypes (**Fig. 5F and Supplementary Fig. S8F-H**). When these loops were characterized by the presence or absence of Ctcf (CC-I), promoter, and enhancer at loop anchors, we found that the loops between enhancer-promoter (E-P), promoter-promoter (P-P), and enhancer-enhancer (E-E) were more selectively disrupted in SKO and DKO mice than other types of loops associated with Ctcf (**Fig 5G-H**). Moreover, these findings in the mouse model were confirmed in human leukemia cells using a series of isogenic AML cell lines derived from HL-60, which were targeted for *STAG2* and *RUNX1* using a CRISPR-Cas9 system, in which synergistic disruption of CC-II loops were recapitulated in *STAG2*/*RUNX1*-double knockout cells (**Supplementary Fig. S9A-F**).

To further understand the combinatorial effects on chromatin looping, we evaluated how the CC-II-anchored loops identified in WT cells are altered in SKO and DKO cells (**Fig. 5I**). As shown in **Fig. 5J**, the CC-II sites anchoring loops identified in WT cells (group (1)) were divided into four groups (groups (2)-(5)) depending on whether the loop at each site was lost or preserved in SKO and DKO cells, which were further investigated for the binding patterns of cohesin components, Pol II, Mediator, and ten hematopoietic transcription factors (TFs) at each group. Interestingly, we found relative enrichment of Stag2 at groups (2) and (4), strong enrichment of Pol II and Mediator at group (4), and relative enrichment of certain TFs at group (4) (**Fig. 5K**). In contrast, Stag1 enrichment was observed at group (5), i.e., CC-II sites with DKO-resistant loops. In addition, group (4) is bound by multiple TFs more frequently than other groups (**Fig. 5L**). These results suggest that, in the absence of Stag2, Runx1 deficiency additionally disrupts E-P loops anchored at Stag2

binding sites enriched for Pol II, Mediator, and TFs, leading to profound disruption of short-range chromatin interactions in DKO (**Fig. 5M**).

Transcriptional pausing underlies transcriptional vulnerability to *Stag2*/*Runx1* codeficiency

To see the effects of SKO and/or RKO on gene expression, we next investigated gene expression in LSK cells from these mice in greater details. On the basis of unsupervised clustering, we identified five discrete groups of genes (groups I-V) differentially expressed across four genotypes (**Fig. 6A-B and Supplementary Fig. S10A**). These groups were associated with distinct gene ontology terms and tissue- or hematopoietic lineage-specific gene expression profiles (**Fig. 6C and Supplementary Fig. S10B-C**), and group II and IV genes were synergistically upregulated and downregulated in DKO mice, respectively. These indicate that despite globally seen across the entire genome, loop attenuation does not necessarily result in a uniform change in overall gene expression. This is in agreement with the report that alteration in gene expression remained moderate and were seen only in a subset of genes, even when all loop structures were disrupted by complete loss of cohesin (28), suggesting that in general, the effect of chromatin looping on gene expression is modest and may be influenced by other contexts.

In this regard, it has been reported that super-enhancer (SE)-associated genes are more prone to downregulated expression in cohesin-deficient cells (28). In our mouse models, SE-associated genes also showed a trend of being downregulated in SKO and DKO cells, compared with RKO and WT cells, on average (**Fig. 6D-E and Supplementary Fig. S10D**). However, the effect of knockout was highly variable depending on SE site, compared with the case with typical enhancer (TE), particularly in DKO. This was exemplified for four SE-associated genes, *Hoxa9* (group IV)*, Gata2* (group II), and *Fos*/*Fosb* (group II) (**Fig. 6D)**. *Hoxa9* and other Hoxa cluster genes, which have long been implicated in the regulation of normal hematopoiesis and leukemogenesis (29), were downregulated in SKO/DKO cells, where attenuated loops were observed (**Fig. 6F and Supplementary Fig. S10E**). Thus we further investigated the roles of Hoxa9, which was also down-regulated in shRNA mouse models targeting cohesin components, *Stag2* and *Smc1* (10) (**Supplementary Fig. S11A**). In serial replating assay, Hoxa9-overexpression did not prolong the replating for SKO/DKO cells, although the number of colonies increased substantially in Hoxa9-expressed cells. (**Supplementary Fig. S11B**). On the other hand, in in vitro single-cell differentiation assay, DKO-derived HSPCs showed a reduced frequency of erythroid-containing colonies compared to WT-derived HSPCs, which, however, was substantially rescued

by Hoxa9-overexpression (**Supplementary Fig. S11C-E**). This suggests that the enhanced self-renewal in DKO is not attributed to *Hoxa9* down-regulation but mediated by other mechanisms, while down-regulated *Hoxa9* might contribute to differentiation block in these mice.

In contrast to Hoxa9 downregulation, even being associated with attenuated E-P loops, *Gata2* and *Fos*/*Fosb*, as well as other AP-1 components, showed upregulated expression (**Supplementary Fig. S12A**). Of note, in ATAC-seq analysis of DKO-derived LSK cells, consensus binding motifs of AP-1, Gata2, Runx1, IRFs, and Hoxa9 were enriched in enhanced ATAC-peaks frequently associated with group-II,V genes (AP-1 and Gata2) and attenuated ATAC-peaks frequently associated with group-IV genes (Runx1, IRFs, and Hoxa9), respectively (**Fig. 6G-H and Supplementary Fig. S12B-C**). Moreover, AP-1 and Gata2 motifs were highly enriched in promoter regions in group-II genes (**Supplementary Fig. S12D**). Thus, modulation of promoter activities by AP-1 and Gata2 may correspond to gene upregulation in group II genes by overriding detrimental effects of global loop suppression.

To further investigate the effect of E-P loop attenuation on gene expression, we next evaluated the link with transcriptional pausing, which has been known to correlate with enhancer activity and be implicated in the regulation of differentiation potential of stem cells (30-32). Of particular interest, in this regard, group-IV genes showed a high basal pausing level, as assessed by pausing index calculated by total Pol II ChIP-seq (**Fig. 6I and Supplementary Fig. S13A**). We separately confirmed that high-pausing genes were consistently and significantly downregulated in SKO and more profoundly decreased in DKO (**Supplementary Fig. S13B**). Degrees of pausing did not influence the expression specificity across diverse hematopoietic lineages (**Supplementary Fig. S13C**). These findings suggest a higher vulnerability of genes with high basal pausing to attenuated chromatin interactions caused by *Stag2/Runx1* deficiency. In addition, in coordination with reduced numbers of E-P loops in SKO and DKO cells across all DEG groups (**Fig. 6J**), we observed a substantial decrease in ChIP-seq intensities of Ser5-phosphorylated (Ser5-P) Pol II at the promoter proximal regions in SKO and DKO in all DEG groups, suggesting the global impact of E-P loop attenuation on promoter-proximal Pol II dynamics (**Fig. 6K**).

Explaining partial similarities of transcriptomes in SKO and RKO (**Fig. 2N**), group-IV genes were downregulated in SKO/RKO in a synergistic manner (**Fig. 6A-B and Supplementary Fig. S10A**), and were most strongly enriched for genes specifically expressed in HSCs across diverse hematopoietic lineages (**Fig. 6C**), suggesting a role of downregulated group-IV genes in the hematological phenotypes of Stag2/Runx1 deficiency. We also performed RNA-seq analysis in

HL-60 cell lines with *STAG2*/*RUNX1* deficiency. Although there were substantial differences in altered pathways in mouse LSK cells and HL-60 cells, we observed considerable overlaps of downregulated pathways in two experimental systems (**Supplementary Fig. S14A-B**).

Downregulation of high-pausing genes in *STAG2*/cohesin-mutated human AML/MDS

Finally we evaluated to what extent above findings in mice could be extended in human MDS/AML samples carrying *STAG2* and/or other *SRSA* mutations, as well as other cohesin mutations, using transcriptome data from three published cohorts of MDS/AML (6,33,34). An integrated pathway analysis of altered gene expression revealed a number of pathways changing in the same directions among SKO mouse model, cohesin-mutated MDS/AML cohorts, and HL-60 cell line model, including interferon response, regulation of leukocyte, adaptive immune responses, inflammatory response, ribosomal translation, and regulation of DNA/expression (**Fig. 7A**). Recapitulating the case with *Stag2*/*Runx1* deficient mouse models, expression of *HOXA9* and other HOXA cluster genes showed a uniform trend of downregulation with an increasing number of *SRSA* mutations in human samples (**Fig. 7B**). SE-associated genes identified in human normal HSPCs (35) were marginally downregulated in cohesin/*STAG2*-mutated MDS samples, as compared with TE-associated genes; however, this trend was less clear in AML samples (**Supplementary Fig. S15A-B**). We also evaluated the effect of basal level of transcriptional pausing on gene expression in *SRSA*-mutated samples, where the basal pausing level was calculated using total Pol II ChIP-seq of human normal HSPCs (36). High-pausing genes identified in mouse and human HSPCs were associated with several molecular pathways including interferon response and DNA repair response (**Fig. 7C**), consistent with downregulation of interferon and inflammatory responses in pathway network analysis (**Fig. 7A**). Conspicuously, high-pausing genes are consistently downregulated in cohesin- or *STAG2*-mutated samples in all three cohorts studied (**Fig. 7D and Supplementary Fig. S15C-D**). Moreover, high-pausing genes were preferentially downregulated in samples with ≥2 *SRSA* mutations, and *STAG2*-mutated cases with other *SRSA* mutations (**Fig. 7E-F and Supplementary Fig. S15E**). Taken together, these results support the relevance of transcriptional pausing and downregulation of high basal pausing genes in leukemogenesis not only of *Stag2*/*Runx1* DKO mice but also of human MDS/AML carrying multiple *SRSA* mutations.

Discussion

We have revealed a unique interplay between Stag2 and Runx1 in the maintenance of short-range chromatin interactions and transcriptional regulation, disruption of which leads to the development of MDS in mice. The interplay seems to depend on their localization to Ctcf-deficient, enhancer-proficient sites, in which the role of Stag2 cannot be replaced by Stag1. The distinct role of STAG2 in enhancer-rich regions is also suggested from the analysis of cultured cell lines in a recent report (37). Given the minimum changes with RKO alone, it is rather unexpected that Stag2/Runx1 DKO causes more profound chromatin alterations across the entire genome, compared with SKO alone. In the absence of Stag2, Runx1 loss additionally disrupts E-P loops anchored at cohesin bindings sites highly enriched for Pol II and Mediator. This suggests that such E-P loops vulnerable to combined loss of Stag2 and Runx1 may be associated with formation of transcriptional condensates through phase separation capacities of Pol II, Mediator, and TFs, as emerged from several recent studies (38-40).

The effects of cohesin loss on whole transcriptomes are modest despite of the essential roles in regulation of looping (28). Of interest, genes showing high basal transcriptional pausing are more prone to downregulated expression, compared with genes with low transcriptional pausing. Such genes may require the assistance of intact E-P loop formation and relevant enhancer-bound TFs, such as Runx1, for their transcription/expression, as group-IV genes are more profoundly downregulated in DKO cells. The link between gene expression and transcriptional pausing is in contrast to a previous study (28) which highlighted the effect of cohesin-mediated looping on the expression of super-enhancer-associated genes as typically seen for Hoxa genes in DKO mice. Given that super-enhancer-associated genes show lower degree of pausing than typical enhancer-associated genes (**Supplementary Fig. S13A**) (32), transcriptional pausing should be considered as a novel gate keeper to determine selective expression changes, distinct from association with super-enhancers. High-pausing genes in HSPCs are associated with several molecular pathways including interferon response and DNA repair response. Thus, downregulation of high-pausing genes is consistent with downregulation of interferon and inflammatory responses at whole transcriptome levels and enrichment of IRFs in reduced ATAC peaks in SKO and DKO. These findings suggest that transcriptional pausing provides the molecular basis of a previously reported downregulation of interferon and inflammatory responses, which control self-renewal and differentiation of HSPCs, in cohesin-mutated AML and hematopoietic cells (41). Taken together, perturbation of both several

super-enhancer-associated genes including *Hoxa9* and highly paused genes may contribute to multiple differentiation abnormalities and cell transformation in MDS/AML.

Distinct roles of Stag1 and Stag2 in HSPC self-renewal and differentiation in mouse models has been reported in a recent study (42). While Stag2-deficient mice display similar phenotypes in two studies, our study illustrates several novel findings: (1) association of mutations in *SRSA* genes; (2) mechanistic insights of combined effects of Stag2 and Runx1 loss on chromatin looping; and (3) the link between transcriptional pausing and selective gene dysregulation. Explaining the top significant associations between driver mutations, *SRSA* genes showed a conspicuous co-mutation pattern among MDS and related disorders, and also significantly co-mutated in a subset of primary AML, reported as AML with chromatin spliceosome mutation (43) or secondary-type primary AML (15)**,** suggesting that these mutations define a unique subset of myeloid neoplasms, where the deregulated interplay of these genes in the maintenance of enhancer activity might explain the common pathogenesis. The significant downregulation of high-pausing genes in samples with cohesin/*STAG2* and other *SRSA* mutations in three independent cohort of MDS/AML strongly supports this idea. A previous study reporting the interaction between Asxl1 and cohesin (25) and our finding of highly enriched Asxl1 binding at CC-II sites in mice (**Supplementary Fig. S7F**) are also suggestive of this, as well as a recent report demonstrating the enhanced transcriptional pausing induced by mutated *SRSF2* (44). We did not observe no significant increase in abnormal splicing in *Stag2*/*Runx1* DKO cells, suggesting that myelodysplasia in DKO mice is not likely due to altered splicing (**Supplementary Fig. S15F**). It is warranted in the future studies to better clarify the molecular basis of this unique subset of myeloid neoplasms.

Acknowledgments

We thank Satoko Yabuta, Ai Takatsu, Akiko Ozaki, Atsuko Ryu, Maki Nakamura, Takeshi Shirahari (Department of Pathology and Tumor Biology, Kyoto University), and Satoko Baba (Pathology Project for Molecular Targets, Cancer Institute, Japanese Foundation for Cancer Research) for technical assistance; Dr. Kazuko Miyazaki and Dr. Masaki Miyazaki (Department of Immunology, Institute for Frontier Life and Medical Sciences, Kyoto University) for technical advices on ATAC-seq and ChIP-seq experiments; Dr. Shuhei Asada and Dr. Toshio Kitamura (Division of Cellular Therapy, The Institute of Medical Science, University of Tokyo) for providing vectors; the Center for Anatomical, Pathological and Forensic Medical Research, Kyoto University Graduate School of Medicine, for preparing microscope slide; iLAC, Co., Ltd. for sequencing support. Super-resolution imaging was performed at the iCeMS Analysis Center, Institute for Integrated Cell-Material Sciences (iCeMS), Kyoto University Institute for Advanced Study (KUIAS), and we thank Dr. Takahiro Fujiwara for data analysis and Fumiyoshi Ishidate for technical assistance (iCeMS Analysis Center). The super-computing resource was provided by Human Genome Center, the Institute of Medical Science, the University of Tokyo. The results shown here are in part based upon data generated by the TCGA Research Network: https://www.cancer.gov/tcga.

This work was supported by Grant-in-Aid for Scientific Research (MEXT/JSPS KAKENHI JP26221308: S.O., JP26253060: S.O., JP17J05245: Y.O., JP18K16084: A.K., JP19H03560: A.Yoda), MEXT as "Priority Issue on Post-K computer" (Integrated Computational Life Science to Support Personalized and Preventive Medicine) (hp180198, hp190179: S.O., S.M.), Grants-in-Aid from the Japan Agency for Medical Research and Development, AMED (JP15cm0106056, JP19cm0106501, JP16ck0106073, JP19ck0106250: S.O., JP19cm0106138: A.K.), Scientific Research on Innovative Areas (15H05909, 15H05912: S.O, S.M., JP15H05979: K.Y., A.K., 15H05976: K.S., 19H04806: A.Yoda), “Stem Cell Aging and Disease” (14430052: M.S.), JST CREST (JPMJCR18S5: K.S.), grants from Takeda Science Foundation (S.O., H.M., T.Y., A.K.), Naito Foundation (A.Yoda), TERUMO LIFE SCIENCE FOUNDATION (A.Yoda), Yasuda Medical Foundation (A.Yoda), and JSPS Core-to-Core Program (S.O.). Studies conducted at Massachusetts Institute of Technology were supported by the United States Public Health Service Grant R01-GM034277 and R01-CA133404 to Phillip A. Sharp and P01-CA042063 to Tyler Jacks from the NIH, by the Koch Institute Support (core) grant P30-CA14051 from the National Cancer Institute, and supported in part by an agreement between the Whitehead Institute for Biomedical Research and Novo Nordisk. Studies conducted at the University of Pavia and Fondazione IRCCS Policlinico San Matteo, Pavia, Italy, were supported by

Associazione Italiana per la Ricerca sul Cancro (AIRC), Milan, Italy (InvestigatorGrant #20125: L.M.; AIRC 5x1000 project #21267: M.C.).

Author's contributions

Conception and design: Y. Ochi, A. Kon, K. Kataoka, H.I. Suzuki, S. Ogawa

Development of methodology: Y. Ochi, A. Kon, N. Nakazawa, A. Yoda, Y. Kogure

Acquisition of data: Y. Ochi, A. Kon, N. Nakazawa, H. Koseki, M. Nakayama, D. Morishita, A. Yoda, R. Okuda, K. Yoshida, S. Kotani, H. Makishima, L. Malcovati, K. Takeuchi, E. Sugihara, T-A. Sato, M. Cazzola

Analysis and interpretation of data: Y. Ochi, A. Kon, T. Sakata, M.M. Nakagawa, N. Nakazawa, M. Kakuta, T. Tsuruyama, R. Saiki, T. Yoshizato, Y. Shiozawa, Y. Nannya, L. Malcovati, M. Sanada, S. Miyano, H.I. Suzuki, S. Ogawa

Writing, review, and/or revision of the manuscript: Y. Ochi, A. Kon, T. Sakata, T. Yoshizato, H. Makishima, L. Malcovati, A. Takaori-Kondo, M. Cazzola, H.I. Suzuki, S. Ogawa

Administrative, technical, or material support: A. Kon, T. Sakata, H. Koseki, N. Kakiuchi, T. Nishimura, A. Yokoyama, M. Kengaku, K. Shirahige, S. Ogawa

Study supervision: A. Kon, A. Takaori-Kondo, H.I. Suzuki, S. Ogawa

Methods

Correlations between driver mutations in human MDS/AML

We analyzed in-house or publicly available data on large-scale genetic profiling of MDS/AML (2,3,14-18) for the investigation of correlations among major driver mutations commonly mutated in myeloid neoplasms. A total of 3,047 cases with MDS/AML were analyzed for correlations across 42 frequently mutated genes by Fisher's exact test as previously described (45). Patient survival was analyzed in 831 patients, for which data on survival was available (2). We analyzed number of driver mutations, variant allele frequencies of mutations, type of *RUNX1* mutations, and status of *STAG2* mutations in 76 cases which harbored more than one *STAG2* mutations, in a MDS cohort (2). The tumor cell fraction was calculated as previously described (46) with minor modifications. The tumor content was regarded as the maximum adjusted VAF among driver mutations in each case. Patient cohort is summarized in **Supplementary Table S1**. Clinical characteristics of MDS patients (2) with *STAG2*, *RUNX1*, *SRSF2*, and/or *ASXL1* mutations is summarized in **Supplementary Table S2**. Correlations between mutations in patients with MDS/AML are described in **Supplementary Table S3**.

Mice

Animal care was in accordance with institutional guidelines and approved by the Animal Research Committee, Graduate School of Medicine, Kyoto University (Kyoto, Japan). To generate the *Stag2* conditional knockout mouse model, the *Stag2*-targeting vector was constructed based on the *Cre-LoxP* system, in which two *LoxP* sites were inserted flanking exon 7, which encodes a STAG domain, and *Frt*-flanked neomycin selection cassette in a downstream intron. The linearized targeting vector was electroporated into murine C57BL/6 embryonic stem cells (RENKA strain) and were selected in G418. Homologous recombination was confirmed by direct sequencing of both outer regions of the neomycin cassette, and also by Southern blotting using neomycin-specific probes. Chimeric mice were produced by microinjection of targeted embryonic stem cells into blastocysts and were bred to C57BL/6 mice to establish germ line transmission (Trans Genic Inc., Kobe, Japan). The generated mice were initially crossed to a germline *Flp*-deleter (The Jackson Laboratory), to eliminate the neomycin cassette, and subsequently to the interferon-inducible *Mx1-Cre* transgenic mice (47). *Mx1-Cre* expression was induced by intraperitoneally injecting 500 μg of pIpC on six alternate days. Genotyping of *Stag2* floxed alleles were performed as

previously described (48) using the following primers: 5'- GACCACTAAGCTCATAATCGC-3' and 5'-ATTTCTGGCTACTACGCTTGC-3'. *Runx1* conditional knockout mice were described previously (49). CD57BL/6 CD45.1$^+$ mice and CD57BL/6 F1-CD45.1$^+$/CD45.2$^+$ mice were purchased from Sankyo-Lab Service (Tsukuba, Japan).

Retroviral transduction

For Hoxa9 overexpression, we used FLAG-tagged Hoxa9 (50) in the pMSCV-neo retroviral vector in serial replating assay and pGCDNsam-IRES-EGFP retroviral vector in single-cell differentiation assay. Retroviruses were produced by transient transfection of Plat-E packaging cells with retroviral constructs. Purified c-Kit$^+$ HSPCs were cultured in Iscove's modified Dulbecco's media (IMDM) containing 20% FBS and 50 ng/ml mouse SCF, mouse TPO, and human FLT-3L for 24 h, and then were rerto-transduced using Retronectin (Takara).

Serial replating assay

Freshly isolated 20,000 BM or 2,000 c-Kit$^+$ cells were seeded into cytokine-supplemented methylcellulose medium (Methocult, M3434; STEMCELL Technologies) according to the manufacturer's protocol. For Hoxa9-overexpression assay, c-Kit$^+$ cells transduced by pMSCV-neo vector were selected by adding G418 to the medium at the final concentration of 1 mg/ml. Colonies propagated in culture were scored at day 14 in duplicate. For replating, cells were resuspended in PBS, counted, and 10,000 cells were replated in duplicate once a week.

Flow cytometry

Single-cell suspensions were stained with monoclonal antibodies as previously described (48). Stained cells were analyzed with FACS Aria III or LSRFortessa X-10 flow cytometers (BD Bioscience, Franklin Lakes, NJ, USA). Cell sorting was performed with FACS Aria III. Cell cycle and apoptosis analysis were performed as previously described (48). Data were analyzed by FlowJo software (Tree Star, Ashland, CA, USA). The antibodies used in FACS experiments are described in **Supplementary Table S4**.

Isolation of mouse hematopoietic progenitors

Purification of HSPCs was performed as previously described (48). Briefly, freshly isolated BM cells were stained with APC-conjugated anti-c-Kit antibody and were enriched using anti-APC

magnetic beads and MACS LS columns (Miltenyi Biotec) according to the manufacturer's instruction.

Bone marrow transplantation

In non-competitive BMT assay, unfractionated BM cells (2 x 10^6 cells) from CD45.2 donor mice were transplanted into 8-12 weeks-old female CD45.1 recipient mice which were lethally irradiated at 9.5 Gy dose. In competitive BMT assay, unfractionated BM cells (1 x 10^6 cells) from CD45.2 donor mice were transplanted into 8-12 weeks-old female CD45.1 recipient mice which were lethally irradiated at 9.5 Gy dose, together with the equal number of BM cells from CD45.1/CD45.2 competitor mice. In the BMT experiments, pIpC was injected at 4 weeks after BMT. The donor chimerism in PB was evaluated at 4, 8, 12, 16, and 20 weeks after transplantation by flow cytometry. Mice were sacrificed at 20 weeks after transplantation, and the chimerism in each BM fraction was assessed by flow cytometry.

Generation of CRISPR knockout cell lines

Human AML HL-60 cell lines were obtained from American Type Culture Collection and not tested for Mycoplasma contamination. sgRNAs targeting *STAG2*/*RUNX1* were designed, and knockout efficiency was confirmed by Guide-it Mutation Detection Kit (Takara). To express SpCas9, HL-60 cell line was transduced by lentiCas9-Blast vector (Addgene #52962) and selected by blasticidin at the concentration of 5 μg/ml. To generate WT, SKO, RKO, and DKO cells, cells were transduced by pLKO5-sgRNA-EFS-GFP vector (Addgene #57822) containing sgRNA targeting STAG2 or non-targeting control sgRNA and pLKO5-sgRNA-EFS-tRFP vector (Addgene #57823) containing sgRNA targeting RUNX1 or non-targeting control sgRNA, and GFP^+/RFP^+ cells were sorted at single cell per well into a 96-well plate. Generated colonies were genotyped by amplicon sequencing using iSeq 100 (Illumina). All clones for SKO, RKO, and DKO were subjected to Western blotting to confirm the knockout of STAG2 and/or RUNX1. PCR primers and sgRNA sequences are provided in **Supplementary Table 5**, and genotypes of generated clones are described in **Supplementary Table 6**.

RNA-sequencing

RNA was extracted using RNeasy Mini Kit (QIAGEN) or NucleoSpin RNA XS (Macherey-Nagel). Libraries for RNA-seq were prepared using the NEBNext Ultra RNA Library Prep kit for Illumina

(New England BioLabs) and were subjected to sequencing using HiSeq 2500 or NovaSeq 6000 instrument (Illumina) with a standard 100-150-bp paired-end protocol as previously described (51). RNA-seq experiments were performed in two or more biological replicates. The sequencing reads were aligned to the reference genome (hg19 or mm9) using STAR (v2.5.3) (52). Reads on each refSeq gene were counted with featureCounts (v1.5.3) (53) from Subread package, and edgeR package in R (54) was used to identify the differentially expressed genes with FDR threshold of 0.05 and to generate the multidimensional scaling (MDS) plot. The analysis was performed in genes expressed at >1 count per million (CPM) in two or more samples, and generalized linear models were used to compare gene expression data. MSigDB overlap analysis was performed using MSigDB database and hallmark gene sets (https://www.gsea-msigdb.org/gsea/msigdb/index.jsp). RNA expression analysis in the hematopoietic system was carried out using Haemopedia RNA-seq datasets (55), and averages of log2 (TPM + 1) values of each gene set were calculated for each cell type. GSEA (v2.2.4) (56) was used to determine the sets of genes that are significantly different between groups. Enriched pathways were visualized using Enrichment Map (57) with the q-value < 0.05 and overlap similarity coefficient parameters > 0.5. RNA-seq datasets used are described in **Supplementary Table S7**. Differentially expressed genes shown in **Fig. 2I** are described in **Supplementary Tables S8-9**. Differentially expressed genes shown in **Fig. 3J** are described in **Supplementary Tables S10-15**.

More detailed methods are described in the Supplementary Methods.

ATAC-sequencing

ATAC-seq experiments were performed using LSK or CMP cells obtained from WT-, SKO-, RKO-, or DKO-transplanted mice using Fast-ATAC protocol as previously described (58) with minor modifications. Briefly, freshly isolated 10,000 cells were pelleted and fifty microliters of transposase mixture (25 ul of 2 x TD buffer, 2.5 ul of TDE1, 0.5 ul of 1% digitonin, and 22 ul of nuclease-free water) (FC-121-1030, Illumina; G9441) was added to the cells. After transposition reactions at 37°C for 30 min, transposed DNA was purified using QIAGEN MinElute Reaction Cleanup kit. Transposed fragments were PCR-amplified, and the resulting library was sequenced on Hiseq 2500. ATAC-seq experiments were performed in biological duplicates. Reads were aligned to the mouse mm9 reference genome using bowtie2 (v2.3.3) (59) with -X 2000 –no-mixed –very-sensitive parameters following adapter trimming using cutadapt (v1.14) (60). Duplicates

were removed by Picard (v2.6.0) (https://broadinstitute.github.io/picard/), and reads on mitochondria genome or blacklisted regions (ENCODE) were removed by bedtools (v2.27.1) (61). Peaks were called with MACS (v2.1.1) (62) with –nomodel –broad parameters with a q-value threshold of 1 x 10^{-5} for individual replicate as well as merged data of all replicates. Read counts on peaks for merged data were counted with the multicov function in bedtools, and edgeR was used to identify the peaks with differential accessibility with FDR threshold of 0.05. Transcription factor motifs were discovered with HOMER (63) in differentially accessible sites (up or down, compared with WT) using stable peaks or random genome as backgrounds. Peak annotation was performed with HOMER. Differentially accessible ATAC regions in SKO-derived LSK and CMP cells (vs WT) shown in **Fig. 2** are described in **Supplementary Tables S16-19**.

ChIP-sequencing

ChIP-seq experiments were performed using c-Kit$^+$ HSPCs or HL-60 cell lines. Cells were fixed in PBS with 1% formaldehyde (Thermo Fisher Scientific) for 10 min at room temperature with gentle mixing. The reaction was stopped by adding glycine solution (10x) (Cell Signaling Technology) and incubating for 5 minutes at room temperature, and the cells were washed in cold PBS twice. The cells were then processed with SimpleChIP Plus Sonication Chromatin IP Kit (Cell Signaling Technology) and Covaris E220 (Covaris) according to the manufacturer's protocol. After purification of ChIPed DNA, ChIP-seq libraries were constructed using ThruPLEX DNA-seq kit (Takara) according to the manufacturer's protocol, and then subjected to sequencing using HiSeq 2500 or NoveSeq 6000 (Illumina). ChIP-seq experiments were performed in two or more biological replicates with input controls. The sequencing reads were aligned to the reference genome (hg19 or mm9) using bowtie (v1.2.2) (64) following trimming of adapters and read tails to a total length of 50 base pairs using cutadapt. Duplicates and reads on blacklisted regions (ENCODE) were removed by Picard and bedtools, respectively. Peaks were called using MACS (v2.1.1) for each replicate individually with a *P*-value threshold of 1 x 10^{-3} unless otherwise specified, and overlapped peaks among replicates were regarded as consensus peak sets. Motif analysis and peak annotation were performed with HOMER. Super-enhancers were identified with H3K27ac ChIP-seq data in WT HSPCs using ROSE (65) with default parameters. Identified super-enhancers are described in **Supplementary Table S20**. Super-enhancers in human HSCs were previously described (35), and we used the dataset of BI_CD34_Primary_RO01536 for assignment of super-enhancer-associated genes. Calculation of ChIP signal intensities around

peaks and generation of read density profile plots and heatmaps were performed using deeptools (66). For clustering of cohesin binding sites, we calculated logarithm of H3K27ac and Ctcf ChIP signal intensities summed up around ± 200 bp from centers of cohesin binding sites (Stag1 and/or Stag2 peaks) by deeptools, performed clustering using flowPeaks (67), and regarded the H3K27ac high clusters as cohesin cluster II and the others as cluster I. Binding profiles of cohesin components, Pol II, Mediator, and ten hematopoietic TFs were similarly calculated around ± 200 bp from centers of cohesin binding sites (**Fig. 5K**). We also used ChIP-seq datasets (10 TFs: Asxl1, Fli1, Gata2, Gfi1b, Lmo2, Lyl1, Meis1, Pu1, Runx1, Scl; Pol II, Med12 in mouse, Pol II in human (24-26,36)) in previous studies. More detailed methods are described in the Supplementary Methods.

Pol II pausing analysis

For total Pol II ChIP-seq, two replicates were merged and ChIP-seq peaks were called using MACS (v1.4.2) with a *P*-value threshold of 1×10^{-3}. For analysis of pausing indices in mice, expressed genes, whose transcription start sites (TSSs) overlapped with Pol II ChIP-seq peaks in WT HSPCs, were subjected to downstream analyses. Pausing indices were calculated as the input-subtracted read density in the promoter-proximal region (-50 bp to +300 bp around TSS) divided by that of the gene body (from +300 bp to 2 kb downstream of the end of gene). Genes with positive signals in both the promoter-proximal region and gene body were further considered. ChIP-seq intensities of Ser5-P Pol II in the promoter proximal region were similarly calculated. Pol II ChIP-seq in human CD133-positive cells was previously described (36), and ChIP-seq peaks were called using MACS (v1.4.2) with a *P*-value threshold of 1×10^{-5}. For pausing analysis in human, input subtraction was not performed and genes, whose TSSs overlapped with Pol II ChIP-seq peaks, were considered. Statistical significance was assessed with one-sided Wilcoxon rank-sum test.

Hi-C

Hi-C experiments were performed using MboI restriction enzyme as previously described (27). Briefly, two million cells were crosslinked with 1% formaldehyde for 10 min at room temperature. Cells were permeabilized and chromatin was digested with MboI restriction enzyme, and the ends of restriction fragments were labeled with biotinylated nucleotides and ligated. After crosslink reversal, DNA was purified and sheared with Covaris M220 (Covaris). Then point ligation

junctions were pulled down with streptavidin beads. Then libraries were constructed with Nextera Mate Pair Sample Preparation Kit (Illumina) according to the manufacturer's protocol, and subject to sequencing using NovaSeq 6000 (Illumina) with a standard 100- or 150-bp paired-end protocol. Hi-C experiments were performed in biological duplicates. The sequencing reads were processed using Juicer (27) and hg19 or mm10 reference genome. After filtering of reads, the average valid interactions per genotype resulted in 1.79 billion for mouse HSPCs and 1.66 billion for HL-60 cells. For comparative analysis, the valid interactions after filtering were randomly resampled and arranged in the number of the lowest sample. Contact matrices used for further analysis were created for each replicate as well as merged one by genotype and Knight-Ruiz (KR)-normalized with Juicer. Loops were called at 5kb and 10kb resolutions using HICCUPS (27) and then merged to construct loop sets. Loops were classified into CC-I loops (whose anchors overlapped with at least one CC-I sites but not with CC-II) and CC-II loops (whose anchors overlapped with at least one CC-II but not CC-I sites). Topologically associating domains (TADs) were called at 5kb resolution using Arrowhead (27). TAD boundaries were defined as +-5kb from the 5'- or 3'- ends of TADs, and insides were regions insides of both boundaries. More detailed methods are described in the Supplementary Methods.

Statistical analysis

In human MDS/AML, correlations across 42 frequently mutated genes were assessed by Fisher's exact test. For mouse phenotype analysis, we calculated *P*-values with two-tailed unpaired Student's *t* test for two group comparison, or ordinary one-way analysis of variance (ANOVA) with Bonferroni analysis for three or more group comparison using GraphPad Prism (v6). For survival analysis, survival was estimated using the Kaplan-Meier method, and groups were compared using the log-rank test, with survival package in R software. In RNA-seq, ATAC-seq, and ChIP-seq analyses, statistical analyses were performed using edgeR, HOMER, DAVID, TSEA, GSEA, or MACS. For metaplot analysis, bin-wise *P*-values were obtained using one-sided Wilcoxon rank-sum test. For splicing analysis, differential PSI was assessed using two-sided moderated t-test and Benjamini-Hochberg correction. For pausing analysis and RNA expression analysis according to pausing indices, statistical significance was assessed with one-sided Wilcoxon rank-sum test.

Data availability

External ChIP-seq datasets used in this study are summarized in **Supplementary Table S21**. The sequencing data generated in this study are available in the GEO repository, under accession number GSE131583. All other data will be made available upon request to the corresponding author.

Additional Methods

Detailed methods for quantitative reverse transcription PCR (qRT-PCR), Western blotting, co-immunoprecipitation, histology and cytology, immunostaining, microscopy and data analysis, Single-cell differentiation assay, and splicing analysis are described in the Supplementary Methods.

References

1. Cazzola M, Della Porta MG, Malcovati L. The genetic basis of myelodysplasia and its clinical relevance. Blood **2013**;122:4021-34.
2. Haferlach T, Nagata Y, Grossmann V, Okuno Y, Bacher U, Nagae G*, et al.* Landscape of genetic lesions in 944 patients with myelodysplastic syndromes. Leukemia **2014**;28:241-7.
3. Papaemmanuil E, Gerstung M, Malcovati L, Tauro S, Gundem G, Van Loo P*, et al.* Clinical and biological implications of driver mutations in myelodysplastic syndromes. Blood **2013**;122:3616-27; quiz 99.
4. Ogawa S. Genetics of MDS. Blood **2019**;133:1049-59.
5. Kon A, Shih LY, Minamino M, Sanada M, Shiraishi Y, Nagata Y*, et al.* Recurrent mutations in multiple components of the cohesin complex in myeloid neoplasms. Nat Genet **2013**;45:1232-7.
6. Ley TJ, Miller C, Ding L, Raphael BJ, Mungall AJ, Robertson A*, et al.* Genomic and epigenomic landscapes of adult de novo acute myeloid leukemia. N Engl J Med **2013**;368:2059-74.
7. Yoshida K, Toki T, Okuno Y, Kanezaki R, Shiraishi Y, Sato-Otsubo A*, et al.* The landscape of somatic mutations in Down syndrome-related myeloid disorders. Nat Genet **2013**;45:1293-9.
8. Remeseiro S, Losada A. Cohesin, a chromatin engagement ring. Curr Opin Cell Biol **2013**;25:63-71.
9. Viny AD, Ott CJ, Spitzer B, Rivas M, Meydan C, Papalexi E*, et al.* Dose-dependent role of the cohesin complex in normal and malignant hematopoiesis. J Exp Med **2015**;212:1819-32.
10. Mullenders J, Aranda-Orgilles B, Lhoumaud P, Keller M, Pae J, Wang K*, et al.* Cohesin loss alters adult hematopoietic stem cell homeostasis, leading to myeloproliferative neoplasms. J Exp Med **2015**;212:1833-50.
11. Mazumdar C, Shen Y, Xavy S, Zhao F, Reinisch A, Li R*, et al.* Leukemia-Associated Cohesin Mutants Dominantly Enforce Stem Cell Programs and Impair Human Hematopoietic Progenitor Differentiation. Cell Stem Cell **2015**;17:675-88.
12. Galeev R, Baudet A, Kumar P, Rundberg Nilsson A, Nilsson B, Soneji S*, et al.* Genome-wide RNAi Screen Identifies Cohesin Genes as Modifiers of Renewal and Differentiation in Human HSCs. Cell Rep **2016**;14:2988-3000.
13. Rowley MJ, Corces VG. Organizational principles of 3D genome architecture. Nat Rev Genet **2018**;19:789-800.
14. Walter MJ, Shen D, Ding L, Shao J, Koboldt DC, Chen K*, et al.* Clonal architecture of secondary acute myeloid leukemia. N Engl J Med **2012**;366:1090-8.

15. Lindsley RC, Mar BG, Mazzola E, Grauman PV, Shareef S, Allen SL*, et al.* Acute myeloid leukemia ontogeny is defined by distinct somatic mutations. Blood **2015**;125:1367-76.
16. Makishima H, Yoshizato T, Yoshida K, Sekeres MA, Radivoyevitch T, Suzuki H*, et al.* Dynamics of clonal evolution in myelodysplastic syndromes. Nat Genet **2017**;49:204-12.
17. Yoshizato T, Nannya Y, Atsuta Y, Shiozawa Y, Iijima-Yamashita Y, Yoshida K*, et al.* Genetic abnormalities in myelodysplasia and secondary acute myeloid leukemia: impact on outcome of stem cell transplantation. Blood **2017**;129:2347-58.
18. Meggendorfer M, de Albuquerque A, Nadarajah N, Alpermann T, Kern W, Steuer K*, et al.* Karyotype evolution and acquisition of FLT3 or RAS pathway alterations drive progression of myelodysplastic syndrome to acute myeloid leukemia. Haematologica **2015**;100:e487-90.
19. Hu L, Li M, Ding Y, Pu L, Liu J, Xie J*, et al.* Prognostic value of RDW in cancers: a systematic review and meta-analysis. Oncotarget **2017**;8:16027-35.
20. Pietras EM, Reynaud D, Kang YA, Carlin D, Calero-Nieto FJ, Leavitt AD*, et al.* Functionally Distinct Subsets of Lineage-Biased Multipotent Progenitors Control Blood Production in Normal and Regenerative Conditions. Cell Stem Cell **2015**;17:35-46.
21. de Bruijn M, Dzierzak E. Runx transcription factors in the development and function of the definitive hematopoietic system. Blood **2017**;129:2061-9.
22. Buenrostro JD, Giresi PG, Zaba LC, Chang HY, Greenleaf WJ. Transposition of native chromatin for fast and sensitive epigenomic profiling of open chromatin, DNA-binding proteins and nucleosome position. Nat Methods **2013**;10:1213-8.
23. Shlyueva D, Stampfel G, Stark A. Transcriptional enhancers: from properties to genome-wide predictions. Nat Rev Genet **2014**;15:272-86.
24. Wilson NK, Foster SD, Wang X, Knezevic K, Schutte J, Kaimakis P*, et al.* Combinatorial transcriptional control in blood stem/progenitor cells: genome-wide analysis of ten major transcriptional regulators. Cell Stem Cell **2010**;7:532-44.
25. Li Z, Zhang P, Yan A, Guo Z, Ban Y, Li J*, et al.* ASXL1 interacts with the cohesin complex to maintain chromatid separation and gene expression for normal hematopoiesis. Sci Adv **2017**;3:e1601602.
26. Aranda-Orgilles B, Saldana-Meyer R, Wang E, Trompouki E, Fassl A, Lau S*, et al.* MED12 Regulates HSC-Specific Enhancers Independently of Mediator Kinase Activity to Control Hematopoiesis. Cell Stem Cell **2016**;19:784-99.
27. Rao SS, Huntley MH, Durand NC, Stamenova EK, Bochkov ID, Robinson JT*, et al.* A 3D map of the human genome at kilobase resolution reveals principles of chromatin looping. Cell **2014**;159:1665-80.
28. Rao SSP, Huang SC, Glenn St Hilaire B, Engreitz JM, Perez EM, Kieffer-Kwon KR*, et al.* Cohesin Loss Eliminates All Loop Domains. Cell **2017**;171:305-20 e24.

29. Collins CT, Hess JL. Deregulation of the HOXA9/MEIS1 axis in acute leukemia. Curr Opin Hematol **2016**;23:354-61.
30. Ghavi-Helm Y, Klein FA, Pakozdi T, Ciglar L, Noordermeer D, Huber W*, et al.* Enhancer loops appear stable during development and are associated with paused polymerase. Nature **2014**;512:96-100.
31. Williams LH, Fromm G, Gokey NG, Henriques T, Muse GW, Burkholder A*, et al.* Pausing of RNA polymerase II regulates mammalian developmental potential through control of signaling networks. Mol Cell **2015**;58:311-22.
32. Henriques T, Scruggs BS, Inouye MO, Muse GW, Williams LH, Burkholder AB*, et al.* Widespread transcriptional pausing and elongation control at enhancers. Genes Dev **2018**;32:26-41.
33. Tyner JW, Tognon CE, Bottomly D, Wilmot B, Kurtz SE, Savage SL*, et al.* Functional genomic landscape of acute myeloid leukaemia. Nature **2018**;562:526-31.
34. Shiozawa Y, Malcovati L, Galli A, Pellagatti A, Karimi M, Sato-Otsubo A*, et al.* Gene expression and risk of leukemic transformation in myelodysplasia. Blood **2017**;130:2642-53.
35. Hnisz D, Abraham BJ, Lee TI, Lau A, Saint-Andre V, Sigova AA*, et al.* Super-enhancers in the control of cell identity and disease. Cell **2013**;155:934-47.
36. Cui K, Zang C, Roh TY, Schones DE, Childs RW, Peng W*, et al.* Chromatin signatures in multipotent human hematopoietic stem cells indicate the fate of bivalent genes during differentiation. Cell Stem Cell **2009**;4:80-93.
37. Kojic A, Cuadrado A, De Koninck M, Gimenez-Llorente D, Rodriguez-Corsino M, Gomez-Lopez G*, et al.* Distinct roles of cohesin-SA1 and cohesin-SA2 in 3D chromosome organization. Nat Struct Mol Biol **2018**;25:496-504.
38. Cho WK, Spille JH, Hecht M, Lee C, Li C, Grube V*, et al.* Mediator and RNA polymerase II clusters associate in transcription-dependent condensates. Science **2018**;361:412-5.
39. Sabari BR, Dall'Agnese A, Boija A, Klein IA, Coffey EL, Shrinivas K*, et al.* Coactivator condensation at super-enhancers links phase separation and gene control. Science **2018**;361.
40. Boija A, Klein IA, Sabari BR, Dall'Agnese A, Coffey EL, Zamudio AV*, et al.* Transcription Factors Activate Genes through the Phase-Separation Capacity of Their Activation Domains. Cell **2018**;175:1842-55 e16.
41. Cuartero S, Weiss FD, Dharmalingam G, Guo Y, Ing-Simmons E, Masella S*, et al.* Control of inducible gene expression links cohesin to hematopoietic progenitor self-renewal and differentiation. Nat Immunol **2018**;19:932-41.

42. Viny AD, Bowman RL, Liu Y, Lavallee VP, Eisman SE, Xiao W*, et al.* Cohesin Members Stag1 and Stag2 Display Distinct Roles in Chromatin Accessibility and Topological Control of HSC Self-Renewal and Differentiation. Cell Stem Cell **2019**;25:682-96 e8.
43. Papaemmanuil E, Gerstung M, Bullinger L, Gaidzik VI, Paschka P, Roberts ND*, et al.* Genomic Classification and Prognosis in Acute Myeloid Leukemia. N Engl J Med **2016**;374:2209-21.
44. Chen L, Chen JY, Huang YJ, Gu Y, Qiu J, Qian H*, et al.* The Augmented R-Loop Is a Unifying Mechanism for Myelodysplastic Syndromes Induced by High-Risk Splicing Factor Mutations. Mol Cell **2018**;69:412-25 e6.
45. Suzuki H, Aoki K, Chiba K, Sato Y, Shiozawa Y, Shiraishi Y*, et al.* Mutational landscape and clonal architecture in grade II and III gliomas. Nat Genet **2015**;47:458-68.
46. Ochi Y, Hiramoto N, Yoshizato T, Ono Y, Takeda J, Shiozawa Y*, et al.* Clonally related diffuse large B-cell lymphoma and interdigitating dendritic cell sarcoma sharing MYC translocation. Haematologica **2018**;103:e553-e6.
47. Kuhn R, Schwenk F, Aguet M, Rajewsky K. Inducible gene targeting in mice. Science **1995**;269:1427-9.
48. Kon A, Yamazaki S, Nannya Y, Kataoka K, Ota Y, Nakagawa MM*, et al.* Physiological Srsf2 P95H expression causes impaired hematopoietic stem cell functions and aberrant RNA splicing in mice. Blood **2018**;131:621-35.
49. Ichikawa M, Asai T, Saito T, Seo S, Yamazaki I, Yamagata T*, et al.* AML-1 is required for megakaryocytic maturation and lymphocytic differentiation, but not for maintenance of hematopoietic stem cells in adult hematopoiesis. Nat Med **2004**;10:299-304.
50. Yokoyama A, Ficara F, Murphy MJ, Meisel C, Hatanaka C, Kitabayashi I*, et al.* MLL becomes functional through intra-molecular interaction not by proteolytic processing. PLoS One **2013**;8:e73649.
51. Yoshida K, Sanada M, Shiraishi Y, Nowak D, Nagata Y, Yamamoto R*, et al.* Frequent pathway mutations of splicing machinery in myelodysplasia. Nature **2011**;478:64-9.
52. Dobin A, Davis CA, Schlesinger F, Drenkow J, Zaleski C, Jha S*, et al.* STAR: ultrafast universal RNA-seq aligner. Bioinformatics **2013**;29:15-21.
53. Liao Y, Smyth GK, Shi W. featureCounts: an efficient general purpose program for assigning sequence reads to genomic features. Bioinformatics **2014**;30:923-30.
54. Robinson MD, McCarthy DJ, Smyth GK. edgeR: a Bioconductor package for differential expression analysis of digital gene expression data. Bioinformatics **2010**;26:139-40.
55. Choi J, Baldwin TM, Wong M, Bolden JE, Fairfax KA, Lucas EC*, et al.* Haemopedia RNA-seq: a database of gene expression during haematopoiesis in mice and humans. Nucleic Acids Res **2019**;47:D780-D5.

56. Subramanian A, Tamayo P, Mootha VK, Mukherjee S, Ebert BL, Gillette MA*, et al.* Gene set enrichment analysis: a knowledge-based approach for interpreting genome-wide expression profiles. Proc Natl Acad Sci U S A **2005**;102:15545-50.
57. Merico D, Isserlin R, Stueker O, Emili A, Bader GD. Enrichment map: a network-based method for gene-set enrichment visualization and interpretation. PLoS One **2010**;5:e13984.
58. Corces MR, Buenrostro JD, Wu B, Greenside PG, Chan SM, Koenig JL*, et al.* Lineage-specific and single-cell chromatin accessibility charts human hematopoiesis and leukemia evolution. Nat Genet **2016**;48:1193-203.
59. Langmead B, Salzberg SL. Fast gapped-read alignment with Bowtie 2. Nat Methods **2012**;9:357-9.
60. Martin M. Cutadapt removes adapter sequences from high-throughput sequencing reads. 2011 **2011**;17:3.
61. Quinlan AR, Hall IM. BEDTools: a flexible suite of utilities for comparing genomic features. Bioinformatics **2010**;26:841-2.
62. Zhang Y, Liu T, Meyer CA, Eeckhoute J, Johnson DS, Bernstein BE*, et al.* Model-based analysis of ChIP-Seq (MACS). Genome Biol **2008**;9:R137.
63. Heinz S, Benner C, Spann N, Bertolino E, Lin YC, Laslo P*, et al.* Simple combinations of lineage-determining transcription factors prime cis-regulatory elements required for macrophage and B cell identities. Mol Cell **2010**;38:576-89.
64. Langmead B. Aligning short sequencing reads with Bowtie. Curr Protoc Bioinformatics **2010**;Chapter 11:Unit 11 7.
65. Loven J, Hoke HA, Lin CY, Lau A, Orlando DA, Vakoc CR*, et al.* Selective inhibition of tumor oncogenes by disruption of super-enhancers. Cell **2013**;153:320-34.
66. Ramirez F, Dundar F, Diehl S, Gruning BA, Manke T. deepTools: a flexible platform for exploring deep-sequencing data. Nucleic Acids Res **2014**;42:W187-91.
67. Ge Y, Sealfon SC. flowPeaks: a fast unsupervised clustering for flow cytometry data via K-means and density peak finding. Bioinformatics **2012**;28:2052-8.

Figure legends

Figure 1. *STAG2* and associated mutations in human MDS/AML.

A, Correlations between driver mutations in MDS/AML. Left panel: Significantly co-occurring and mutually exclusive mutations are shown in red and blue circles, respectively. Odds ratio and associated q-values are indicated by the color gradient and size of circles, respectively. Right upper panel: Volcano plot showing the relationship of Pearson correlation values and corresponding -log10(*P*-value) between any pairs of the co-occurring mutations found in more than five cases. *P*-values were calculated by Fisher's exact test. **B**, Venn diagram showing the overlaps of '*SRSA*' mutations (*STAG2*, *RUNX1*, *SRSF2*, and *ASXL1*) in MDS/AML cases. The numbers of cases are indicated in red or blue colors, in which >20% increase or decrease are observed compared with the expected numbers by chance as shown in parenthesis, respectively. **C**, Kaplan–Meier estimates of overall survival according to the number of *SRSA* mutations. *P*-value was calculated by log-rank test. **D**, Adjusted VAF values of *SRSA* mutations. **E**, Tumor cell fractions (TCFs) of indicated driver mutations are shown for the patients harboring two or more different *STAG2* mutations.

Figure 2. Stag2 depletion alters HSC self-renewal and differentiation in mice.

A, White blood cell (WBC) count, hemoglobin (HGB) level, platelet (PLT) count and red cell distribution width (RDW) in the peripheral blood (PB) of wild-type (WT) and *Stag2* conditional knockout (SKO) littermate male mice are plotted as dots (n = 17), in which the mean ± standard deviation (SD) are indicated as bars (left panels). Number of granulocytes/monocytes ($CD11b^+$), B-lymphocytes ($B220^+$) and T-lymphocytes ($CD4^+$/$CD8^+$) in the PB of WT and SKO mice (mean ± SD, n = 10) are shown in the right panel. **B**, Frequency of lineage (Lin)-negative/$Sca1^+$/$c\text{-}Kit^+$ (LSK) cells (left panel), and frequencies of long-term HSC (LT-HSC), short-time HSC (ST-HSC), multipotent progenitor (MPP)-2, MPP-3, and MPP-4 fractions in the BM of WT or SKO mice (mean ± SD, n = 6) (right panel) are shown. **C**, Frequencies of common myeloid progenitors (CMPs), granulocyte-macrophage progenitors (GMPs), megakaryocyte/erythrocyte lineage-restricted progenitors (MEPs) and common lymphoid progenitors (CLPs) in the BM of WT and SKO mice (mean ± SD, n = 6). **D**, Frequencies of each lineage-committed cells in the BM of WT and SKO mice (mean ± SD, n = 4). **E**, Colony counts in methylcellulose replating experiments using nucleated BM cells from WT or SKO mice (mean ± SD, n = 2) are shown. BM cells were plated in duplicate at a density of 20,000 cells/plate for the first plating and 10,000 cells/plate for replating.

F, Frequency of apoptotic cells (Annexin$^+$/7-AAD$^-$) in CD150$^+$/CD48$^-$ LSK cells (n = 6, mean ± SD). **G**, Frequency of cycling cells (S/G2/M; Ki-67$^+$/Hoechst$^+$), quiescent cells (G0; Ki-67-/Hoechst-), and G1 cells (Ki-67$^+$/Hoechst$^-$) in CD150$^+$/CD48$^-$ LSK cells (n = 5, mean ± SD). **H**, Percentages of CD45.2$^+$ donor cells within each fraction of the BM or PB after competitive BM transplantation (16 weeks after pIpC injection) are shown (mean ± SD, n = 10 for WT and 6 for SKO). **I**, MA plot showing the transcriptional changes between WT- and SKO-derived LSK cells. Differentially expressed genes (DEGs) (FDR < 0.05) are indicated by red color. FC, fold-change. **J**, Gene set enrichment analysis (GSEA) between WT- and SKO-derived LSK cells, showing a significant enrichment of genes characteristic of GMPs and B-lymphocytes. Nominal *P*-value, false discovery rate (FDR), and normalized enrichment score (NES) are indicated. **K**, Expression levels of *Runx1* in LSK and CMP fractions are indicated by counts per million mapped reads (CPM) (min to max values with mean, n = 3). *P*-values were calculated using edgeR package in R software. **L,** Motifs and corresponding *P*-values identified by de novo motif search in ATAC-seq peaks that gained accessibility in SKO-derived LSK cells. **M**, Enrichment of known transcription factor (TF) motifs in ATAC-seq peaks that gained accessibility in SKO-derived LSK (left panel) and CMP cells (right panel). The sorted motif rank and –log10(*P*-value) of a motif enrichment test using stable peaks as backgrounds is indicated in horizontal and vertical axis, respectively. **N**, GSEA analysis between SKO- and WT-derived LSK cells, showing a negative enrichment of genes down-regulated in *Runx1* conditional knockout (RKO)-derived LSK cells compared with WT (left panel), and GSEA analysis between RKO- and WT-derived LSK cells, showing a negative enrichment of genes down-regulated in SKO-derived LSK cells compared with WT (right panel). For panels (**A-G**), mice were analyzed at 12-24 weeks of age. * $P < 0.05$; ** $P < 0.01$; *** $P < 0.001$; **** $P < 0.0001$. Two-tailed unpaired Student's t-test in (**A-H**).

Figure 3. *Stag2*/*Runx1* double knockouts induce MDS in mice.

A, WBC, HGB, mean corpuscular volume (MCV), and PLT count in the PB of recipient mice transplanted with BM cells of WT, SKO, RKO, or *Stag2*/*Runx1* double conditional knockout (DKO) mice are plotted as dots (n = 8 for WT, 9 for SKO, 14 for RKO and 10 for DKO), in which the mean ± SD are indicated as bars (left panels). Number of granulocytes/monocytes (CD11b$^+$), B-lymphocytes (B220$^+$), and T-lymphocytes (CD4$^+$/CD8$^+$) in the PB of WT-, SKO-, RKO-, and DKO-transplanted mice are shown in the right panel (mean ± SD, n = 9 for WT and SKO, 14 for RKO, and 4 for DKO). **B-G**, Frequencies of HSPCs (**B-C**), myeloid progenitors (**D**), megakaryocyte/erythroid

progenitors (**E**), erythroblasts (**F**), and lineage-committed cells (**G**) in the BM are shown (mean ± SD, n = 5 for WT and RKO, and 3 for SKO and DKO). PreMegE, pre-megakaryocyte-erythroid progenitors; MkP, megakaryocytic progenitors; PreCFUe, pre-colony-forming unit erythroid cells; CFUe, colony-forming unit erythroid cells. **H**, Kaplan–Meier estimates of overall survival for each genotype (n = 9 for WT and SKO, 16 for RKO, and 10 for DKO). *P*-value was calculated by log-rank test. Death due to MDS is indicated by the purple circle. **I**, Representative May-Grünwald-Giemsa staining of BM cells showing dysplastic features, including pseudo-Pelger–Huët anomalies in neutrophils, binucleated megakaryocytes or erythroblasts, and abnormal mitosis. **J**, MA plot showing the transcriptional changes in LSK cells derived from SKO, RKO, and DKO mice compared with WT-derived LSK cells. DEGs (FDR < 0.05) are indicated by red color. **K**, Frequency of differentially accessible ATAC peaks for SKO-, RKO- and DKO-derived LSK cells compared with WT. In panels (**A-G**), mice were analyzed 16-20 weeks after pIpC injection. * $P < 0.05$; ** $P < 0.01$; *** $P < 0.001$; **** $P < 0.0001$. *P*-values were calculated by ordinary one-way ANOVA with Bonferroni analysis in (**A-G**).

Figure 4. Colocalization of Stag2-cohesin and Runx1 at enhancers.

A, Upper panels: ChIP-seq density heatmap of cohesin components (Stag1, Stag2, and Smc1), Ctcf, Runx1, and histone marks (H3K4me1, H3K4me3, H3K27ac, and H3K27me3) in c-Kit$^+$ HSPCs of WT mice centered on Stag1- and/or Stag2-cohesin binding sites (n = 27,997) are depicted in descending order of Stag2 peak intensities, in which cohesin binding sites were divided into two clusters (cohesin cluster-I (CC-I) and cohesin cluster-II (CC-II)) according to the ChIP signals for Ctcf and H3K27ac (see also **Supplementary Fig. S7A-B**). Color scales below the heatmaps indicate ChIP-seq intensities (reads per kilobase per million mapped reads (RPKM)). Lower panels: Average ChIP-seq read intensity plot for CC-I (blue) and CC-II (green) distribution around the cohesin binding sites. **B**, Average ChIP-seq read intensities of Stag1 or Stag2 around CC-I or CC-II sites (upper panels) and *P*-values for comparison between Stag1 and Stag2 across each bin (lower panels). **C**, Super-resolution images of Stag2/Runx1 localization at the nucleus in a mouse c-Kit$^+$ HSPC (upper panels) and STAG2/RUNX1 localization at the nucleus in a K562 cell line (middle panels). The dotted white box indicates the magnified region shown in the inset (Scale bars: 1μm). The images were obtained using a LSM880 Airy scan super-resolution microscope (Zeiss). Lower panel: Quantification of the colocalization of Stag2-Runx1 in mouse c-Kit$^+$ HSPCs and colocalization of STAG2-RUNX1 in K562 cell lines. The dots indicate the percentages of the areas

of Stag2 (STAG2)-Runx1 (RUNX1) double positive spots among total areas of Stag2 (STAG2) positive spots. ****p<0.0001, two-sided Wilcoxon rank-sum test (n = 15 from three biological replicates). **D**, Average ChIP-seq read intensities of Stag1 and Ctcf in WT- and SKO-derived HSPCs around CC-I (blue) and CC-II (green) sites (left panels) and *P*-values for comparison between WT and SKO across each bin (right panels). **E**, Schematic representation representing the preferential binding of Stag2-cohesin to active enhancers together with Runx1. *P*-values were calculated by one-sided Wilcoxon rank-sum test comparing the ChIP-intensities in each bin in (**B**) and (**D**). Horizontal dashed lines indicate *P* = 0.05 in (**B**) and (**D**).

Figure 5. Stag2/Runx1 codeficiency alters chromatin architectures and disrupts enhancer-promoter loops.

A, Number of cohesin peaks (CC-I or CC-II) within topologically-associating domains (TADs) located in genomic compartment A (A-TADs) or B (B-TADs). *P*-values were calculated by two-sided Wilcoxon rank-sum test. **B**, Number of DEGs between WT- and SKO/RKO/DKO-transplanted LSK cells (FDR < 0.05) or other genes (stable) located in A- or B-TADs. *P*-value was calculated by Fisher's exact test. **C**, Average differential changes in Hi-C contacts within a subset of size-normalized A-TADs, visualized as log2 ratio indicated in the color scale. **D**, Average differential changes in Hi-C contacts within each hierarchical level of size-normalized TADs, showing the disruption of short-range interactions particularly within smaller sub-TADs in SKO, and more prominent in DKO. Hierarchical TADs were called using GMAP, and each level of TADs indicated in the upper-left panel was separately analyzed. **E**, Violin plots showing the size distribution of CC-I or CC-II loops with median and quartiles. *P*-value was calculated by two-sided Wilcoxon rank-sum test. Loops were classified by the presence of only one of either CC-I or CC-II sites at their anchors. **F**, Number of CC-I or CC-II loops independently identified using each Hi-C data. **G**, Summary of the major types of loops identified in each Hi-C data. Ctcf sites (CC-I sites) and active enhancers/promoters in which loops were anchored are displayed as purple, orange, and green circles, respectively. The loops between two sites are displayed as blue lines, and the width of the lines is proportional to the number of loops relative to WT. E, Enhancer; P, Promoter; C, CTCF; C-C, Ctcf-Ctcf; C-E, Ctcf-Enhancer: C-P, Ctcf-Promoter; E-E, Enhancer-Enhancer; E-P, Enhancer-Promoter; P-P, Promoter-Promoter. **H**, Genome browser snapshot demonstrating the Hi-C contacts, chromatin loops (upper panels), and ChIP-seq profiles (lower panels) in WT-/SKO-/RKO-/DKO-transplanted HSPCs at the *Wdr5* gene (a group IV gene in

Fig. 6A) locus. The arcs below each Hi-C contact map show the loops identified in the corresponding Hi-C data, and the E-P loop anchored at both promoter of Wdr5 and active enhancer was indicated as blue color. The dotted white box indicates the magnified region shown on the right. Color scale intensities of Hi-C heatmaps are shown in KR-normalized Hi-C contacts. Note that the E-P loop anchored at both promoter of Wdr5 and active enhancer was weakened in SKO, and more prominently in DKO (blue arrows). **I**, An alluvial plot demonstrating the proportion of CC-II sites having loops in WT which retained or lost loops in SKO and DKO. Red sites lost loops in DKO, and green sites retained loops in DKO. **J**, A classification scheme of CC-II sites with loops identified in WT for the analysis in (**K**) and (**L**). **K**, Median ChIP-seq intensities of various factors at each group of CC-II sites shown in (**J**). Color scales are normalized along each row. **L**, Proportions of numbers of co-bound 10 TFs (Asxl1, Fli1, Gata2, Gfi1b, Lmo2, Lyl1, Meis1, Pu1, Runx1, and Scl) at each group of CC-II sites shown in (**J**). **M**, Schematic representation depicting the characteristics of loops susceptible to Stag2/Runx1 loss. **** $P < 0.0001$.

Figure 6. Molecular features of transcriptional vulnerability to Stag2/Runx1 codeficiency. **A**, K-means clustering analysis of DEGs between WT- and SKO/RKO/DKO-derived LSK cells in RNA-seq datasets (FDR < 0.05). Color scales are normalized along each row. **B**, Box plots showing expression changes of each DEG group in SKO/RKO/DKO-derived LSK cells compared with WT. The vertical axis represents the log2(FC) in the indicated genotype and DEG group. **C**, Expression specificity of each DEG group across diverse hematopoietic lineages. Average expression levels of genes in the indicated DEG groups in each hematopoietic lineage are shown. Mouse expression datasets of diverse hematopoietic lineages are from Haemopedia RNA-seq datasets. Color scales are normalized along each row. **D**, Super-enhancers (SEs) and typical enhancers (TEs) identified by the standard ROSE algorithm using H3K27ac ChIP-seq intensities in HSPCs. **E**, Box plots showing expression changes of SE- and TE-associated genes in SKO/RKO/DKO-derived LSK cells compared with WT. *P*-values were calculated by one-sided Wilcoxon rank-sum test comparing SE genes vs TE genes. **F**, Box plots showing expression levels of Hoxa family genes in WT/SKO/RKO/DKO-derived LSK cells. *P*-values (vs WT) were calculated with edgeR package. **G**, Enrichment of known TF motifs in the ATAC-seq peaks that gained (left panel) or lost (right panel) accessibility in DKO-derived LSK cells compared with WT. The sorted motif rank and –log10(*P*-value) of a motif enrichment test using stable peaks as backgrounds are indicated in horizontal and vertical axis, respectively. **H**, Frequencies of differentially accessible ATAC-seq

peaks in SKO/RKO/DKO-derived LSK cells compared with WT (FDR < 0.05) near genes in the indicated DEG group. **I**, Box plots showing Pol II pausing indices of genes in each DEG group. **J**, Number of E-P loops anchored at the promoters of genes in the indicated DEG groups. The vertical axis represents the relative number of loops in WT/SKO/RKO/DKO-derived HSPCs to WT. **K**, Box plots showing Ser5-P Pol II ChIP-seq intensities in the promoter proximal regions of genes in each DEG group in WT/SKO/RKO/DKO-derived HSPCs. * $P < 0.05$; ** $P < 0.01$; *** $P < 0.001$; **** $P < 0.0001$.

Figure 7. Shared transcriptome changes in human and mice. **A**, Comparison of transcriptome changes in mouse model, three human MDS/AML, and HL-60 cell line datasets using enrichment map analysis based on GSEA results. NES values in cohesin-mutated MDS/AML cases compared with cohesin-WT cases in three independent cohort (6,33,34) are indicated in the upper left, lower left, and bottom of each circle, and those in SKO of HL-60 cell lines and LSK cells compared with WT are indicated in the upper right and lower right of each circle, respectively. Each node indicates a gene set of GSEA. The size of each node indicates the number of genes in each gene set, and the color scale indicates the NES value. The width of edge indicates the overlap size of gene sets. **B**, Box plots showing expression levels of HOXA family genes in human AML patients with 0/1/≥2 mutations in *SRSA* genes. *P*-values (vs no mutations in *SRSA* genes) were calculated with edgeR package. **C**, MSigDB overlap analysis between high-pausing genes and hallmark gene sets in MSigDB. FDR *q*-values were from MSigDB overlap analysis. Pathways which are significant ($q < 0.01$) in either dataset are shown. **D**, Cumulative probability distributions of expression changes (log2FC) of genes grouped by pausing index (PI) in cohesin-mutated cases (vs WT) in RNA-seq datasets of AML (33). *P*-values (vs genes with PI no more than 10) were calculated by one-sided Wilcoxon rank-sum test. **E-F**, Left panels: Box plots showing expression changes (log2FC) of genes grouped by PI according to the number of *SRSA* mutations (0/1/≥2) (**E**) or mutations in *STAG2* with/without the other *SRSA* mutations (*RUNX1*, *SRSF2*, and/or *ASXL1*) (**F**) in RNA-seq datasets of AML (33). Right panels show cumulative probability distribution of expression changes (log2FC) shown in left panels. *P*-values were calculated by one-sided Wilcoxon rank-sum test. * $P < 0.05$; ** $P < 0.01$; *** $P < 0.001$; **** $P < 0.0001$.

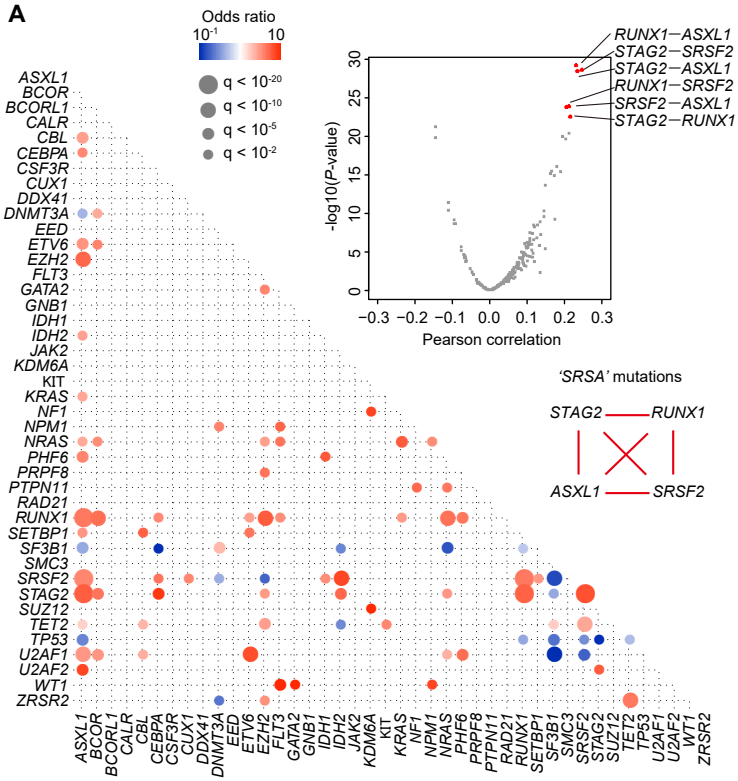
A
Odds ratio
10-1
10
q < 10-20
q < 10-10
q < 10-5
q < 10-2
ASXL1
BCOR
BCORL1
CALR
CBL
CEBPA
CSF3R
CUX1
DDX41
DNMT3A
EED
ETV6
EZH2
FLT3
GATA2
GNB1
IDH1
IDH2
JAK2
KDM6A
KIT
KRAS
NF1
NPM1
NRAS
PHF6
PRPF8
PTPN11
RAD21
RUNX1
SETBP1
SF3B1
SMC3
SRSF2
STAG2
SUZ12
TET2
TP53
U2AF1
U2AF2
WT1
ZRSR2
RUNX1—ASXL1
STAG2—SRSF2
STAG2—ASXL1
RUNX1—SRSF2
SRSF2—ASXL1
STAG2—RUNX1
-log10(P-value)
Pearson correlation
'SRSA' mutations
STAG2
RUNX1
ASXL1
SRSF2

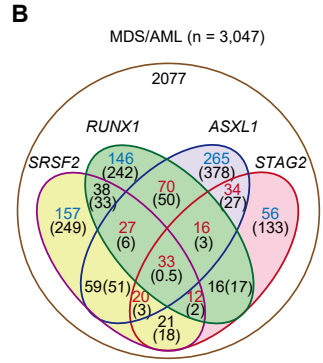
B
MDS/AML (n = 3,047)
2077
RUNX1
ASXL1
SRSF2
STAG2
146 (242)
265 (378)
157 (249)
38 (33)
70 (50)
34 (27)
56 (133)
27 (6)
16 (3)
33 (0.5)
59(51)
20 (3)
12 (2)
16(17)
21 (18)

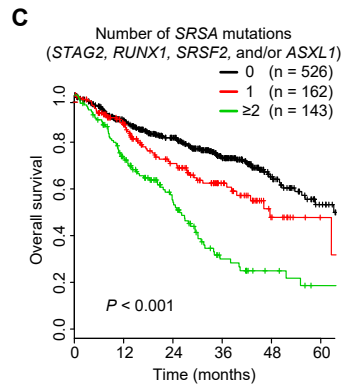
C
Number of SRSA mutations
(STAG2, RUNX1, SRSF2, and/or ASXL1)
0 (n = 526)
1 (n = 162)
≥2 (n = 143)
Overall survival
P < 0.001
Time (months)

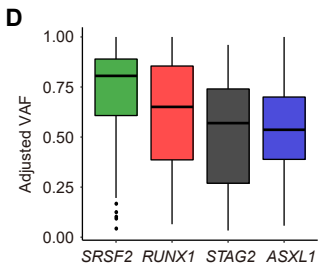
D
Adjusted VAF
SRSF2
RUNX1
STAG2
ASXL1

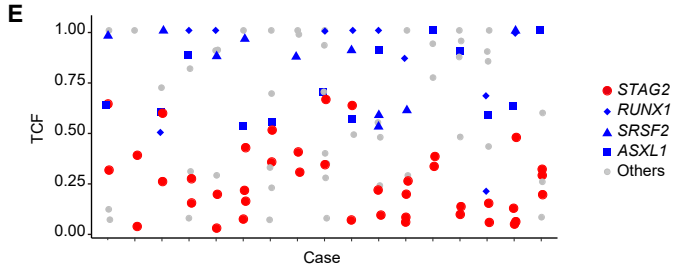
E
TCF
Case
STAG2
RUNX1
SRSF2
ASXL1
Others

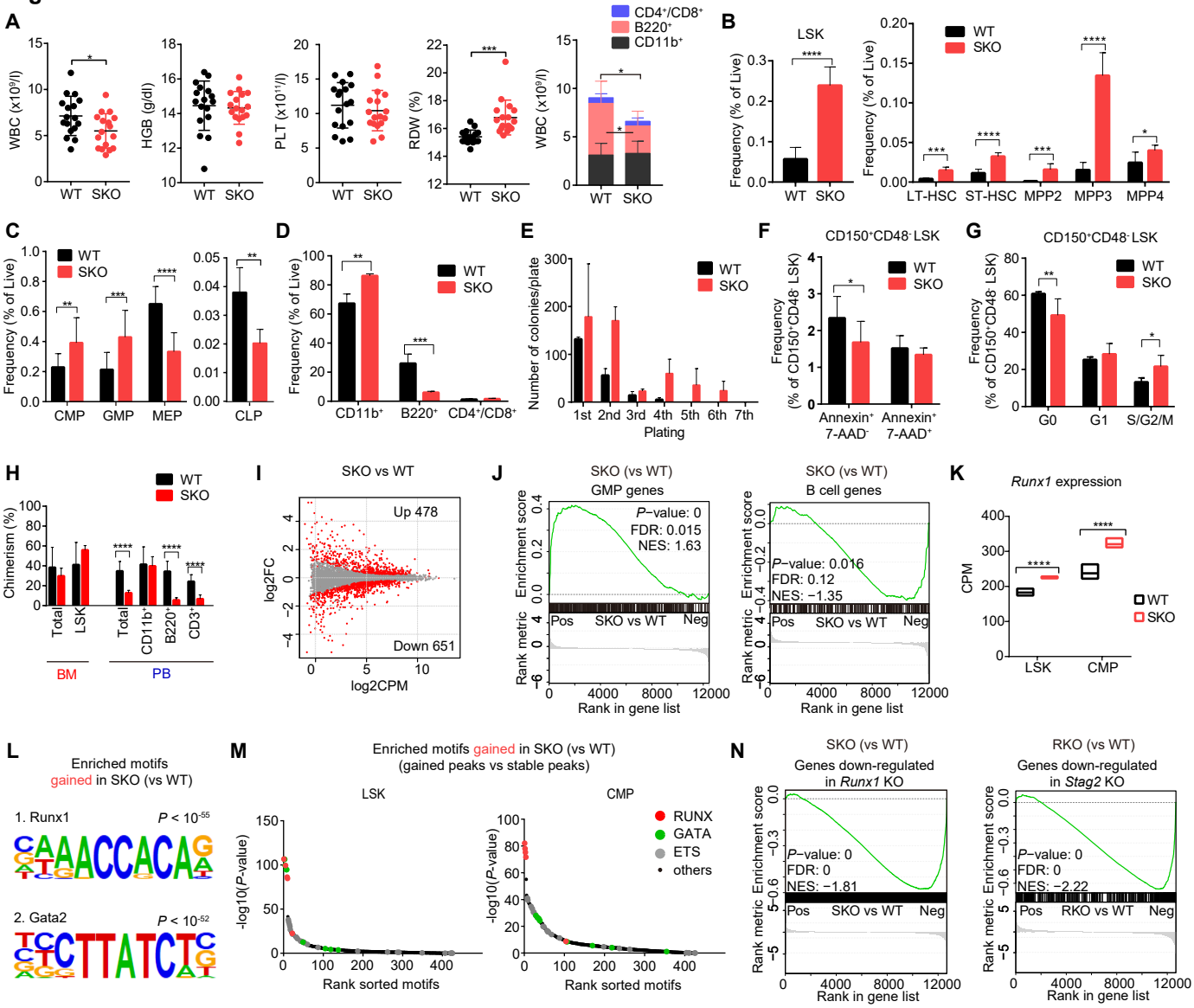
A
WBC (x10⁹/l)
HGB (g/dl)
PLT (x10¹¹/l)
RDW (%)
WBC (x10⁹/l)
CD4⁺/CD8⁺
B220⁺
CD11b⁺
WT
SKO
B
LSK
Frequency (% of Live)
LT-HSC
ST-HSC
MPP2
MPP3
MPP4
C
CMP
GMP
MEP
CLP
D
CD11b⁺
B220⁺
CD4⁺/CD8⁺
E
Number of colonies/plate
1st 2nd 3rd 4th 5th 6th 7th
Plating
F
CD150⁺CD48⁻LSK
Frequency (% of CD150⁺CD48⁻LSK)
Annexin⁺ 7-AAD⁻
Annexin⁺ 7-AAD⁺
G
G0
G1
S/G2/M
H
Chimerism (%)
Total
LSK
CD11b⁺
B220⁺
CD3⁺
BM
PB
I
SKO vs WT
Up 478
Down 651
log2FC
log2CPM
J
SKO (vs WT)
GMP genes
P-value: 0
FDR: 0.015
NES: 1.63
B cell genes
P-value: 0.016
FDR: 0.12
NES: −1.35
Enrichment score
Rank metric
Pos
SKO vs WT
Neg
Rank in gene list
K
Runx1 expression
CPM
LSK
CMP
L
Enriched motifs gained in SKO (vs WT)
1. Runx1
P < 10⁻⁵⁵
2. Gata2
P < 10⁻⁵²
M
Enriched motifs gained in SKO (vs WT)
(gained peaks vs stable peaks)
LSK
CMP
-log10(P-value)
Rank sorted motifs
RUNX
GATA
ETS
others
N
SKO (vs WT)
Genes down-regulated in Runx1 KO
P-value: 0
FDR: 0
NES: −1.81
RKO (vs WT)
Genes down-regulated in Stag2 KO
NES: −2.22
RKO vs WT

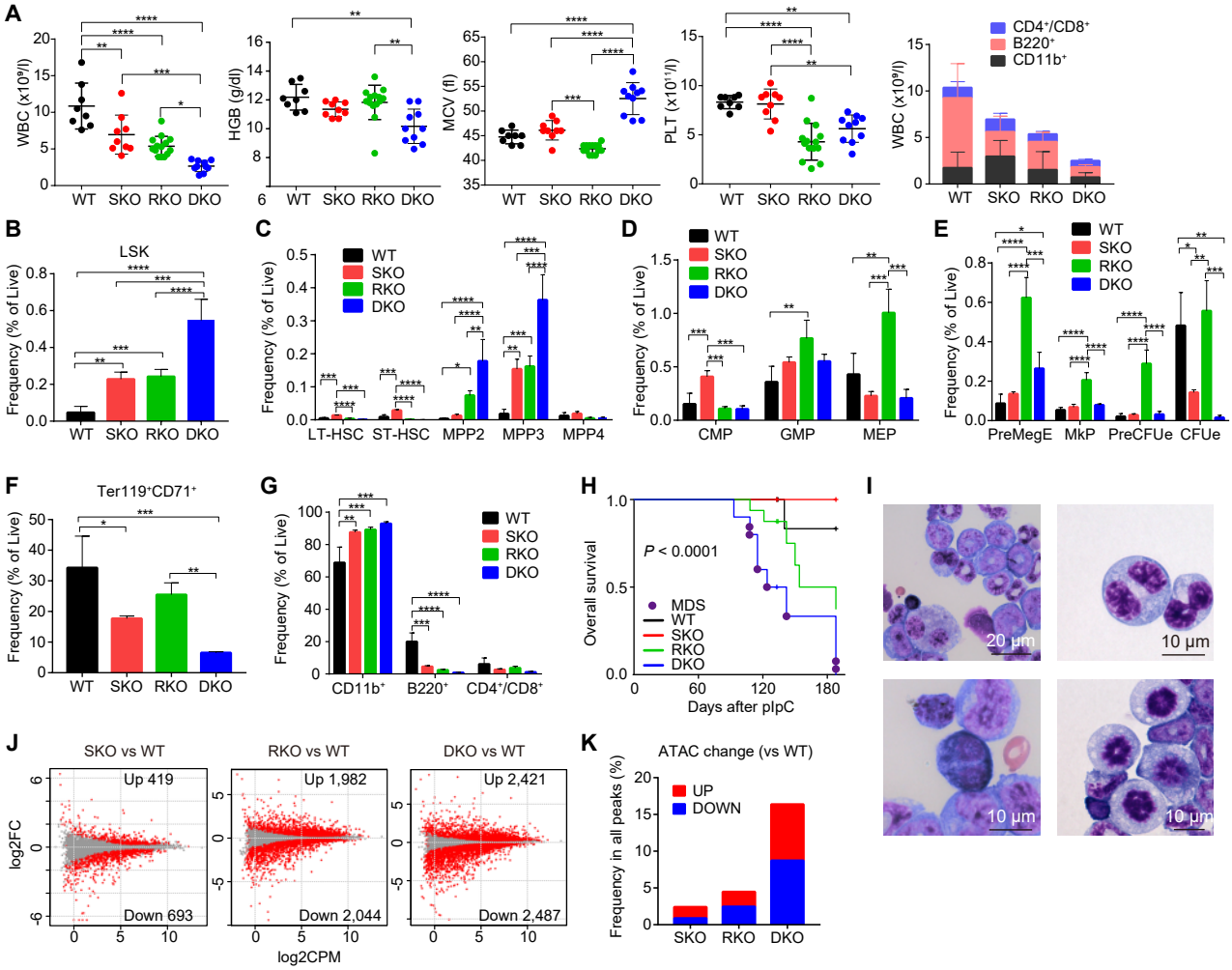
A
WBC (x10⁹/l)
HGB (g/dl)
MCV (fl)
PLT (x10¹²/l)
WBC (x10⁹/l)
CD4⁺/CD8⁺
B220⁺
CD11b⁺
WT SKO RKO DKO
B
LSK
Frequency (% of Live)
C
LT-HSC ST-HSC MPP2 MPP3 MPP4
D
CMP GMP MEP
E
PreMegE MkP PreCFUe CFUe
F
Ter119⁺CD71⁺
G
CD11b⁺ B220⁺ CD4⁺/CD8⁺
H
Overall survival
P < 0.0001
MDS
Days after pIpC
I
20 μm
10 μm
J
SKO vs WT
RKO vs WT
DKO vs WT
Up 419
Down 693
Up 1,982
Down 2,044
Up 2,421
Down 2,487
log2FC
log2CPM
K
ATAC change (vs WT)
UP
DOWN
Frequency in all peaks (%)

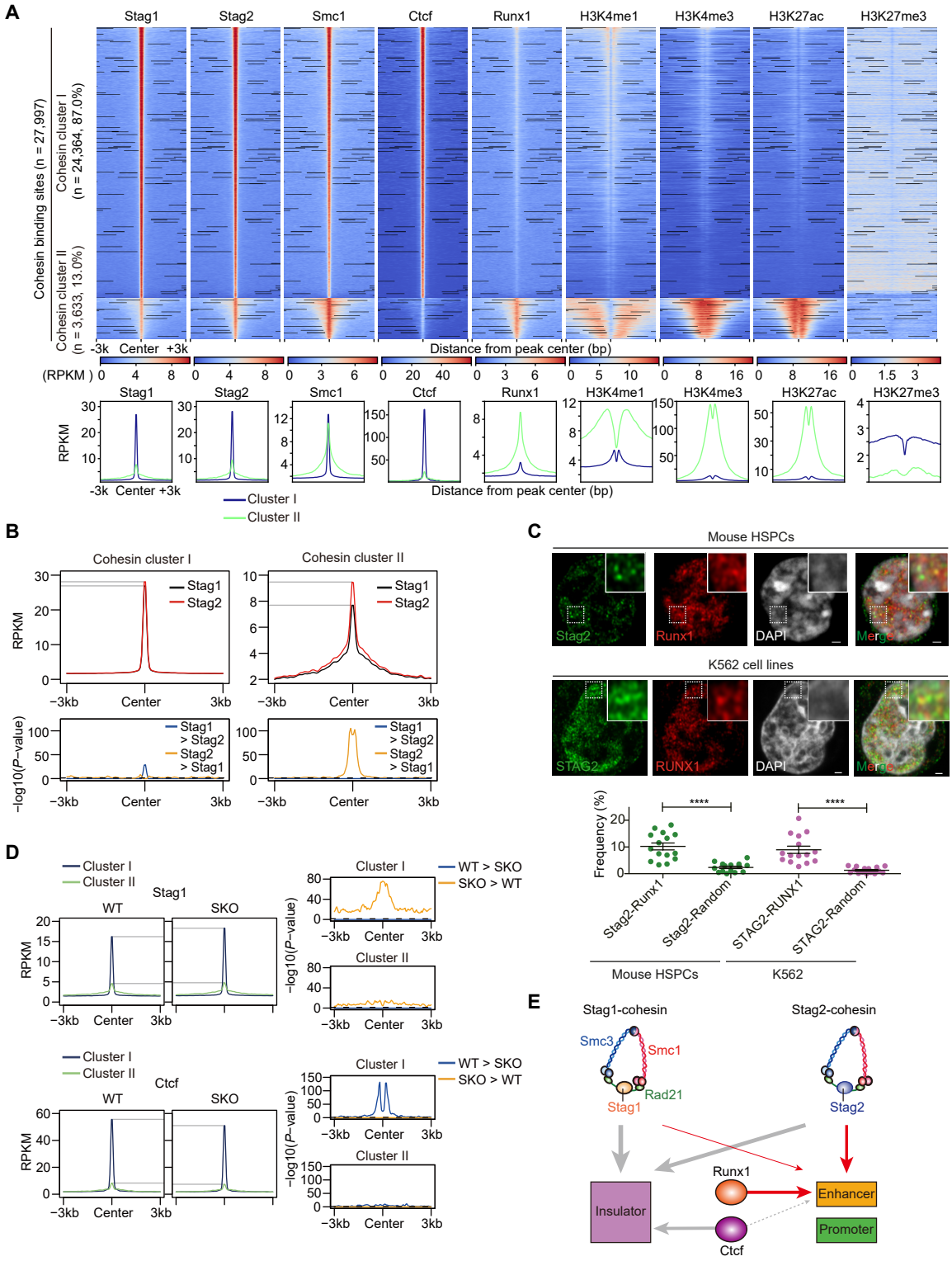
A
Stag1
Stag2
Smc1
Ctcf
Runx1
H3K4me1
H3K4me3
H3K27ac
H3K27me3
Cohesin binding sites (n = 27,997)
Cohesin cluster I (n = 24,364, 87.0%)
Cohesin cluster II (n = 3,633, 13.0%)
-3k Center +3k
Distance from peak center (bp)
(RPKM)
RPKM
Cluster I
Cluster II
B
Cohesin cluster I
Cohesin cluster II
Stag1
Stag2
−log10(P−value)
Stag1 > Stag2
Stag2 > Stag1
−3kb
Center
3kb
C
Mouse HSPCs
K562 cell lines
Stag2
Runx1
DAPI
Merge
STAG2
RUNX1
Frequency (%)
****
Stag2-Runx1
Stag2-Random
STAG2-RUNX1
STAG2-Random
Mouse HSPCs
K562
D
Cluster I
Cluster II
Stag1
WT
SKO
RPKM
−log10(P−value)
WT > SKO
SKO > WT
Ctcf
E
Stag1-cohesin
Stag2-cohesin
Smc3
Smc1
Rad21
Stag1
Stag2
Runx1
Insulator
Enhancer
Promoter
Ctcf

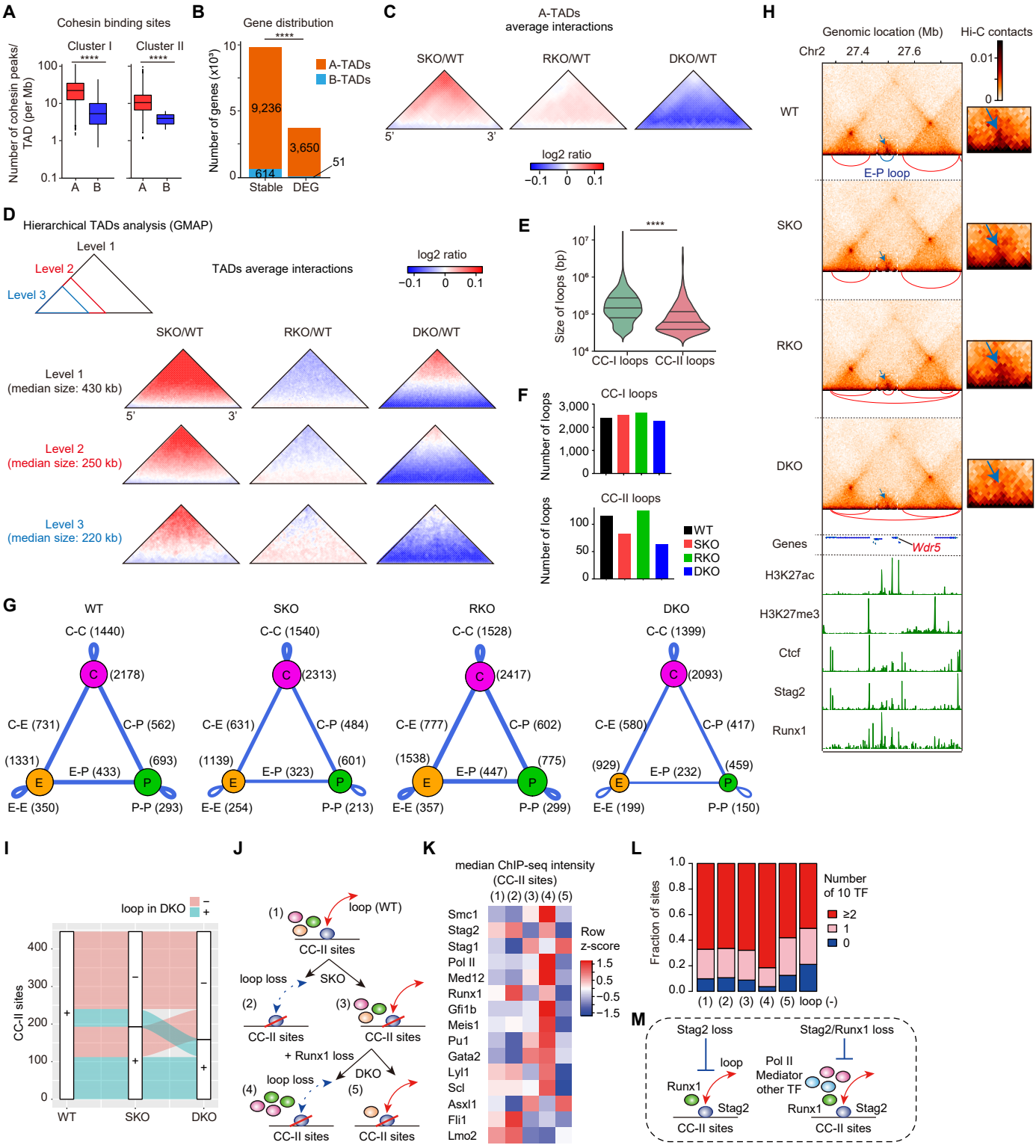
A
Cohesin binding sites
Cluster I
Cluster II
Number of cohesin peaks/ TAD (per Mb)
B
Gene distribution
A-TADs
B-TADs
Number of genes (x10³)
9,236
614
3,650
51
Stable
DEG
C
A-TADs average interactions
SKO/WT
RKO/WT
DKO/WT
log2 ratio
D
Hierarchical TADs analysis (GMAP)
Level 1
Level 2
Level 3
TADs average interactions
Level 1 (median size: 430 kb)
Level 2 (median size: 250 kb)
Level 3 (median size: 220 kb)
E
Size of loops (bp)
CC-I loops
CC-II loops
F
CC-I loops
CC-II loops
Number of loops
WT
SKO
RKO
DKO
G
WT
SKO
RKO
DKO
C-C (1440)
C-C (1540)
C-C (1528)
C-C (1399)
(2178)
(2313)
(2417)
(2093)
C-E (731)
C-P (562)
E-P (433)
E-E (350)
P-P (293)
C-E (631)
C-P (484)
E-P (323)
E-E (254)
P-P (213)
C-E (777)
C-P (602)
E-P (447)
E-E (357)
P-P (299)
C-E (580)
C-P (417)
E-P (232)
E-E (199)
P-P (150)
H
Genomic location (Mb)
Hi-C contacts
Chr2
27.4
27.6
WT
SKO
RKO
DKO
E-P loop
Genes
Wdr5
H3K27ac
H3K27me3
Ctcf
Stag2
Runx1
I
loop in DKO
CC-II sites
WT
SKO
DKO
J
loop (WT)
loop loss
SKO
+ Runx1 loss
DKO
K
median ChIP-seq intensity (CC-II sites)
Smc1
Stag2
Stag1
Pol II
Med12
Runx1
Gfi1b
Meis1
Pu1
Gata2
Lyl1
Scl
Asxl1
Fli1
Lmo2
Row z-score
L
Fraction of sites
Number of 10 TF
loop (-)
M
Stag2 loss
loop
Runx1
Stag2
Stag2/Runx1 loss
Pol II Mediator other TF

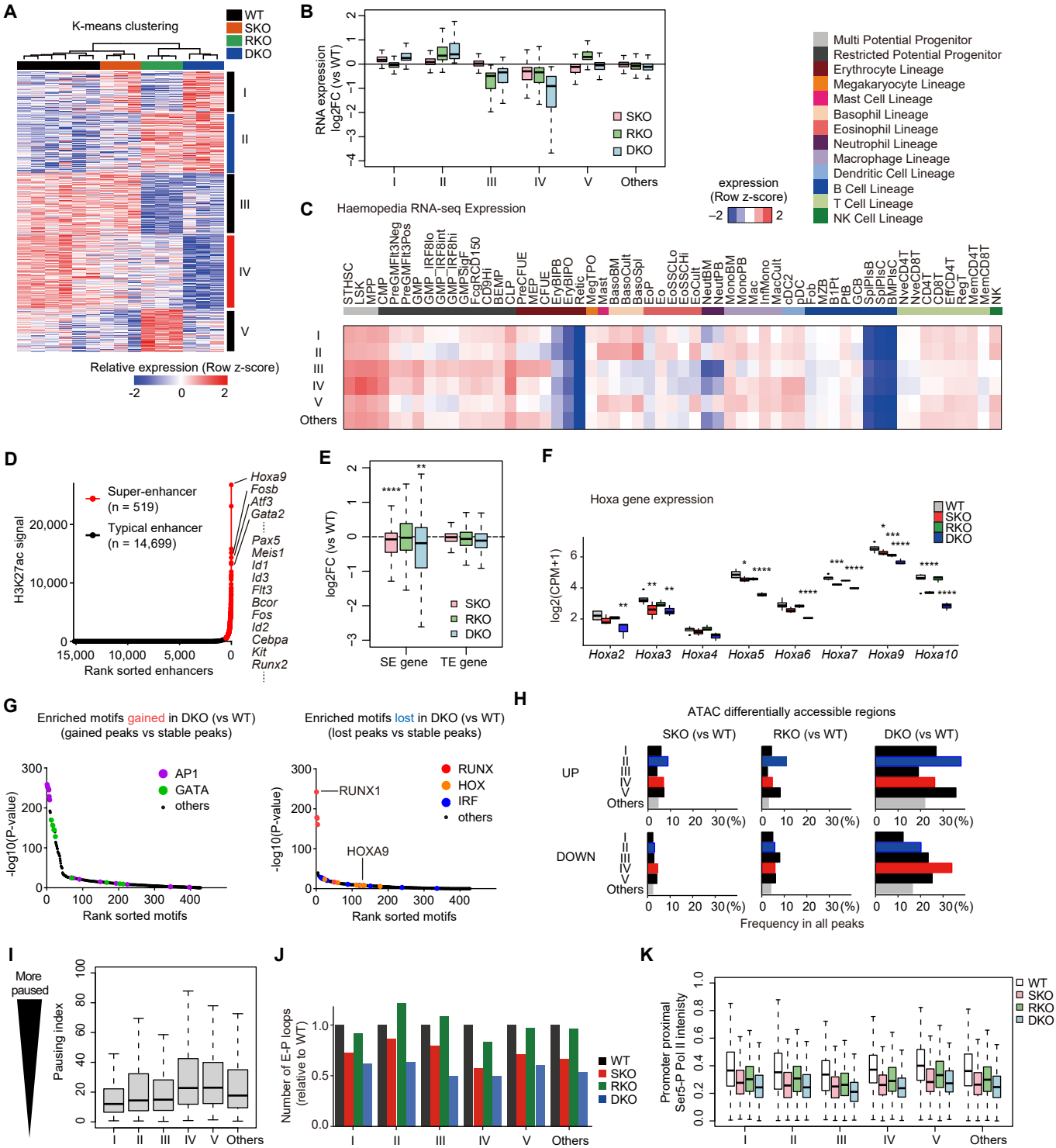
A
K-means clustering
WT
SKO
RKO
DKO
I
II
III
IV
V
Relative expression (Row z-score)
-2 0 2
B
RNA expression log2FC (vs WT)
SKO
RKO
DKO
I II III IV V Others
Multi Potential Progenitor
Restricted Potential Progenitor
Erythrocyte Lineage
Megakaryocyte Lineage
Mast Cell Lineage
Basophil Lineage
Eosinophil Lineage
Neutrophil Lineage
Macrophage Lineage
Dendritic Cell Lineage
B Cell Lineage
T Cell Lineage
NK Cell Lineage
expression (Row z-score)
-2 2
C
Haemopedia RNA-seq Expression
STHSC LSK MPP CMP PreGMFlt3Neg PreGMFlt3Pos GMP GMP_IRF8lo GMP_IRF8int GMP_IRF8hi GMPSigF FcgRCD150 CD9Hi BEMP CLP PreCFUE MEP CFUE EryBlPB EryBlPO EryPl Retic MegTPO Mast BasoBM BasoCult BasoSpl EoP Eo EoSSCLo EoSSCHi EoCult NeutBM NeutPB MonoBM MonoPB Mac InfMono MacCult cDC2 pDC Fob MZB B1Pt PtB GCB SplPlsB SplPlsC BMPlsC NveCD4T NveCD8T CD4T CD8T EffCD4T Reg1 MemCD4T MemCD8T NK
I
II
III
IV
V
Others
D
Super-enhancer (n = 519)
Typical enhancer (n = 14,699)
H3K27ac signal
20,000
10,000
0
15,000 10,000 5,000 0
Rank sorted enhancers
Hoxa9
Fosb
Atf3
Gata2
Pax5
Meis1
Id1
Id3
Flt3
Bcor
Fos
Id2
Cebpa
Kit
Runx2
E
log2FC (vs WT)
SKO
RKO
DKO
SE gene
TE gene
F
Hoxa gene expression
WT
SKO
RKO
DKO
log2(CPM+1)
Hoxa2 Hoxa3 Hoxa4 Hoxa5 Hoxa6 Hoxa7 Hoxa9 Hoxa10
G
Enriched motifs gained in DKO (vs WT)
(gained peaks vs stable peaks)
AP1
GATA
others
-log10(P-value)
Rank sorted motifs
Enriched motifs lost in DKO (vs WT)
(lost peaks vs stable peaks)
RUNX
HOX
IRF
others
RUNX1
HOXA9
H
ATAC differentially accessible regions
SKO (vs WT)
RKO (vs WT)
DKO (vs WT)
UP
DOWN
I II III IV V Others
Frequency in all peaks
I
More paused
Pausing index
J
Number of E-P loops (relative to WT)
WT
SKO
RKO
DKO
K
Promoter proximal Ser5-P Pol II intensity
WT
SKO
RKO
DKO

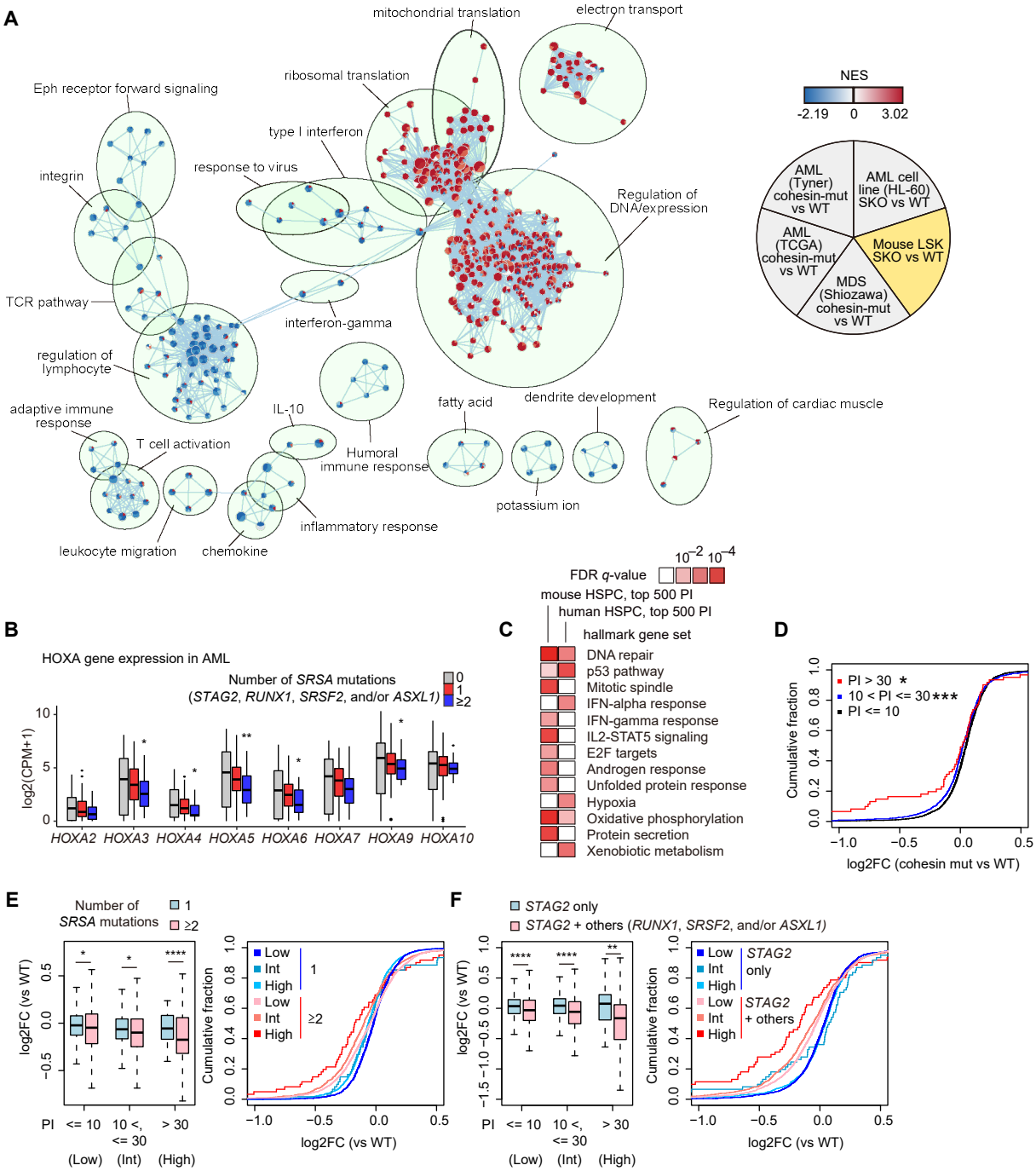
A
mitochondrial translation
electron transport
ribosomal translation
Eph receptor forward signaling
type I interferon
integrin
response to virus
Regulation of DNA/expression
TCR pathway
interferon-gamma
regulation of lymphocyte
adaptive immune response
IL-10
fatty acid
dendrite development
Regulation of cardiac muscle
T cell activation
Humoral immune response
potassium ion
inflammatory response
leukocyte migration
chemokine
NES
-2.19 0 3.02
AML (Tyner) cohesin-mut vs WT
AML cell line (HL-60) SKO vs WT
AML (TCGA) cohesin-mut vs WT
Mouse LSK SKO vs WT
MDS (Shiozawa) cohesin-mut vs WT
FDR q-value
10−2 10−4
mouse HSPC, top 500 PI
human HSPC, top 500 PI
hallmark gene set
DNA repair
p53 pathway
Mitotic spindle
IFN-alpha response
IFN-gamma response
IL2-STAT5 signaling
E2F targets
Androgen response
Unfolded protein response
Hypoxia
Oxidative phosphorylation
Protein secretion
Xenobiotic metabolism
B
HOXA gene expression in AML
Number of SRSA mutations
(STAG2, RUNX1, SRSF2, and/or ASXL1)
0
1
≥2
log2(CPM+1)
HOXA2 HOXA3 HOXA4 HOXA5 HOXA6 HOXA7 HOXA9 HOXA10
C
D
PI > 30 *
10 < PI <= 30 ***
PI <= 10
Cumulative fraction
log2FC (cohesin mut vs WT)
E
Number of SRSA mutations
1
≥2
log2FC (vs WT)
PI <= 10 10 <, <= 30 > 30
(Low) (Int) (High)
Low
Int
High
Cumulative fraction
log2FC (vs WT)
F
STAG2 only
STAG2 + others (RUNX1, SRSF2, and/or ASXL1)
STAG2 only
STAG2 + others

Supplementary Information

*** Supplementary Methods**

*** Supplementary Figures**

*** Inventory of Supplementary Tables**

Supplementary Methods

Quantitative reverse transcription PCR (qRT-PCR)

Total RNAs were extracted from mouse nucleated BM cells with Rneasy Mini kit (QIAGEN), and subject to reverse transcriptase reaction using ReverTra Ace qPCR RT Master Mix with gDNA Remover (TOYOBO). cDNA was amplified with SYBR Premix Ex Taq II (TaKaRa) using LightCycler480 system (Roche Diagnostics). The expression of 18s rRNA was used for normalization of the results. The primer sets for qPCR are as follows: 5'-TGGAAGATGATGAAGAGCCAAT-3' and 5'-TCGGGCTTCAGTTCTGTTCT-3' for *Stag2*, 5'-GGACACCGTAATTTCCCTTTTG-3' and 5'-TCATTGGCTCTCTTCCCAATC-3' for *Stag1*, 5'-GCTCTGGTAAGTCAAATCTCATGGA-3' and 5'-CCCTCAGGTTGCTGGTCTTTT-3' for *Smc1*, 5'-GCTGGCGGGCAACAGTGAAC-3' and 5'-AGCCAACCTCGCAATTCCTCGC-3' for *Smc3*, 5'-CCTCAGCAGGTAGAGCAAATGG-3' and 5'-GCATCTGCTGAGTGCGTTTGTT-3' for *Rad21*, and 5'-GCAATTATTCCCCATGAACG-3' and 5'-GGGACTTAATCAACGCAAGC-3' for 18s.

Western blotting

Nucleated BM cells were isolated using a density gradient solution (Histopaque-1077, Sigma-Aldrich) and were lysed in RIPA lysis buffer. SDS-PAGE and western blotting were performed following the standard protocol. Antibodies used are as follows: SMC1 (Abcam, ab9262), SMC3 (Abcam, ab9263), RAD21 (Abcam, ab992), STAG2 (Novus, NBP1-30472 (for mouse), or Santa Cruz, sc-81852 (for human)), and RUNX1 (Active Motif, 39000 (for mouse), or Santa Cruz, sc-365644 (for human)), and Actin (Santa Cruz, sc1616).

Co-immunoprecipitation

Mouse 32Dcl3 cell line or human K562 cell line were used for co-immunoprecipitation analysis as previously described (1) with minor modifications. Nuclei were prepared using NE-PER Nuclear and Cytoplasmic Extraction Kit (Thermo Scientific) according to the manufacturer's protocol. Immunoprecipitation was performed using NHS Mag Sepharose (GE Healthcare) magnetic beads conjugated with SMC1 (Abcam, ab9262) or SMC3 (Abcam, ab9263) antibody and incubated with the cell extracts overnight at 4℃. After washing with lysis buffer, the beads were suspended with SDS-PAGE sample buffer.

Histology and cytology

For histological analysis, tissue samples were fixed in 4% paraformaldehyde, embedded in paraffin, sectioned and stained with hematoxylin and eosin. For cytological analysis, cytospin preparations of BM samples (Thermo Scientific Cytospin 4) or PB smears were stained using the May–Grünwald–Giemsa staining method.

Immunostaining

Purified mouse c-Kit$^+$ HSPCs and K562 cell lines were transferred onto Poly-D-Lysine coated cover glass and fixed for 20 min in 4% formaldehyde/PBS. Cells were then permeabilized in 0.5% Triton X-100/PBS for 10 min and incubated for 30 min in 5% skim milk/PBST (0.1% Tween-20 in PBS) for blocking. For STAG2 and RUNX1 staining, cells were incubated overnight at 4℃ at an antibody dilution of 1:50 for mouse monoclonal anti-STAG2 (Santa Cruz, sc-81852) and 1:200 for rabbit monoclonal anti-Runx1 (Abcam, ab92336). Subsequent staining with Alexa Fluor 488 donkey anti-mouse IgG (H+L) (Invitrogen A-21202) and Alexa Fluor 594 goat anti-rabbit IgG (H+L) (Invitrogen A-11037) was performed for 60 min at room temperature at a dilution of 1:1000. Stained cells were treated in DAPI solution (1μg/ml) for 30 min and were mounted with ProLong Gold antifade reagents (Invitrogen).

Microscopy and data analysis

Super-resolution images were obtained using LSM880 Airy scan (Zeiss) with a 100x oil objective lens (NA 1.46, alpha Plan-Apochromat 100x/1.46 Oil Ph3 M27). For colocalization analysis, random 4 μm x 4 μm squares in DAPI positive regions were cropped from central 5 images in z-stack images. Spots segmentation was performed using auto local threshold (MidGrey method). For quantification of the random colocalization as negative control, each square image was flipped horizontally and vertically. These steps were performed using ImageJ. Appropriate sample size was checked by G*Power 3.1 (2,3).

Single-cell differentiation assay

Single-cell differentiation assay was performed as previously described (4) with minor modifications. c-Kit$^+$ HSPCs were transduced by FLAG-tagged Hoxa9 or mock in the pGCDNsam-IRES-EGFP vector, and GFP-positive cells were sorted at one cell per well into a 96-well plate of which each well contains IMDM with 10% FBS, 2-β-mercaptoethanol, 10 ng/ml mouse SCF, TPO and IL-3, and 40 ng/ml human EPO. After 14 day-culture, each generated colony was subjected to FACS analysis and was classified to granulocyte-, monocyte-, and/or erythroid-containing colony if it contained > 10% of corresponding cells.

RNA-sequencing

RNA was extracted using RNeasy Mini Kit (QIAGEN) or NucleoSpin RNA XS (Macherey-Nagel). Libraries for RNA-seq were prepared using the NEBNext Ultra RNA Library Prep kit for Illumina (New England BioLabs) and were subjected to sequencing using HiSeq 2500 or NovaSeq 6000 instrument (Illumina) with a standard 100-150-bp paired-end protocol as previously described (5). RNA-seq experiments were performed in two or more biological replicates. The sequencing reads were aligned to the reference genome (hg19 or mm9) using STAR (v2.5.3) (6). Reads on each refSeq gene were counted with featureCounts (v1.5.3) (7) from Subread package, and edgeR package in R (8) was used to identify the differentially expressed genes with FDR threshold of 0.05 and to generate the multidimensional scaling (MDS) plot. The analysis was performed in genes expressed at >1 count per million (CPM) in two or more samples, and generalized linear models were used to compare gene expression data. Differentially expressed genes between WT- and SKO/RKO/DKO-transplanted LSK cells (FDR < 0.05) were grouped into 5 clusters using k-means clustering. Motif analysis was performed using the HOMER findMotifs.pl program (9). For the gene promoters, enrichment of known transcription factor motifs was analyzed from -2,000 to +1,000 bp from the transcription start site (TSS), and genes without significant expression changes were used as backgrounds. Gene ontology (GO) analysis was performed using Database for Annotation, Visualization, and Integrated Discovery (DAVID; http://david.abcc.ncifcrf.gov). MSigDB overlap analysis was performed using MSigDB database and hallmark gene sets (https://www.gsea-msigdb.org/gsea/msigdb/index.jsp). Tissue Specific Expression Analysis (TSEA) was performed with TSEA tool (http://genetics.wustl.edu/jdlab/tsea/) (10). RNA expression analysis in the hematopoietic system was carried out using Haemopedia RNA-seq datasets (11), and averages of log2 (TPM + 1) values of each gene set were calculated for each cell type. GSEA (v2.2.4) (12) was used to determine the sets of genes that are significantly different between groups. Gene sets characteristic of GMP and B-lymphocytes were generated using datasets from previous reports (13,14). For network analysis, GSEA analysis was performed with gene sets downloaded from https://www.baderlab.org/Software/EnrichmentMap (Human_GOBP_AllPathways_no_GO_iea_March_01_2018_symbol.gmt file). Enriched pathways were visualized using Enrichment Map (15) with the q-value < 0.05 and overlap similarity coefficient parameters > 0.5. For RNA-seq of human MDS/AML (16-18), reads aligned to the human reference genome (hg19) or counted read data were obtained and analyzed as described above. Human AML cases (17) were grouped into 2 clusters using genes with high pausing levels (pausing index >20) and k-means clustering. RNA-seq datasets used are described in **Supplementary Table S7**. Differentially expressed genes shown in **Fig. 2I** are described in **Supplementary Tables S8-9**. Differentially expressed genes shown in **Fig. 3J** are described in **Supplementary Tables S10-15**.

ChIP-sequencing

ChIP-seq experiments were performed using c-Kit$^+$ HSPCs or HL-60 cell lines. Cells were fixed in PBS with 1% formaldehyde (Thermo Fisher Scientific) for 10 min at room temperature with gentle mixing. The reaction was stopped by adding glycine solution (10x) (Cell Signaling Technology) and incubating for 5 minutes at room temperature, and the cells were washed in cold PBS twice. The cells were then processed with SimpleChIP Plus Sonication Chromatin IP Kit (Cell Signaling Technology) and Covaris E220 (Covaris) according to the manufacturer's protocol. The antibodies used for ChIP are as follows: STAG1 (Protein Tech, 14015-1-AP), STAG2 (Novus, NBP1-30472), SMC1 (Abcam, ab9262), CTCF (Cell Signaling Technology, D31H2), RUNX1 (Abcam, 23980), total Pol II (CST, D8L4Y), Ser5-P Pol II (Abcam, ab5408), H3K27ac (Cell Signaling Technology, D5E4), H3K27me3 (Cell Signaling Technology, C36B11), H3K4me1 (Cell Signaling Technology, D1A9), or H3K4me3 (Cell Signaling Technology, C42D8). After purification of ChIPed DNA, ChIP-seq libraries were constructed using ThruPLEX DNA-seq kit (Takara) according to the manufacturer's protocol, and then subjected to sequencing using HiSeq 2500 or NoveSeq 6000 (Illumina). ChIP-seq experiments were performed in two or more biological replicates with input controls. The sequencing reads were aligned to the reference genome (hg19 or mm9) using bowtie (v1.2.2) (19) following trimming of adapters and read tails to a total length of 50 base pairs using cutadapt. Duplicates and reads on blacklisted regions (ENCODE) were removed by Picard and bedtools, respectively. Peaks were called using MACS (v2.1.1) for each replicate individually with a *P*-value threshold of 1×10^{-3} unless otherwise specified, and overlapped peaks among replicates were regarded as consensus peak sets. Motif analysis and peak annotation were performed with HOMER. Super-enhancers were identified with H3K27ac ChIP-seq data in WT HSPCs using ROSE (20) with default parameters. Identified super-enhancers are described in **Supplementary Table S20**. Super-enhancers in human HSCs were previously described (21), and we used the dataset of BI_CD34_Primary_RO01536 for assignment of super-enhancer-associated genes. Calculation of ChIP signal intensities around peaks and generation of read density profile plots and heatmaps were performed using deeptools (22). In metaplot analysis, statistical significance was assessed with one-sided Wilcoxon rank-sum test at each bin. Visualization of sequence data was performed using IGV. For clustering of cohesin binding sites, we calculated logarithm of H3K27ac and Ctcf ChIP signal intensities summed up around ± 200 bp from centers of cohesin binding sites (Stag1 and/or Stag2 peaks) by deeptools, performed clustering using flowPeaks (23), and regarded the H3K27ac high clusters as cohesin cluster II and the others as cluster I. Binding profiles of cohesin components, Pol II, Mediator, and ten hematopoietic TFs were similarly calculated around ± 200 bp from centers of cohesin binding sites (**Fig. 5K**). For analysis of combinatorial binding of ten transcription factors (Asxl1, Fli1, Gata2, Gfi1b, Lmo2, Lyl1, Meis1, Pu1, Runx1, and Scl) (**Fig. 5L**), each peak was called using MACS (v1.4.2) with a *P*-value threshold of 1×10^{-5}, and number of transcription factors whose peaks overlapped with regions ± 500 bp around CC-II sites annotated to each group gene was counted.

We also used ChIP-seq datasets (10 TFs: Asxl1, Fli1, Gata2, Gfi1b, Lmo2, Lyl1, Meis1, Pu1, Runx1, Scl; Pol II, Med12 in mouse, Pol II in human (24-27)) in previous studies.

Hi-C

Hi-C experiments were performed using MboI restriction enzyme as previously described (28). Briefly, two million mouse c-Kit$^+$ HSPCs or HL-60 cells were crosslinked with 1% formaldehyde for 10 min at room temperature. Cells were permeabilized and chromatin was digested with MboI restriction enzyme, and the ends of restriction fragments were labeled with biotinylated nucleotides and ligated. After crosslink reversal, DNA was purified and sheared with Covaris M220 (Covaris). Then point ligation junctions were pulled down with streptavidin beads. Then libraries were constructed with Nextera Mate Pair Sample Preparation Kit (Illumina) according to the manufacturer's protocol, and subject to sequencing using NovaSeq 6000 (Illumina) with a standard 100- or 150-bp paired-end protocol. Hi-C experiments were performed in biological duplicates. The sequencing reads were processed using Juicer (28) and hg19 or mm10 reference genome. After filtering of reads, the average valid interactions per genotype resulted in 1.79 billion for mouse HSPCs and 1.66 billion for HL-60 cells. For comparative analysis, the valid interactions after filtering were randomly resampled and arranged in the number of the lowest sample. Contact matrices used for further analysis were created for each replicate as well as merged one by genotype and Knight-Ruiz (KR)-normalized with Juicer. Genomic compartmentalization (A or B compartments) was analyzed using Eigenvector (28) at 25kb resolution, and A-compartments were assigned to the genomic bin with positive eigenvector values as well as higher gene density and B-compartments were the opposite. The insulation score was calculated as previously described (29) at 5kb resolution, and visualized by deeptools. Loops were called at 5kb and 10kb resolutions using HICCUPS (28) and then merged to construct loop sets. Loops were classified into CC-I loops (whose anchors overlapped with at least one CC-I sites but not with CC-II) and CC-II loops (whose anchors overlapped with at least one CC-II but not CC-I sites). Loops whose anchors corresponded to the pairs of Ctcf (cohesin cluster-I sites), enhancers (H3K4me1 peaks overlapped with H3K27ac peaks in mouse or H3K27ac peaks excluding peaks overlapped with TSSs (± 2 kb) in human), and promoters (TSSs overlapped with H3K4me3 peaks) were counted, and plotted by igraph package in R software. Aggregated intensities of "peaks" (pixels corresponding to pairs of loop anchors in the contact matrices) were calculated using aggregate peak analysis (APA) (28) with -r 5000 -n 15 parameters, which calculates the sum of a series of submatrices around peaks derived from the contact matrix. Each of these submatrices is a pixel square centered at a single peak in the upper triangle of the contact matrix. Topologically associating domains (TADs) were called at 5kb resolution using Arrowhead (28). TAD boundaries were defined as +- 5kb from the 5'- or 3'- ends of TADs, and insides were regions insides of both boundaries. For aggregated TAD analysis, we selected TADs which did not enclose other TADs, and

were located in compartment A and in the size range 100-300 kb, got submatrices corresponding to TAD regions derived from the contact matrix, resized each of them into a 100 x 100 submatrix, and calculated the sum of size-normalized submatrices. We also performed hierarchical TADs analysis using rGMAP (30) at 5kb resolution with dom_order = 3 parameter, which identifies hierarchical TADs structures such as TADs (level 1) and sub-TADs (level 2/3), and performed aggregated TAD analysis separately according to TAD levels as described above without any additional filters to select TADs. Hi-C contact matrices were visualized by Juicebox (28) or HiCExplorer (31). Annotations on the mm9 reference genome were converted to those on mm10 and vice versa using Lift Genome Annotations (UCSC).

Splicing analysis

RNA-seq datasets in *Sf3b1* K700E mutant cells (GSE85712) and *Srsf2* P95H mutant cells (DRA006224) were previously described (32,33). We took annotation-free approach for alternative splicing analysis using JUM (34). Junctions that have more than 5 reads in 5 (for *Srsf2*) or 2 (for others) replicates of one condition were filtered for downstream analysis. According to inclusion vs exclusion criteria (shown in **Supplementary Fig. S15F**), percent spliced in (PSI) values were adjusted for each junction using a custom script. For alternative first exon (AFE), alternative last exon (ALE), and tandem UTR events, PSI values were calculated using MISO (35). Differential PSI was assessed using moderated t-test and Benjamini-Hochberg correction. For splicing events except for composite events, minimum q-value for each event was considered as a representative statistics. Events which passed a q-value threshold of 0.20 were considered as altered splicing events.

Supplementary References

1. Deardorff MA, Bando M, Nakato R, Watrin E, Itoh T, Minamino M*, et al.* HDAC8 mutations in Cornelia de Lange syndrome affect the cohesin acetylation cycle. Nature **2012**;489:313-7.
2. Faul F, Erdfelder E, Buchner A, Lang AG. Statistical power analyses using G*Power 3.1: tests for correlation and regression analyses. Behav Res Methods **2009**;41:1149-60.
3. Faul F, Erdfelder E, Lang AG, Buchner A. G*Power 3: a flexible statistical power analysis program for the social, behavioral, and biomedical sciences. Behav Res Methods **2007**;39:175-91.
4. Ema H, Morita Y, Yamazaki S, Matsubara A, Seita J, Tadokoro Y*, et al.* Adult mouse hematopoietic stem cells: purification and single-cell assays. Nat Protoc **2006**;1:2979-87.
5. Yoshida K, Sanada M, Shiraishi Y, Nowak D, Nagata Y, Yamamoto R*, et al.* Frequent pathway mutations of splicing machinery in myelodysplasia. Nature **2011**;478:64-9.
6. Dobin A, Davis CA, Schlesinger F, Drenkow J, Zaleski C, Jha S*, et al.* STAR: ultrafast universal RNA-seq aligner. Bioinformatics **2013**;29:15-21.

7. Liao Y, Smyth GK, Shi W. featureCounts: an efficient general purpose program for assigning sequence reads to genomic features. Bioinformatics **2014**;30:923-30.
8. Robinson MD, McCarthy DJ, Smyth GK. edgeR: a Bioconductor package for differential expression analysis of digital gene expression data. Bioinformatics **2010**;26:139-40.
9. Heinz S, Benner C, Spann N, Bertolino E, Lin YC, Laslo P*, et al.* Simple combinations of lineage-determining transcription factors prime cis-regulatory elements required for macrophage and B cell identities. Mol Cell **2010**;38:576-89.
10. Dougherty JD, Schmidt EF, Nakajima M, Heintz N. Analytical approaches to RNA profiling data for the identification of genes enriched in specific cells. Nucleic Acids Res **2010**;38:4218-30.
11. Choi J, Baldwin TM, Wong M, Bolden JE, Fairfax KA, Lucas EC*, et al.* Haemopedia RNA-seq: a database of gene expression during haematopoiesis in mice and humans. Nucleic Acids Res **2019**;47:D780-D5.
12. Subramanian A, Tamayo P, Mootha VK, Mukherjee S, Ebert BL, Gillette MA*, et al.* Gene set enrichment analysis: a knowledge-based approach for interpreting genome-wide expression profiles. Proc Natl Acad Sci U S A **2005**;102:15545-50.
13. Jojic V, Shay T, Sylvia K, Zuk O, Sun X, Kang J*, et al.* Identification of transcriptional regulators in the mouse immune system. Nat Immunol **2013**;14:633-43.
14. Mullenders J, Aranda-Orgilles B, Lhoumaud P, Keller M, Pae J, Wang K*, et al.* Cohesin loss alters adult hematopoietic stem cell homeostasis, leading to myeloproliferative neoplasms. J Exp Med **2015**;212:1833-50.
15. Merico D, Isserlin R, Stueker O, Emili A, Bader GD. Enrichment map: a network-based method for gene-set enrichment visualization and interpretation. PLoS One **2010**;5:e13984.
16. Ley TJ, Miller C, Ding L, Raphael BJ, Mungall AJ, Robertson A*, et al.* Genomic and epigenomic landscapes of adult de novo acute myeloid leukemia. N Engl J Med **2013**;368:2059-74.
17. Tyner JW, Tognon CE, Bottomly D, Wilmot B, Kurtz SE, Savage SL*, et al.* Functional genomic landscape of acute myeloid leukaemia. Nature **2018**;562:526-31.
18. Shiozawa Y, Malcovati L, Galli A, Pellagatti A, Karimi M, Sato-Otsubo A*, et al.* Gene expression and risk of leukemic transformation in myelodysplasia. Blood **2017**;130:2642-53.
19. Langmead B. Aligning short sequencing reads with Bowtie. Curr Protoc Bioinformatics **2010**;Chapter 11:Unit 11 7.
20. Loven J, Hoke HA, Lin CY, Lau A, Orlando DA, Vakoc CR*, et al.* Selective inhibition of tumor oncogenes by disruption of super-enhancers. Cell **2013**;153:320-34.
21. Hnisz D, Abraham BJ, Lee TI, Lau A, Saint-Andre V, Sigova AA*, et al.* Super-enhancers in the control of cell identity and disease. Cell **2013**;155:934-47.

22. Ramirez F, Dundar F, Diehl S, Gruning BA, Manke T. deepTools: a flexible platform for exploring deep-sequencing data. Nucleic Acids Res **2014**;42:W187-91.
23. Ge Y, Sealfon SC. flowPeaks: a fast unsupervised clustering for flow cytometry data via K-means and density peak finding. Bioinformatics **2012**;28:2052-8.
24. Wilson NK, Foster SD, Wang X, Knezevic K, Schutte J, Kaimakis P*, et al.* Combinatorial transcriptional control in blood stem/progenitor cells: genome-wide analysis of ten major transcriptional regulators. Cell Stem Cell **2010**;7:532-44.
25. Li Z, Zhang P, Yan A, Guo Z, Ban Y, Li J*, et al.* ASXL1 interacts with the cohesin complex to maintain chromatid separation and gene expression for normal hematopoiesis. Sci Adv **2017**;3:e1601602.
26. Aranda-Orgilles B, Saldana-Meyer R, Wang E, Trompouki E, Fassl A, Lau S*, et al.* MED12 Regulates HSC-Specific Enhancers Independently of Mediator Kinase Activity to Control Hematopoiesis. Cell Stem Cell **2016**;19:784-99.
27. Cui K, Zang C, Roh TY, Schones DE, Childs RW, Peng W*, et al.* Chromatin signatures in multipotent human hematopoietic stem cells indicate the fate of bivalent genes during differentiation. Cell Stem Cell **2009**;4:80-93.
28. Rao SS, Huntley MH, Durand NC, Stamenova EK, Bochkov ID, Robinson JT*, et al.* A 3D map of the human genome at kilobase resolution reveals principles of chromatin looping. Cell **2014**;159:1665-80.
29. Crane E, Bian Q, McCord RP, Lajoie BR, Wheeler BS, Ralston EJ*, et al.* Condensin-driven remodelling of X chromosome topology during dosage compensation. Nature **2015**;523:240-4.
30. Yu W, He B, Tan K. Identifying topologically associating domains and subdomains by Gaussian Mixture model And Proportion test. Nat Commun **2017**;8:535.
31. Ramirez F, Bhardwaj V, Arrigoni L, Lam KC, Gruning BA, Villaveces J*, et al.* High-resolution TADs reveal DNA sequences underlying genome organization in flies. Nat Commun **2018**;9:189.
32. Obeng EA, Chappell RJ, Seiler M, Chen MC, Campagna DR, Schmidt PJ*, et al.* Physiologic Expression of Sf3b1(K700E) Causes Impaired Erythropoiesis, Aberrant Splicing, and Sensitivity to Therapeutic Spliceosome Modulation. Cancer Cell **2016**;30:404-17.
33. Kon A, Yamazaki S, Nannya Y, Kataoka K, Ota Y, Nakagawa MM*, et al.* Physiological Srsf2 P95H expression causes impaired hematopoietic stem cell functions and aberrant RNA splicing in mice. Blood **2018**;131:621-35.
34. Wang Q, Rio DC. JUM is a computational method for comprehensive annotation-free analysis of alternative pre-mRNA splicing patterns. Proc Natl Acad Sci U S A **2018**;115:E8181-E90.
35. Katz Y, Wang ET, Airoldi EM, Burge CB. Analysis and design of RNA sequencing experiments for identifying isoform regulation. Nat Methods **2010**;7:1009-15.

Supplementary Figure 1 **Ochi et al.**

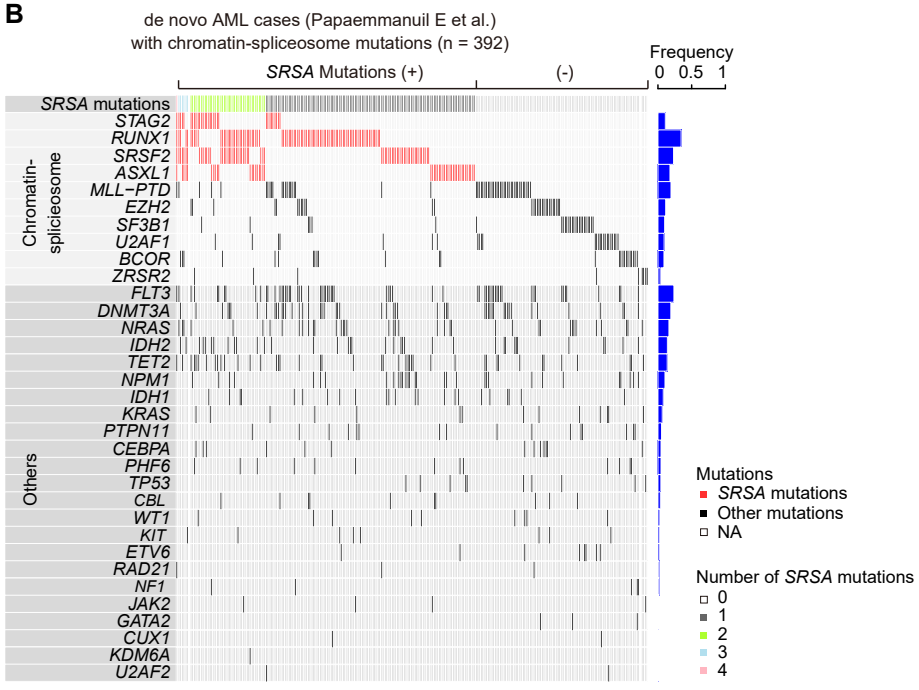

Supplementary Figure 1. Characteristics of human MDS/AML cases with '*SRSA*' mutations (*STAG2*, *RUNX1*, *SRSF2*, and/or *ASXL1*).

A, Mutational profile of MDS/AML cases with *SRSA* mutations. **B**, Mutational profile of de novo AML cases (Papaemmanuil et al., 2016) with chromatin-spliceosome mutations (*STAG2*, *RUNX1*, *SRSF2*, *ASXL1*, *EZH2*, *SF3B1*, *U2AF1*, *BCOR*, *ZRSR2* mutations, or *MLL*-partial tandem duplication (PTD)).

A

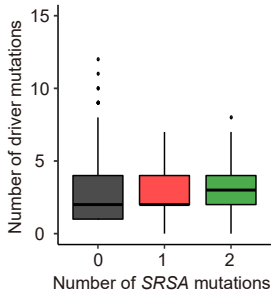
Number of driver mutations
15
10
5
0
0
1
2
Number of *SRSA* mutations

B

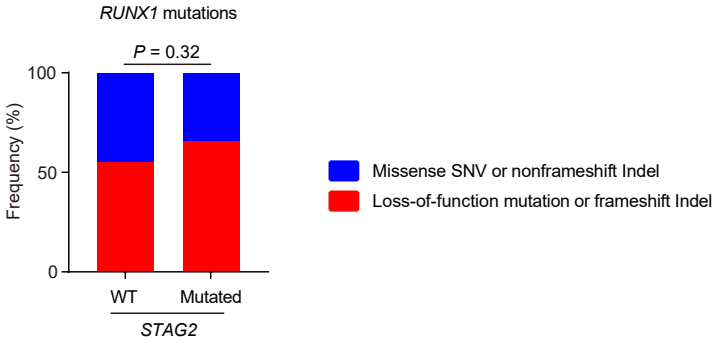
RUNX1 mutations
P = 0.32
Frequency (%)
100
50
0
WT
Mutated
STAG2
Missense SNV or nonframeshift Indel
Loss-of-function mutation or frameshift Indel

C

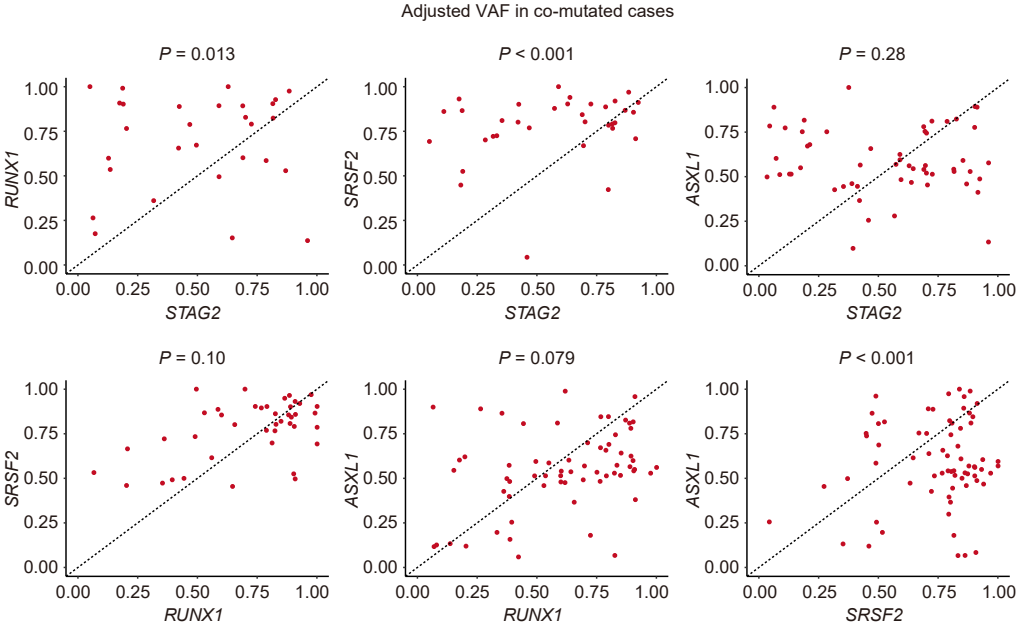
Adjusted VAF in co-mutated cases
P = 0.013
P < 0.001
P = 0.28
P = 0.10
P = 0.079
P < 0.001
RUNX1
SRSF2
ASXL1
STAG2
RUNX1
SRSF2
0.00
0.25
0.50
0.75
1.00

Supplementary Figure 2. Characteristics of *SRSA* mutations.

A, Number of driver mutations (in addition to *SRSA* mutations) according to the number of *SRSA* mutations. **B**, Proportion of loss-of-function or other *RUNX1* mutations in *STAG2*-WT or mutated cases. *P*-value was calculated by Fisher's exact test. *RUNX1* mutations have a slightly higher frequency of loss-of-function mutations (nonsense, frameshift, or splicing mutations) in *STAG2*-mutated cases than WT, although the difference was not significant ($P = 0.32$). **C**, Scatter plots of adjusted VAF values for each combination of *SRSA* mutations. *P*-values were calculated using distances to diagonal lines and Student's t-test.

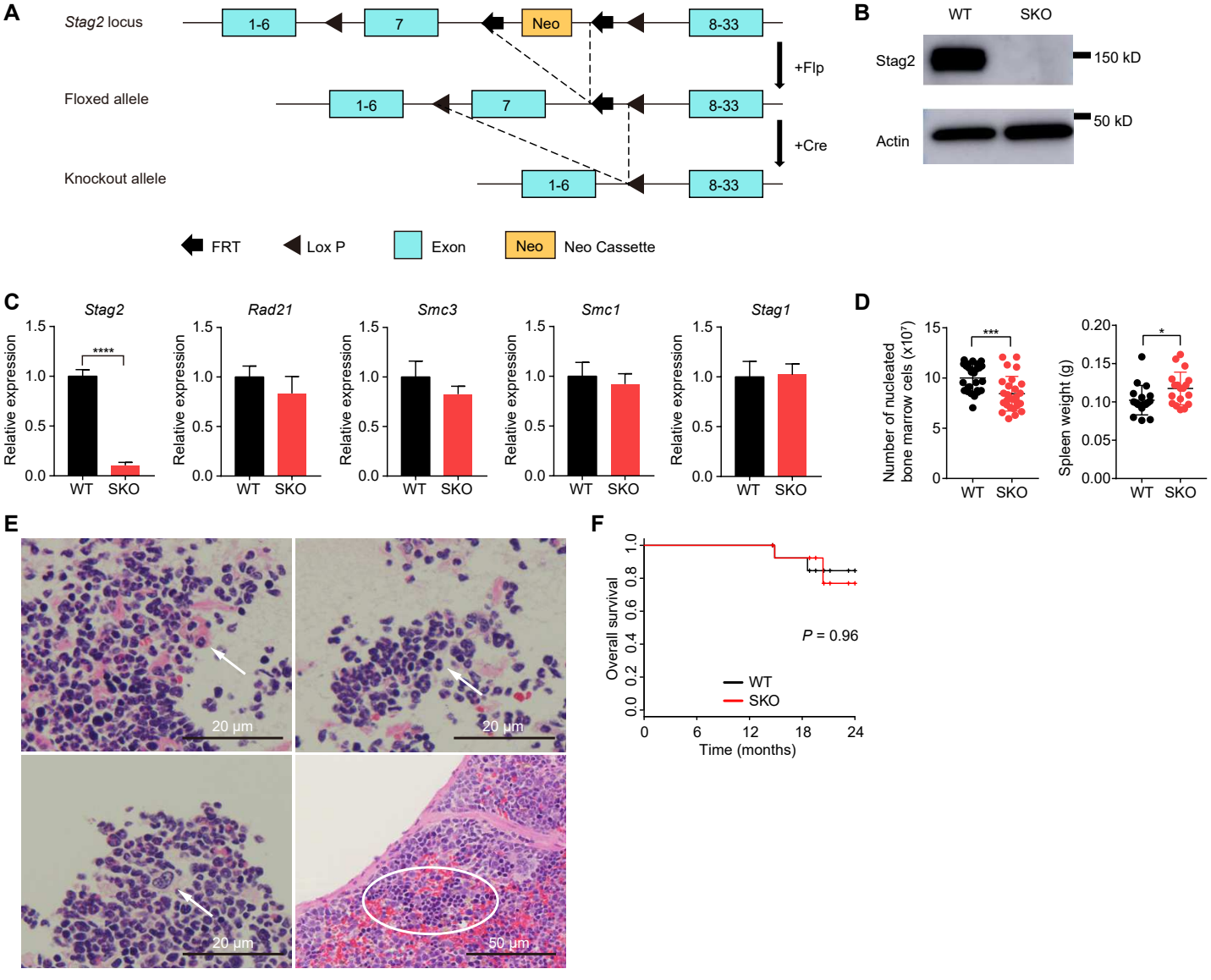
A
Stag2 locus
1-6
7
Neo
8-33
+Flp
Floxed allele
+Cre
Knockout allele
FRT
Lox P
Exon
Neo Cassette
B
WT
SKO
Stag2
150 kD
Actin
50 kD
C
Stag2
Rad21
Smc3
Smc1
Stag1
Relative expression
****
D
Number of nucleated bone marrow cels (x10^7)
***
Spleen weight (g)
*
E
20 μm
50 μm
F
Overall survival
P = 0.96
Time (months)

Supplementary Figure 3. Development of *Stag2* conditional knockout mice and examination of hematological phenotypes.

A, Schematic depiction of the targeted *Stag2* allele. FRT, flippase recognition target. **B**, Representative western blot analysis of Stag2 expression in the BM nucleated cells of WT and SKO mice. **C**, Real-Time qRT-PCR of indicated genes (relative expression, normalized by expression of 18s rRNA, mean ± SD, n = 3). **D**, Absolute number of nucleated BM cells in bilateral femurs and tibias (n = 26), and spleen weight of WT and SKO littermate male mice are plotted as dots (n = 17, mean ± SD). **E**, Section of BM and spleen stained with hematoxylin and eosin. Arrows indicate dysplastic cells in the BM and circle shows the erythroblastic islet in the spleen suggesting the extramedullary hematopoiesis. **F**, Kaplan-Meier plots for overall survival of WT and SKO mice (n = 14 per genotype). *P*-value was calculated by log-rank test. * $P < 0.05$; ** $P < 0.01$; *** $P < 0.001$; **** $P < 0.0001$. Two-tailed unpaired Student's t-test in (**C-D**).

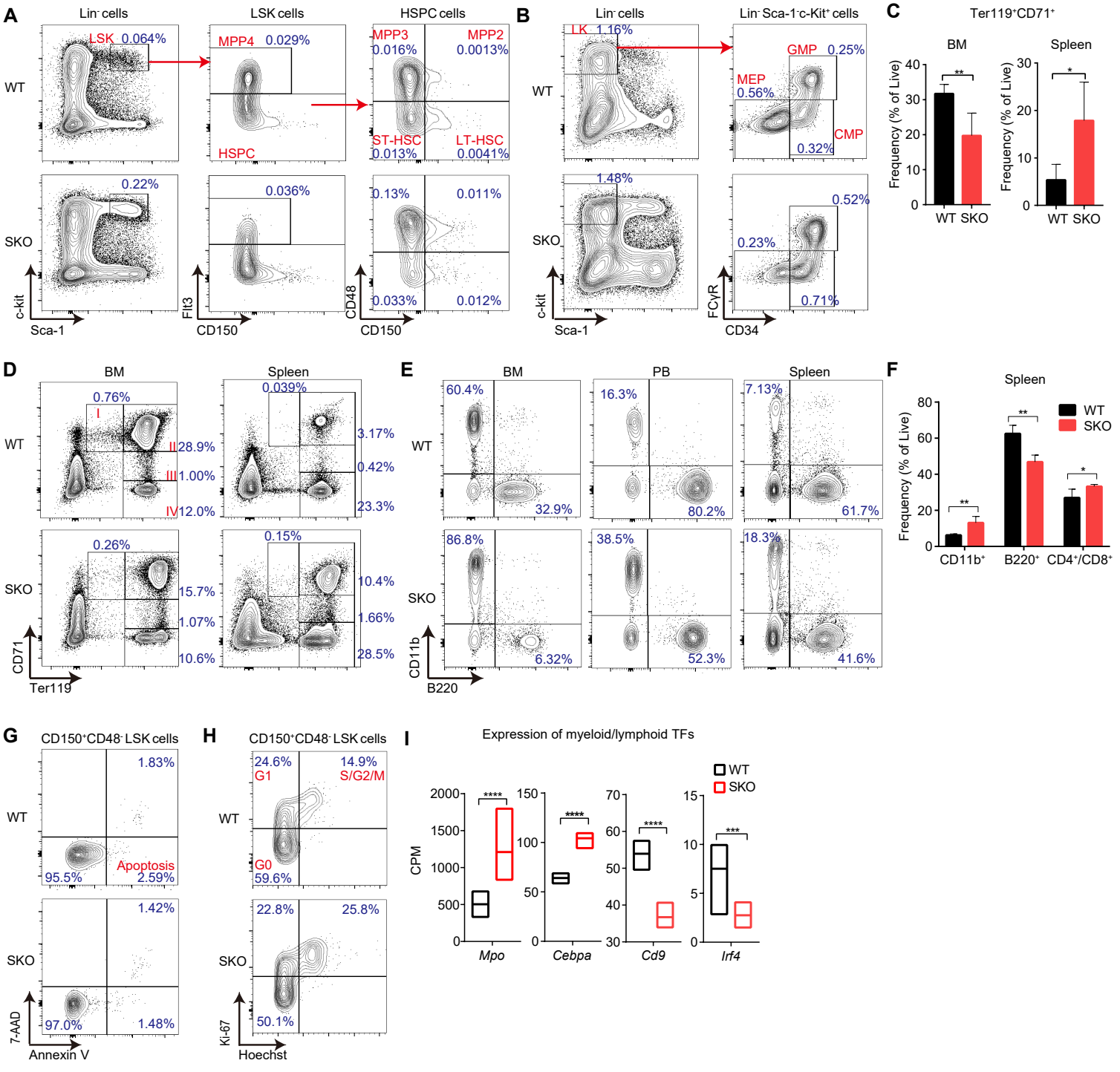
A
Lin- cells
LSK cells
HSPC cells
LSK 0.064%
MPP4 0.029%
MPP3 0.016%
MPP2 0.0013%
ST-HSC 0.013%
LT-HSC 0.0041%
HSPC
WT
SKO
0.22%
0.036%
0.13%
0.011%
0.033%
0.012%
c-kit
Sca-1
Flt3
CD150
CD48
CD150
B
Lin- cells
Lin- Sca-1- c-Kit+ cells
LK 1.16%
GMP 0.25%
MEP 0.56%
CMP 0.32%
1.48%
0.52%
0.23%
0.71%
FCγR
CD34
C
Ter119+CD71+
BM
Spleen
Frequency (% of Live)
WT SKO
D
BM
Spleen
0.76%
I
II 28.9%
III 1.00%
IV 12.0%
0.039%
3.17%
0.42%
23.3%
0.26%
15.7%
1.07%
10.6%
0.15%
10.4%
1.66%
28.5%
CD71
Ter119
E
BM
PB
Spleen
60.4%
32.9%
16.3%
80.2%
7.13%
61.7%
86.8%
6.32%
38.5%
52.3%
18.3%
41.6%
CD11b
B220
F
Spleen
WT
SKO
Frequency (% of Live)
CD11b+
B220+
CD4+/CD8+
G
CD150+CD48- LSK cells
1.83%
95.5%
Apoptosis
2.59%
1.42%
97.0%
1.48%
7-AAD
Annexin V
H
CD150+CD48- LSK cells
24.6%
G1
14.9%
S/G2/M
G0
59.6%
22.8%
25.8%
50.1%
Ki-67
Hoechst
I
Expression of myeloid/lymphoid TFs
WT
SKO
CPM
Mpo
Cebpa
Cd9
Irf4

Supplementary Figure 4. Flow cytometry and transcriptome analysis of *Stag2* conditional knockout mice.

A-B, Representative flow cytometry analysis of the BM LSK (**A**) and Lin-negative/Sca1$^-$/c-Kit$^+$ (LK) populations (**B**) of WT and SKO mice. **C**, Frequency of erythroblasts (Ter119$^+$CD71$^+$) in the BM and spleen (n =5, mean ± SD). **D-E**, Representative flow cytometry analysis of erythroid maturation in the BM and spleen (**D**) and lineage-committed cells in the BM, PB and spleen (**E**). **F**, Frequency of lineage-committed cells in the spleen (n = 4, mean ± SD). **G-H**, Representative flow cytometry analysis of apoptosis (**G**) and cell-cycle (**H**). **I**, Expression levels of myeloid/lymphoid TFs in LSK cells indicated by CPM (min to max values with mean, n = 3). *P*-values were calculated using edgeR package. * $P < 0.05$; ** $P < 0.01$; *** $P < 0.001$; **** $P < 0.0001$. Two-tailed unpaired Student's t-test in (**C, F**).

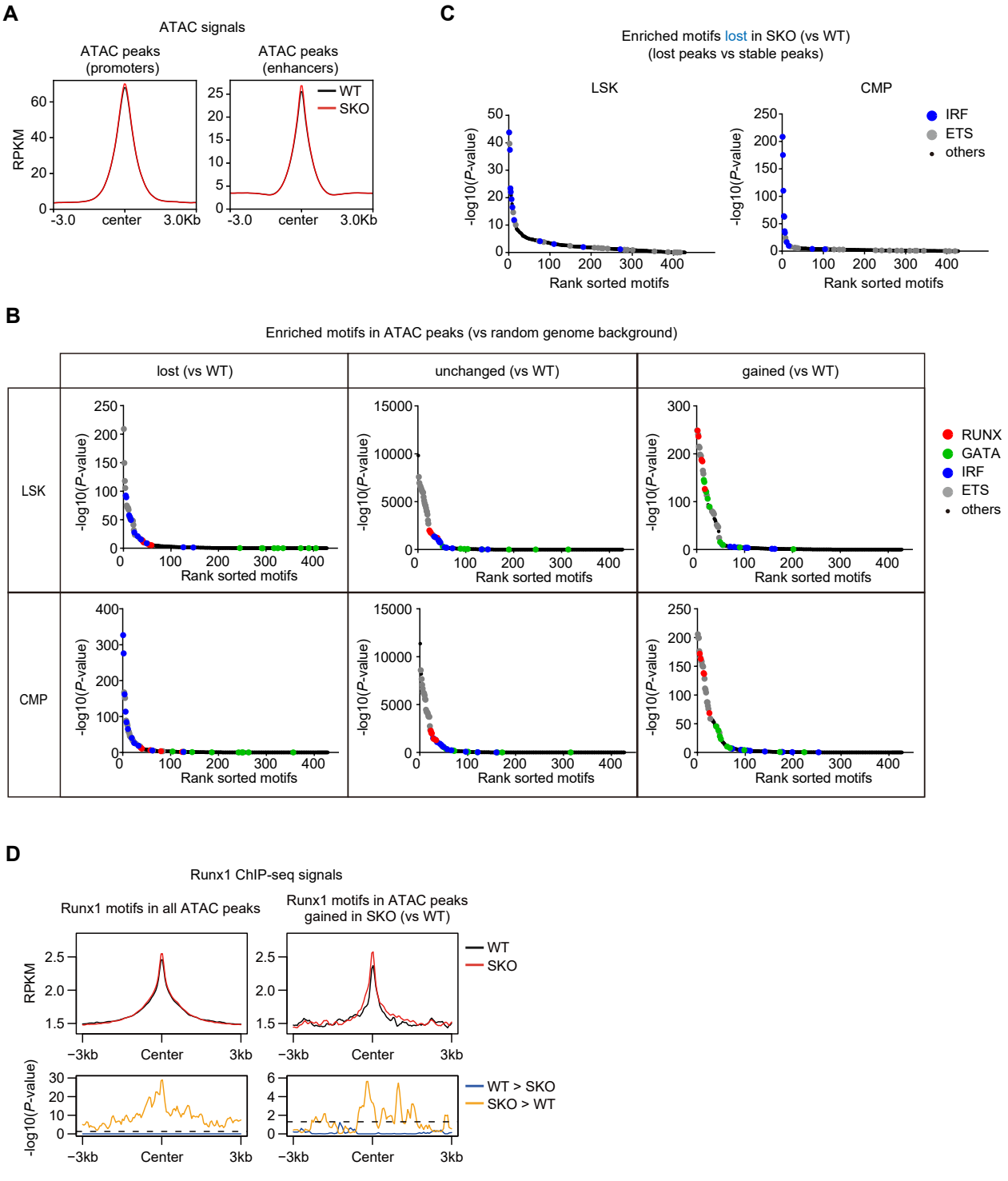
A
ATAC signals
ATAC peaks (promoters)
ATAC peaks (enhancers)
RPKM
WT
SKO
-3.0
center
3.0Kb
C
Enriched motifs lost in SKO (vs WT)
(lost peaks vs stable peaks)
LSK
CMP
-log10(P-value)
Rank sorted motifs
IRF
ETS
others
B
Enriched motifs in ATAC peaks (vs random genome background)
lost (vs WT)
unchanged (vs WT)
gained (vs WT)
LSK
CMP
RUNX
GATA
IRF
ETS
others
D
Runx1 ChIP-seq signals
Runx1 motifs in all ATAC peaks
Runx1 motifs in ATAC peaks gained in SKO (vs WT)
WT
SKO
WT > SKO
SKO > WT
-3kb
Center
3kb

Supplementary Figure 5. Epigenome analysis of *Stag2* conditional knockout mice.

A, Average signal intensities of ATAC-seq around the ATAC-peaks in promoters (left) or enhancers (right) in WT- and SKO-derived LSK cells. **B**, Enrichment of known TF motifs in the ATAC-seq peaks with gained, lost, or unchanged accessibility in SKO-derived LSK or CMP cells compared with WT cells. The sorted motif rank and –log10(*P*-value) of a motif enrichment test using random genome backgrounds are indicated in horizontal and vertical axis, respectively. **C**, Enrichment of known transcription factor motifs in the ATAC-seq peaks that lost accessibility in SKO-derived LSK (left panel) and CMP cells (right panel) compared with WT. Stable peaks are used as backgrounds. **D**, Average Runx1 ChIP-seq signals of WT- and SKO-derived c-Kit$^+$ HSPCs around Runx1 motifs in all ATAC peaks (left panel), or in gained ATAC peaks in SKO-derived LSK cells compared with WT (right panel). *P*-values were calculated by one-sided Wilcoxon rank-sum test comparing the ChIP-intensities in each bin. Horizontal dashed lines indicate $P = 0.05$.

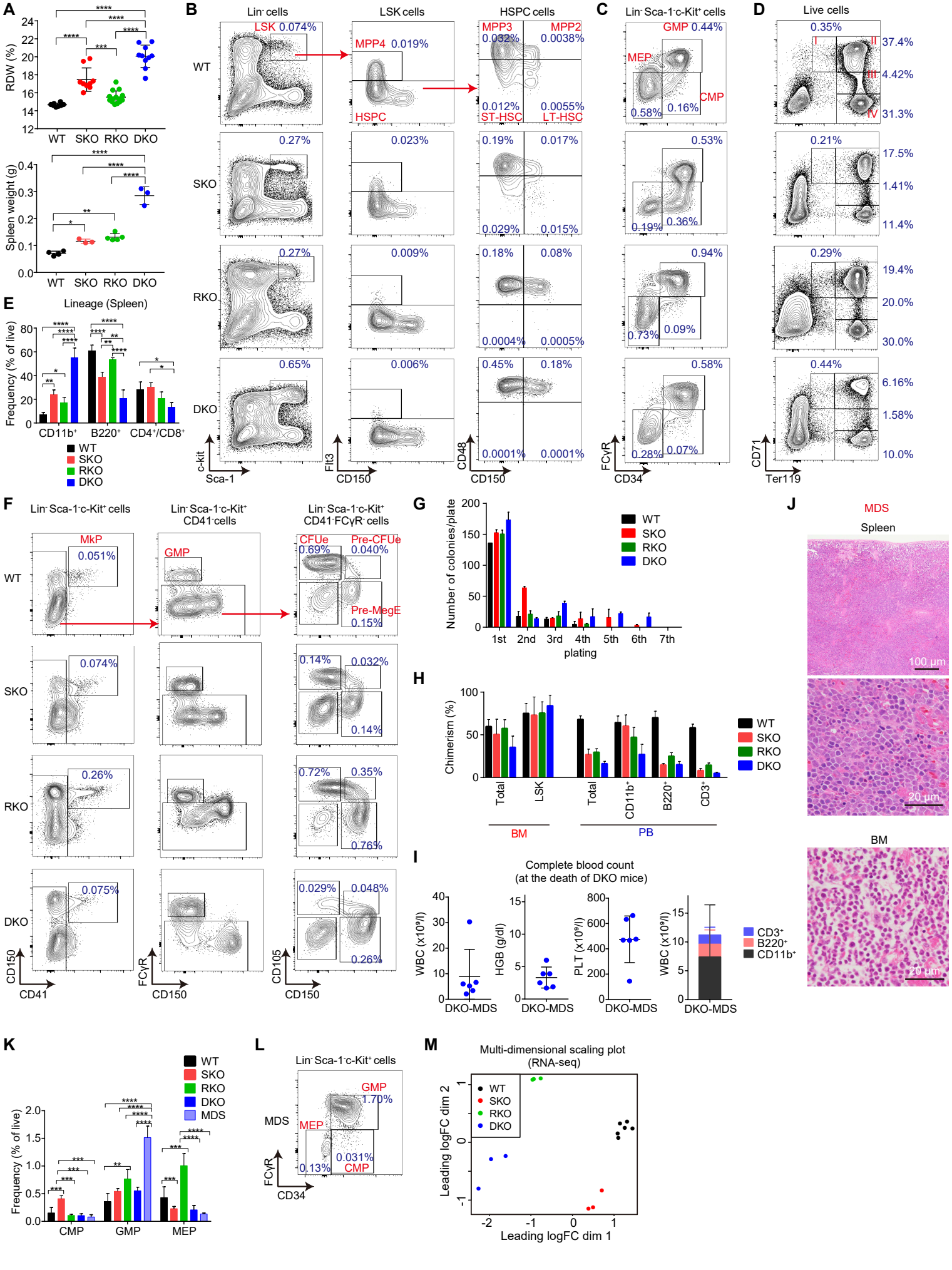
A
RDW (%)
WT SKO RKO DKO
Spleen weight (g)
WT SKO RKO DKO
B
Lin- cells
LSK cells
HSPC cells
WT
SKO
RKO
DKO
LSK 0.074%
MPP4 0.019%
HSPC
MPP3 0.032%
MPP2 0.0038%
0.012% ST-HSC
0.0055% LT-HSC
0.27%
0.023%
0.19% 0.017%
0.029% 0.015%
0.27%
0.009%
0.18% 0.08%
0.0004% 0.0005%
0.65%
0.006%
0.45% 0.18%
0.0001% 0.0001%
c-kit
Sca-1
Flt3
CD150
CD48
CD150
C
Lin- Sca-1- c-Kit+ cells
GMP 0.44%
MEP
CMP
0.58% 0.16%
0.53%
0.19% 0.36%
0.94%
0.73% 0.09%
0.58%
0.28% 0.07%
FCγR
CD34
D
Live cells
0.35%
I
II
III
IV
37.4%
4.42%
31.3%
0.21%
17.5%
1.41%
11.4%
0.29%
19.4%
20.0%
30.0%
0.44%
6.16%
1.58%
10.0%
CD71
Ter119
E
Lineage (Spleen)
Frequency (% of live)
CD11b+ B220+ CD4+/CD8+
WT
SKO
RKO
DKO
F
Lin- Sca-1- c-Kit+ cells
Lin- Sca-1- c-Kit+ CD41- cells
Lin- Sca-1- c-Kit+ CD41- FCγR- cells
MkP 0.051%
GMP
CFUe 0.69%
Pre-CFUe 0.040%
Pre-MegE 0.15%
0.074%
0.14%
0.032%
0.14%
0.26%
0.72%
0.35%
0.76%
0.075%
0.029%
0.048%
0.26%
CD150
CD41
FCγR
CD150
CD105
CD150
G
Number of colonies/plate
1st 2nd 3rd 4th 5th 6th 7th
plating
WT
SKO
RKO
DKO
H
Chimerism (%)
Total LSK Total CD11b+ B220+ CD3+
BM
PB
WT
SKO
RKO
DKO
I
Complete blood count
(at the death of DKO mice)
WBC (x10⁹/l)
HGB (g/dl)
PLT (x10⁹/l)
WBC (x10⁹/l)
DKO-MDS
CD3+
B220+
CD11b+
J
MDS
Spleen
100 μm
20 μm
BM
20 μm
K
Frequency (% of live)
CMP GMP MEP
WT
SKO
RKO
DKO
MDS
L
Lin- Sca-1- c-Kit+ cells
MDS
GMP 1.70%
MEP
0.031%
0.13%
CMP
FCγR
CD34
M
Multi-dimensional scaling plot
(RNA-seq)
Leading logFC dim 2
Leading logFC dim 1
WT
SKO
RKO
DKO

Supplementary Figure 6. Phenotypes of *Stag2*/*Runx1* conditional knockout mice.

A, RDW and spleen weight are plotted as dots (n = 8 for WT, 9 for SKO, 14 for RKO, and 10 for DKO in RDW and n = 5 for WT and RKO, and 3 for SKO and DKO in spleen weight, mean ± SD). **B-D**, Representative flow cytometry analysis of BM LSK cells (**B**), Lin-negative/Sca1$^-$/c-Kit$^+$ cells (**C**), and erythroid precursors (**D**). **E**, Frequency of each lineage-committed cells in the spleen (n = 5 for WT and RKO, and 3 for SKO and DKO, mean ± SD). **F**, Representative flow cytometry analysis of the megakaryocytic and erythroid progenitors in the BM. **G**, Colony counts in methylcellulose replating experiments (mean ± SD, n = 2) of BM cells. **H**, Percentages of CD45.2$^+$ donor cells within each fraction of BM or PB after competitive BM transplantation (16 weeks after pIpC injection) are shown (n = 4, mean ± SD). **I**, WBC, HGB, PLT counts, and total cell number of granulocytes/monocytes (CD11b$^+$), B lymphoid (B220$^+$) and T lymphoid (CD4$^+$/CD8$^+$) cells in the PB of mice that developed MDS (n = 6, mean ± SD). **J**, Section of the spleen (upper panels) and BM (lower panel) stained with hematoxylin and eosin, showing the infiltrating dysplastic myeloid cells in the spleen and BM. **K**, Frequencies of myeloid progenitors in the BM of WT, SKO, RKO or DKO-transplanted mice and MDS mice (DKO mice that developed MDS) (n = 5 for WT and RKO, and 3 for SKO, DKO and MDS, mean ± SD). **L**, Representative flow cytometry analysis of the myeloid progenitors in the BM of DKO mice that developed MDS, showing the expansion of the GMP fractions. **M**, Multi-dimensional scaling plot in which distances correspond to leading logFC between each pair of RNA-seq sample in WT/SKO/RKO/DKO-derived LSK cells. The leading logFC is the average of the largest absolute logFC between each pair of samples. The horizontal and vertical axis show the leading logFC of dimension 1 and 2, respectively. * $P < 0.05$; ** $P < 0.01$; *** $P < 0.001$; **** $P < 0.0001$. *P*-values were calculated by ordinary one-way ANOVA with Bonferroni analysis in (**A, E, K**).

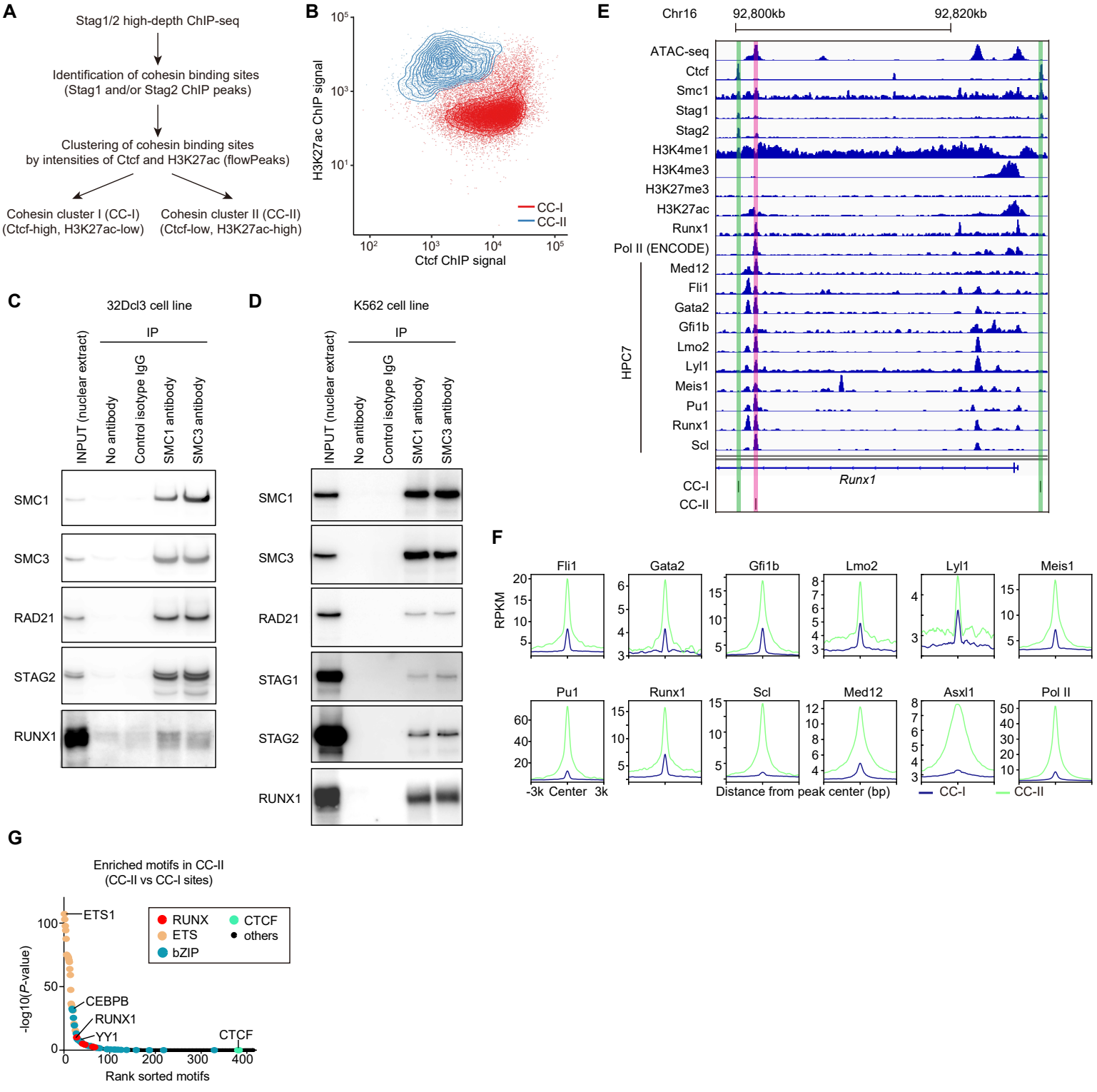
A
Stag1/2 high-depth ChIP-seq
Identification of cohesin binding sites
(Stag1 and/or Stag2 ChIP peaks)
Clustering of cohesin binding sites
by intensities of Ctcf and H3K27ac (flowPeaks)
Cohesin cluster I (CC-I)
(Ctcf-high, H3K27ac-low)
Cohesin cluster II (CC-II)
(Ctcf-low, H3K27ac-high)
B
H3K27ac ChIP signal
Ctcf ChIP signal
CC-I
CC-II
C
32Dcl3 cell line
INPUT (nuclear extract)
IP
No antibody
Control isotype IgG
SMC1 antibody
SMC3 antibody
SMC1
SMC3
RAD21
STAG2
RUNX1
D
K562 cell line
STAG1
E
Chr16
92,800kb
92,820kb
ATAC-seq
Ctcf
Smc1
Stag1
Stag2
H3K4me1
H3K4me3
H3K27me3
H3K27ac
Runx1
Pol II (ENCODE)
HPC7
Med12
Fli1
Gata2
Gfi1b
Lmo2
Lyl1
Meis1
Pu1
Runx1
Scl
Runx1
CC-I
CC-II
F
Fli1
Gata2
Gfi1b
Lmo2
Lyl1
Meis1
RPKM
Pu1
Runx1
Scl
Med12
Asxl1
Pol II
-3k Center 3k
Distance from peak center (bp)
CC-I
CC-II
G
Enriched motifs in CC-II
(CC-II vs CC-I sites)
RUNX
ETS
bZIP
CTCF
others
ETS1
CEBPB
RUNX1
YY1
CTCF
-log10(P-value)
Rank sorted motifs

Supplementary Figure 7. ChIP-seq analysis and identification of CC-I and CC-II sites.

A, Summary of the methods used to identify the two types of cohesin binding sites in ChIP-seq analysis. **B**, Scatterplot and density plot of Ctcf and H3K27ac ChIP intensities for each cohesin binding site, indicated as RPKM values summed up around ± 200 bp from the center of each peak, according to the clusters of cohesin binding sites. CC-I, cohesin-cluster I; CC-II, cohesin-cluster II. **C-D**, Co-immunoprecipitation and western blotting experiments showing the physical interactions of cohesin complex with Runx1/RUNX1 in mouse 32Dcl3 (**C**) or human K562 (**D**) leukemia cell lines. Nuclear extractions were subjected to immunoprecipitation using indicated antibodies above the photos, followed by western blotting using antibodies indicated on the left. **E**, Genome browser snapshot demonstrating the co-localization of various transcriptional regulators at CC-II site at *Runx1* gene locus. **F**, Distribution of indicated proteins around cohesin binding sites were analyzed using published ChIP-seq data of HPC7 and others (Aranda-Orgilles et al., 2016; Li et al., 2017; Wilson et al., 2010), and average ChIP-seq read intensities around CC-I (blue) and CC-II (green) sites are depicted. **G**, Enrichment of known transcription factor motifs in the ChIP-seq peaks of CC-II sites compared with CC-I sites. The sorted motif rank and –log10(*P*-value) of a motif enrichment test are indicated in horizontal and vertical axis, respectively.

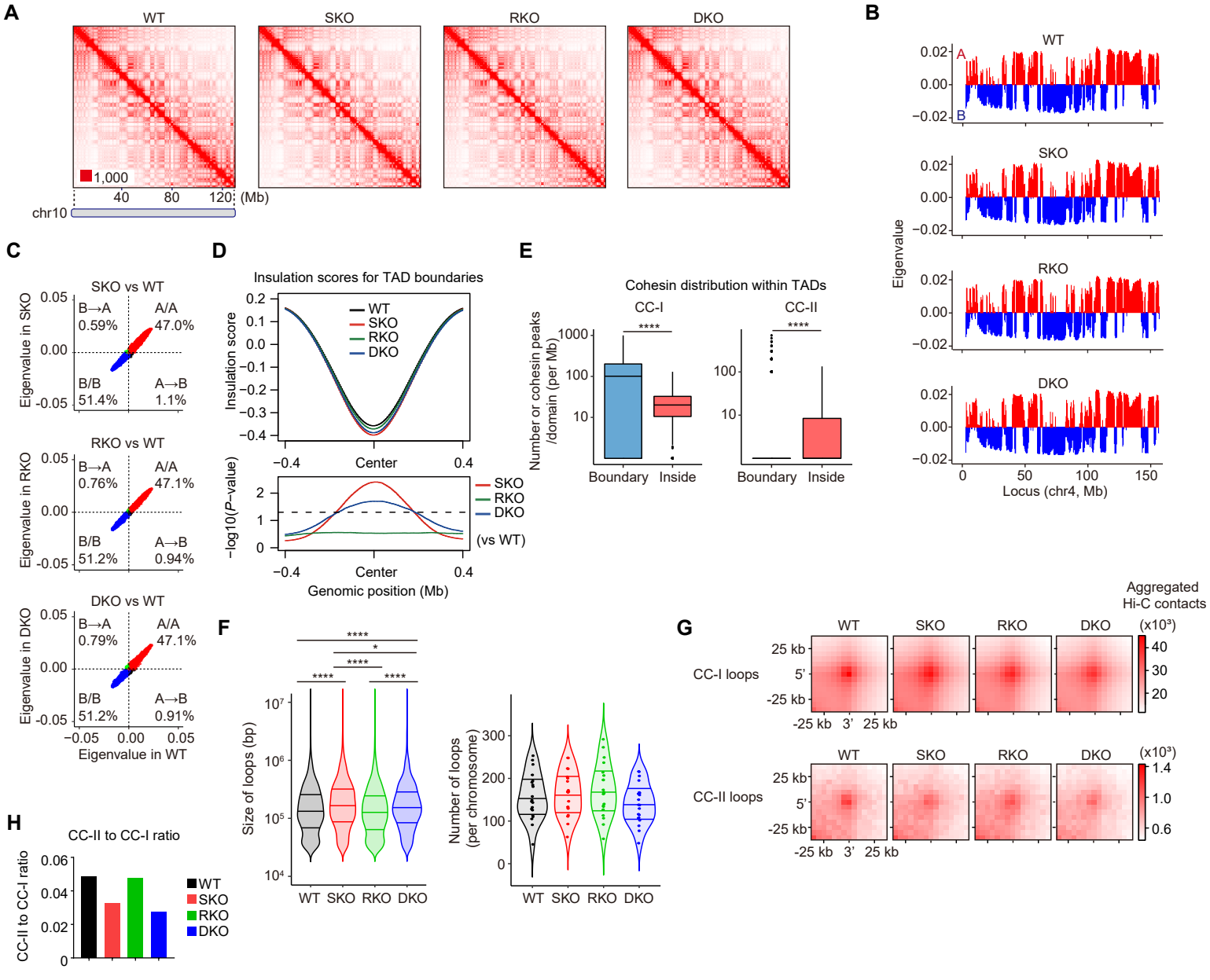
A
WT
SKO
RKO
DKO
1,000
40
80
120
(Mb)
chr10
B
WT
SKO
RKO
DKO
A
B
0.02
0.00
−0.02
Eigenvalue
0
50
100
150
Locus (chr4, Mb)
C
SKO vs WT
RKO vs WT
DKO vs WT
B→A
A/A
B/B
A→B
0.59%
47.0%
51.4%
1.1%
0.76%
47.1%
51.2%
0.94%
0.79%
47.1%
51.2%
0.91%
Eigenvalue in SKO
Eigenvalue in RKO
Eigenvalue in DKO
Eigenvalue in WT
0.05
0.00
−0.05
D
Insulation scores for TAD boundaries
Insulation score
−log10(P−value)
WT
SKO
RKO
DKO
(vs WT)
−0.4
Center
0.4
Genomic position (Mb)
E
Cohesin distribution within TADs
CC-I
CC-II
****
Number or cohesin peaks /domain (per Mb)
1000
100
10
Boundary
Inside
F
****
*
Size of loops (bp)
Number of loops (per chromosome)
WT SKO RKO DKO
G
Aggregated Hi-C contacts
CC-I loops
CC-II loops
25 kb
5'
-25 kb
3'
(x10³)
40
30
20
1.4
1.0
0.6
H
CC-II to CC-I ratio
0.06
0.04
0.02
0

Supplementary Figure 8. Hi-C analysis in *Stag2*/*Runx1* conditional knockout mice.

A, Knight-Ruiz (KR)-normalized Hi-C contact matrices in whole chromosome 10, generated by Juicebox. The intensity of each pixel represents the normalized number of contacts between a pair of loci, and maximum intensity of Hi-C contact is indicated in the lower left of the panel. **B**, First eigenvalues for each genotype at each genomic bin in chromosome 4 indicated as snapshot showing the genomic locus and corresponding values. A-compartments were assigned to the genomic bin with positive eigenvector values as well as higher gene density and B-compartments were the opposite. **C**, Scatterplot of the first eigenvalues for SKO, RKO, or DKO vs WT. Numbers within the plots indicate the percentage of bins, in which assignments to A- or B-compartments were changed or unchanged in SKO, RKO, or DKO compared with WT. Colors of dots represent the changed (green, B to A; black, A to B) or unchanged (red, A to A; blue, B to B) bins. **D**, Average insulation scores at the center of all TAD boundaries. Distance from the boundary and average insulation scores are indicated in horizontal and vertical axis, respectively. *P*-values were calculated by bin-wise one-sided Wilcoxon rank-sum test. **E** Number of cohesin peaks (CC-I or CC-II) insides or at the boundaries of TADs. *P*-values were calculated by two-sided Wilcoxon rank-sum test. A horizontal dashed line indicates $P = 0.05$. **F**, Violin plots showing the size distribution (left) and numbers of all loops (right). *P*-values were calculated by pairwise comparisons using two-sided Wilcoxon rank-sum test with Bonferroni correction. **G**, Aggregate peak analysis (Rao et al., 2014) to measure the aggregate strength of loops anchored at CC-I or CC-II loops, showing the diminishment of CC-II loops particularly in DKO. The number of aggregated Hi-C contacts for each type of loops is indicated in the color bars. **H**, Ratio of CC-II loops to CC1 loops in each genotype. * $P < 0.05$; ** $P < 0.01$; *** $P < 0.001$; **** $P < 0.0001$.

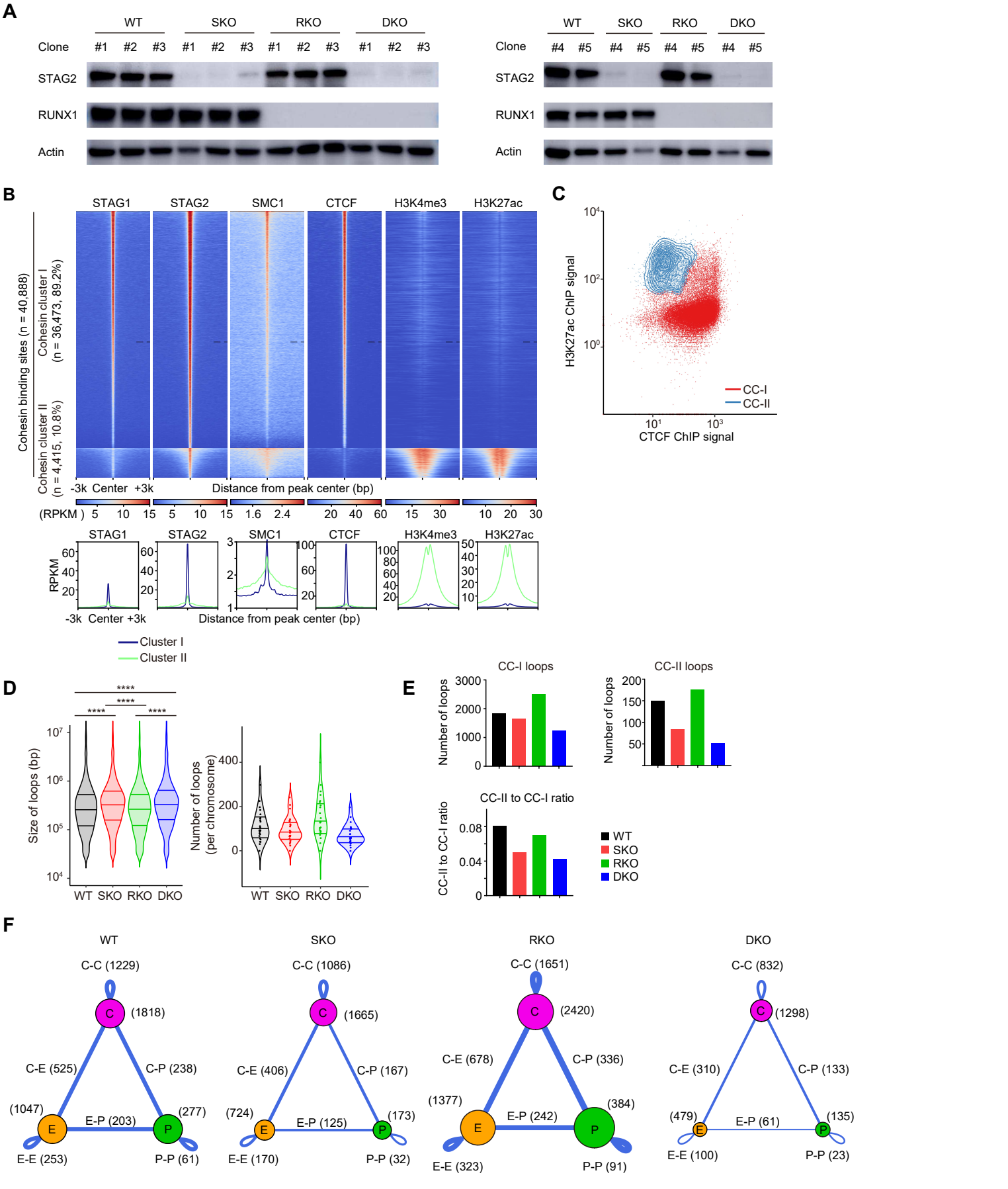
A
WT
SKO
RKO
DKO
Clone
#1 #2 #3 #1 #2 #3 #1 #2 #3 #1 #2 #3
STAG2
RUNX1
Actin
#4 #5 #4 #5 #4 #5 #4 #5
B
STAG1 STAG2 SMC1 CTCF H3K4me3 H3K27ac
Cohesin binding sites (n = 40,888)
Cohesin cluster I (n = 36,473, 89.2%)
Cohesin cluster II (n = 4,415, 10.8%)
-3k Center +3k
Distance from peak center (bp)
(RPKM)
RPKM
Cluster I
Cluster II
C
H3K27ac ChIP signal
CTCF ChIP signal
CC-I
CC-II
D
Size of loops (bp)
Number of loops (per chromosome)
WT SKO RKO DKO
E
CC-I loops
CC-II loops
Number of loops
CC-II to CC-I ratio
F
WT
SKO
RKO
DKO
C-C (1229)
C-C (1086)
C-C (1651)
C-C (832)
(1818)
(1665)
(2420)
(1298)
C-E (525)
C-P (238)
C-E (406)
C-P (167)
C-E (678)
C-P (336)
C-E (310)
C-P (133)
(1047)
(277)
(724)
(173)
(1377)
(384)
(479)
(135)
E-P (203)
E-P (125)
E-P (242)
E-P (61)
E-E (253)
P-P (61)
E-E (170)
P-P (32)
E-E (323)
P-P (91)
E-E (100)
P-P (23)

Supplementary Figure 9. Hi-C analysis of *STAG2*/*RUNX1* knockout HL-60 human leukemia cell lines. **A**, Representative western blots of STAG2 and RUNX1 expression in HL-60 cell lines with *STAG2*/*RUNX1* KO. **B**, Upper panels: ChIP-seq density heatmap in parent (WT) HL-60 cell lines centered on STAG1- and/or STAG2-cohesin binding sites, in which cohesin binding sites were divided into CC-I and CC-II according to the ChIP signals for CTCF and H3K27ac (see also panel (**C**) and **Supplementary Fig. S7A**). Lower panels: Average ChIP-seq read intensity plot for CC-I (blue) and CC-II (green) distribution around the cohesin binding sites. **C**, Scatter plot and density plot of CTCF and H3K27ac ChIP intensities for each cohesin binding site, indicated as RPKM values summed up around ± 200 bp from the center of each peak, according to the clusters of cohesin binding sites in HL-60 cell lines. **D**, Violin plots showing the size distribution (left) and numbers of all loops (right). *P*-values were calculated by pairwise comparisons using two-sided Wilcoxon rank-sum test with Bonferroni correction. **E**, Number of CC-I or CC-II loops and ratio of number of CC-II loops to CC-I loops. **F**, Summary of major types of loops identified in each genotype of HL-60 cell lines. CTCF sites (CC-I sites) and active enhancers/promoters in which loops were anchored are displayed as purple, orange, and green circles, respectively. The loops between two sites are displayed as blue lines, and the width of the lines is proportional to the number of loops relative to WT. E, Enhancer; P, Promoter; C, CTCF; C-C, CTCF-CTCF; C-E, CTCF-Enhancer: C-P, CTCF-Promoter; E-E, Enhancer-Enhancer; E-P, Enhancer-Promoter; P-P, Promoter-Promoter. * $P < 0.05$; ** $P < 0.01$; *** $P < 0.001$; **** $P < 0.0001$.

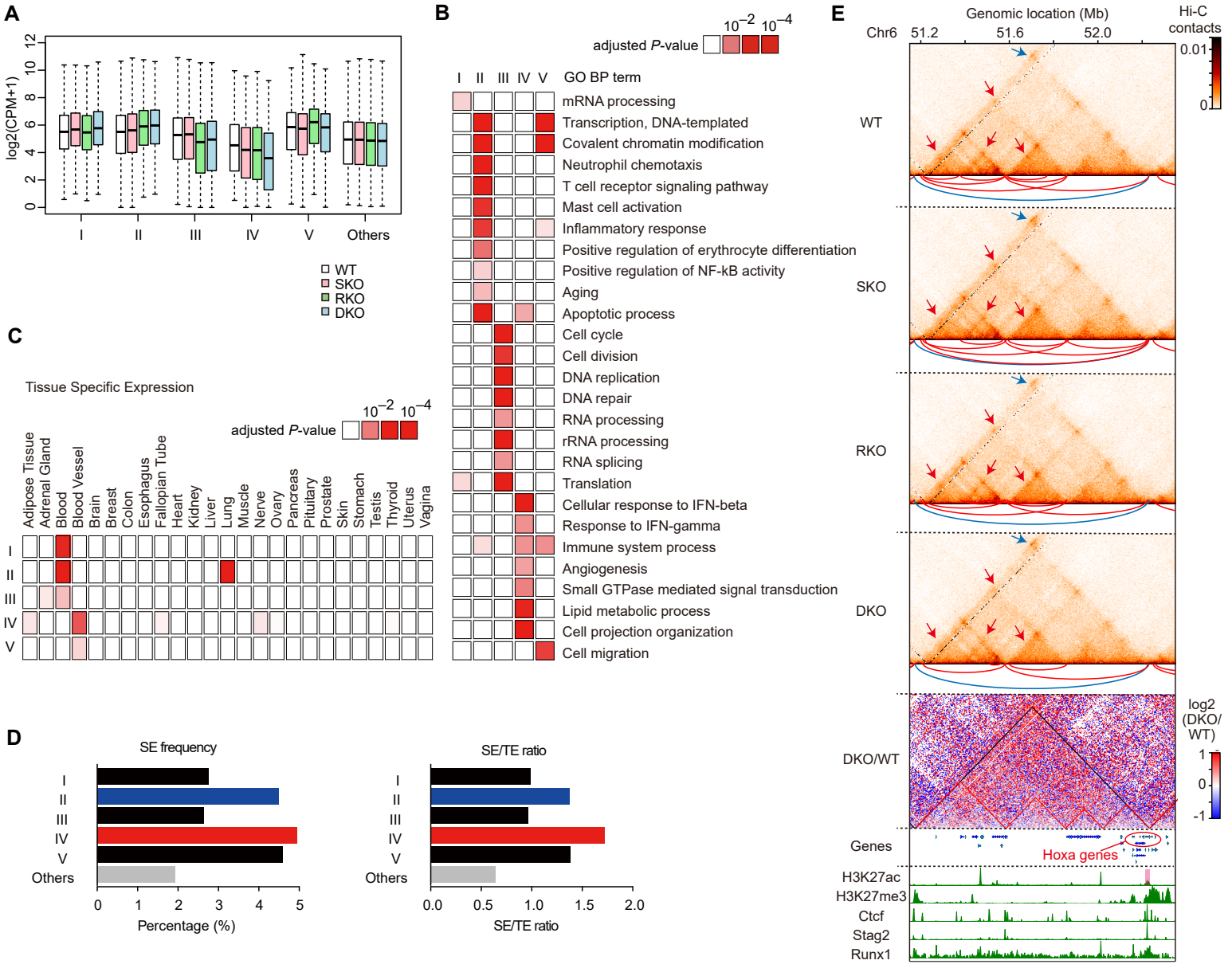
A
log2(CPM+1)
I
II
III
IV
V
Others
WT
SKO
RKO
DKO
B
adjusted P-value
GO BP term
mRNA processing
Transcription, DNA-templated
Covalent chromatin modification
Neutrophil chemotaxis
T cell receptor signaling pathway
Mast cell activation
Inflammatory response
Positive regulation of erythrocyte differentiation
Positive regulation of NF-kB activity
Aging
Apoptotic process
Cell cycle
Cell division
DNA replication
DNA repair
RNA processing
rRNA processing
RNA splicing
Translation
Cellular response to IFN-beta
Response to IFN-gamma
Immune system process
Angiogenesis
Small GTPase mediated signal transduction
Lipid metabolic process
Cell projection organization
Cell migration
C
Tissue Specific Expression
adjusted P-value
Adipose Tissue
Adrenal Gland
Blood
Blood Vessel
Brain
Breast
Colon
Esophagus
Fallopian Tube
Heart
Kidney
Liver
Lung
Muscle
Nerve
Ovary
Pancreas
Pituitary
Prostate
Skin
Stomach
Testis
Thyroid
Uterus
Vagina
D
SE frequency
Percentage (%)
SE/TE ratio
E
Genomic location (Mb)
Chr6
Hi-C contacts
WT
SKO
RKO
DKO
DKO/WT
log2 (DKO/WT)
Genes
Hoxa genes
H3K27ac
H3K27me3
Ctcf
Stag2
Runx1

Supplementary Figure 10. Analysis of transcriptomes, super-enhancers, and Hi-C datasets in Stag2/Runx1 deficient HSPCs.

A, Box plots showing expression levels of each DEG group in WT/SKO/RKO/DKO-derived LSK cells. The vertical axis represents the log2(CPM+1) in the indicated genotype and DEG group. **B**, Summary of representative gene ontology (GO) terms associated with the indicated DEG groups with corresponding adjusted *P*-values, determined by DAVID. **C**, Summary of enrichment of genes of the indicated DEG groups in tissue-specific gene sets in various tissues, determined by Tissue Specific Expression Analysis (TSEA). Adjusted *P*-values are displayed as heatmap. **D**, Frequency of SE-associated gene (upper) and ratio of frequency of SE-associated genes to that of TE-associated genes in each DEG group (bottom). **E**, Genome browser snapshot demonstrating the Hi-C contacts, chromatin loops, and ChIP-seq profiles at the Hoxa gene cluster including *Hoxa9* gene. The black and red triangles in the DKO/WT Hi-C contact map shows the primary TAD and sub-TADs called in WT, respectively. The arcs below each Hi-C contact map show the loops identified in corresponding Hi-C data. Note that smaller loops (red arrows) and Hi-C contacts within sub-TADs (red triangle) were weakened in DKO, while a larger Ctcf-mediated loop (blue arrow) was rather enhanced.

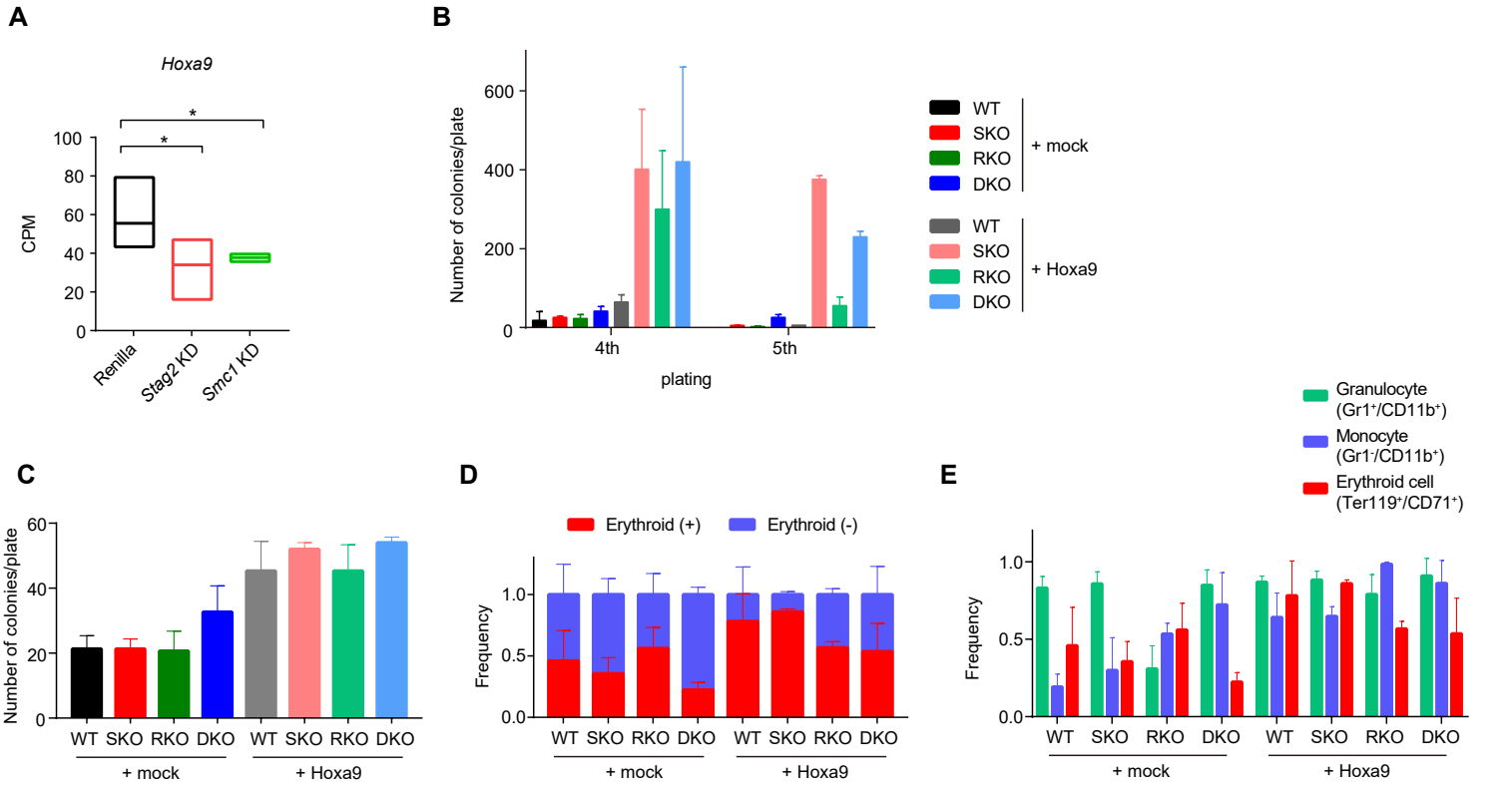
A
Hoxa9
CPM
100
80
60
40
20
0
*
*
Renilla
Stag2 KD
Smc1 KD
B
Number of colonies/plate
600
400
200
0
4th
5th
plating
WT
SKO
RKO
DKO
+ mock
WT
SKO
RKO
DKO
+ Hoxa9
C
Number of colonies/plate
60
40
20
0
WT SKO RKO DKO WT SKO RKO DKO
+ mock
+ Hoxa9
D
Erythroid (+)
Erythroid (-)
Frequency
1.0
0.5
0.0
WT SKO RKO DKO WT SKO RKO DKO
+ mock
+ Hoxa9
E
Granulocyte (Gr1+/CD11b+)
Monocyte (Gr1-/CD11b+)
Erythroid cell (Ter119+/CD71+)
Frequency
1.0
0.5
0.0
WT SKO RKO DKO WT SKO RKO DKO
+ mock
+ Hoxa9

Supplementary Figure 11. Effects of Hoxa9 overexpression on Stag2/Runx1 deficient HSPCs.

A, Expression levels of *Hoxa9* in *Stag2* or *Smc1* knockdown (KD) LSK cells (Mullenders et al., 2015), indicated by CPM (min to max values with mean, n = 4 for Renilla and 3 for KD groups). *P*-values were calculated using edgeR package in R software. **B**, Colony counts at 4th and 5th plating in methylcellulose replating experiments (mean ± SD, n = 2) of c-Kit$^+$ cells transduced with mock- or Hoxa9-expressing retroviral vector. Transduced cells were selected by G418 at the first plating. **C**, Colony counts per 96-well plate in single-cell liquid culture assay (mean ± SD, n = 3) of c-Kit$^+$ cells transduced with mock- or Hoxa9-expressing retroviral vector. **D**, Frequencies of colonies containing or not containing erythroid cells (mean ± SD, n = 3). **E**, Frequencies of granulocyte-, monocyte-, and erythroid-containing colonies (mean ± SD, n = 3).

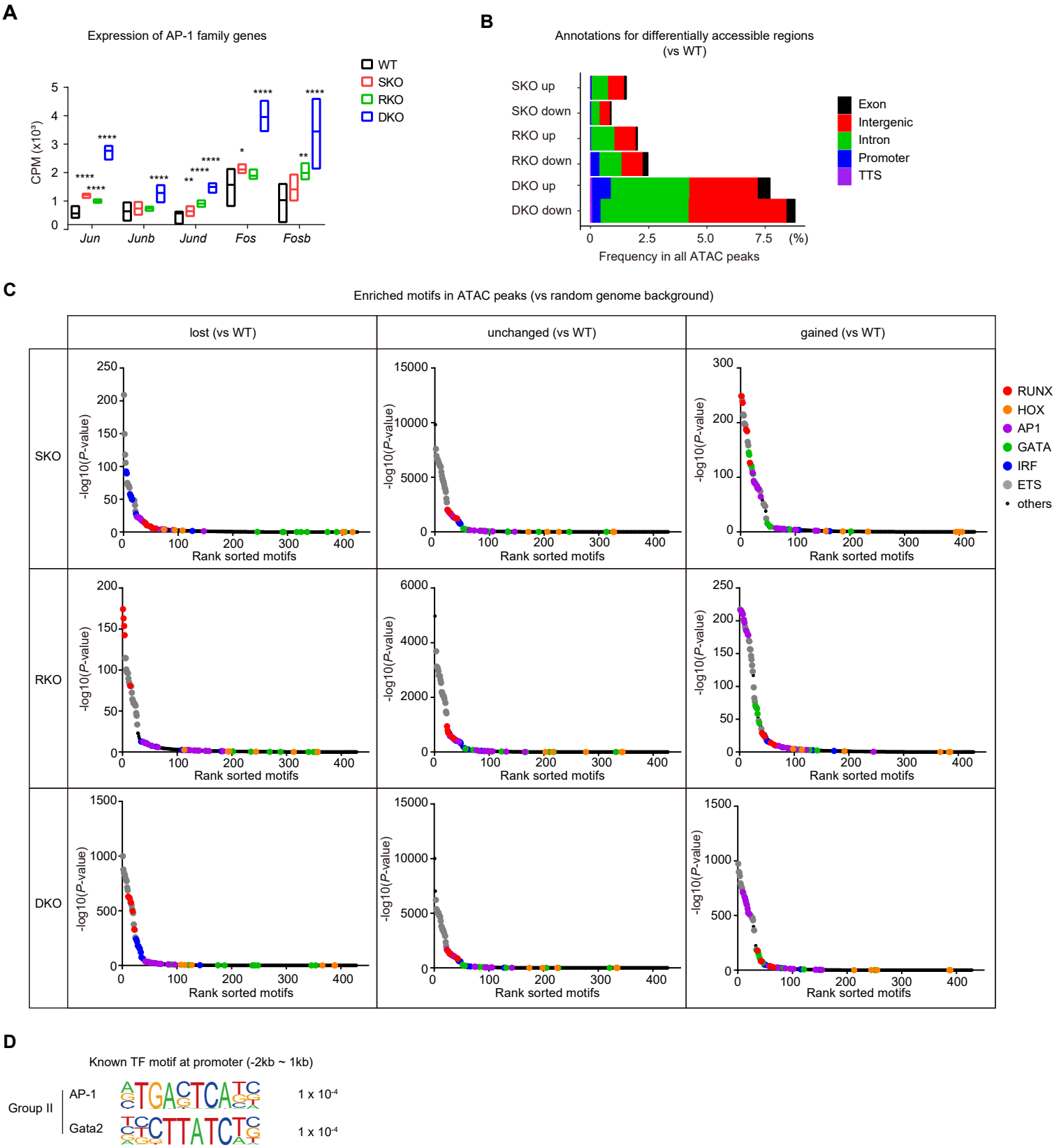
A
Expression of AP-1 family genes
WT
SKO
RKO
DKO
CPM (x10³)
Jun
Junb
Jund
Fos
Fosb
B
Annotations for differentially accessible regions (vs WT)
SKO up
SKO down
RKO up
RKO down
DKO up
DKO down
Exon
Intergenic
Intron
Promoter
TTS
Frequency in all ATAC peaks
C
Enriched motifs in ATAC peaks (vs random genome background)
lost (vs WT)
unchanged (vs WT)
gained (vs WT)
SKO
RKO
DKO
-log10(P-value)
Rank sorted motifs
RUNX
HOX
AP1
GATA
IRF
ETS
others
D
Known TF motif at promoter (-2kb ~ 1kb)
Group II
AP-1
1 x 10⁻⁴
Gata2
1 x 10⁻⁴

Supplementary Figure 12. Analysis of ATAC-seq in Stag2/Runx1 deficient HSPCs.

A, Expression of AP-1 family genes in LSK cells as indicated by CPM (min to max values with mean, n = 6 for WT and 3 for the others), in which *P*-values (vs WT) were calculated with edgeR package. **B**, Genomic annotation of differentially accessible ATAC peaks in SKO-, RKO- and DKO-derived LSK cells compared with WT. **C**, Enrichment of known TF motifs in the ATAC-seq peaks with gained, lost, or unchanged accessibility in SKO/RKO/DKO-derived LSK cells compared with WT. The sorted motif rank and –log10(*P*-value) of a motif enrichment test using random genome backgrounds is indicated in horizontal and vertical axis, respectively. **D**, Motifs and corresponding *P*-values identified by known TF motif search in the HOMER software in the promoter regions of genes in DEG group II. * $P < 0.05$; ** $P < 0.01$; *** $P < 0.001$; **** $P < 0.0001$.

A

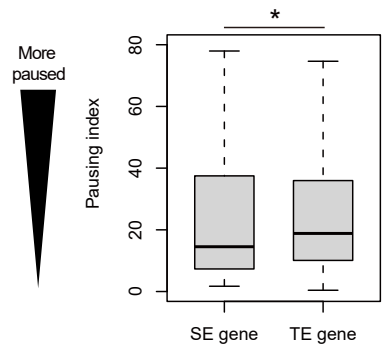
More paused
Pausing index
0
20
40
60
80
*
SE gene
TE gene

B

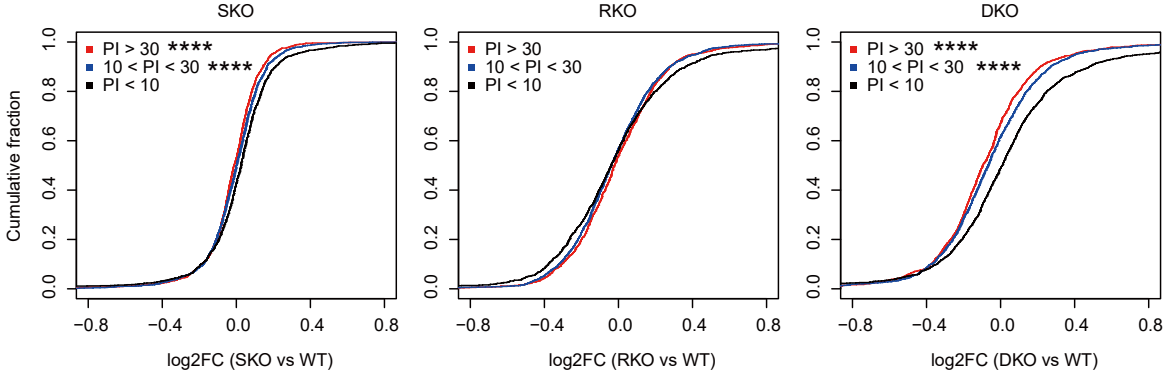
SKO
RKO
DKO
PI > 30 ****
10 < PI < 30 ****
PI < 10
Cumulative fraction
log2FC (SKO vs WT)
log2FC (RKO vs WT)
log2FC (DKO vs WT)

C

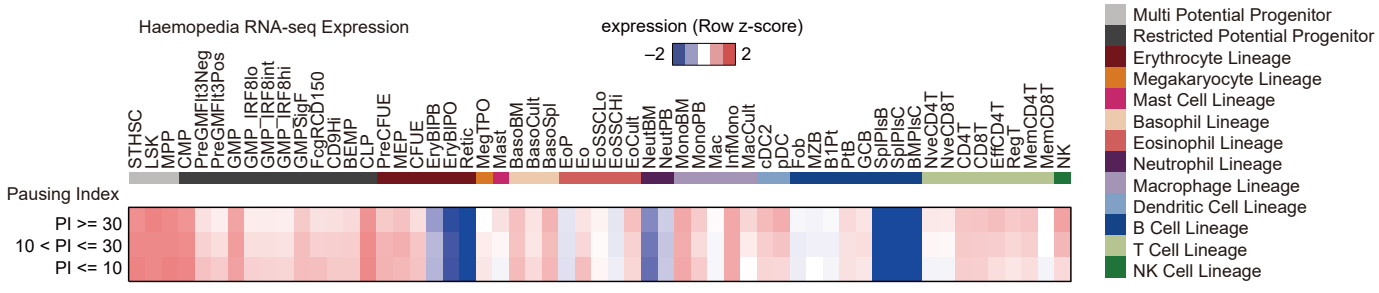
Haemopedia RNA-seq Expression
expression (Row z-score)
−2
2
STHSC
LSK
MPP
CMP
PreGMFlt3Neg
PreGMFlt3Pos
GMP
GMP_IRF8lo
GMP_IRF8int
GMP_IRF8hi
GMPSigF
FcgRCD150
CD9Hi
BEMP
CLP
PreCFUE
MEP
CFUE
EryBlPB
EryBlPO
Retic
MegTPO
Mast
BasoBM
BasoCult
BasoSpl
EoP
Eo
EoSSCLo
EoSSCHi
EoCult
NeutBM
NeutPB
MonoBM
MonoPB
Mac
InfMono
MacCult
cDC2
pDC
Fob
MZB
B1Pt
PtB
GCB
SplPlsB
SplPlsC
BMPlsC
NveCD4T
NveCD8T
CD4T
CD8T
EffCD4T
RegT
MemCD4T
MemCD8T
NK
Pausing Index
PI >= 30
10 < PI <= 30
PI <= 10
Multi Potential Progenitor
Restricted Potential Progenitor
Erythrocyte Lineage
Megakaryocyte Lineage
Mast Cell Lineage
Basophil Lineage
Eosinophil Lineage
Neutrophil Lineage
Macrophage Lineage
Dendritic Cell Lineage
B Cell Lineage
T Cell Lineage
NK Cell Lineage

Supplementary Figure 13. Analysis of Pol II pausing and expression in Stag2/Runx1 deficient HSPCs. **A**, Pausing indices of SE-associated genes and TE-associated genes. Note that SE-associated genes show lower degrees of promoter-proximal pausing consistent with the highly active status of transcription. *P*-value was calculated by one-sided Wilcoxon rank-sum test. **B,** Cumulative probability distributions of expression changes (log2FC) of genes grouped by Pol II pausing indices in SKO/RKO/DKO compared with WT. *P*-values (vs genes with PI no more than 10) were calculated by one-sided Wilcoxon rank-sum test. **C**, Expression specificity of genes classified by Pol II pausing indices across diverse hematopoietic lineages. Average expression levels of genes in the indicated groups in each hematopoietic lineage are shown. Mouse expression datasets of diverse hematopoietic lineages are from Haemopedia RNA-seq datasets. Color scales are normalized along each row.

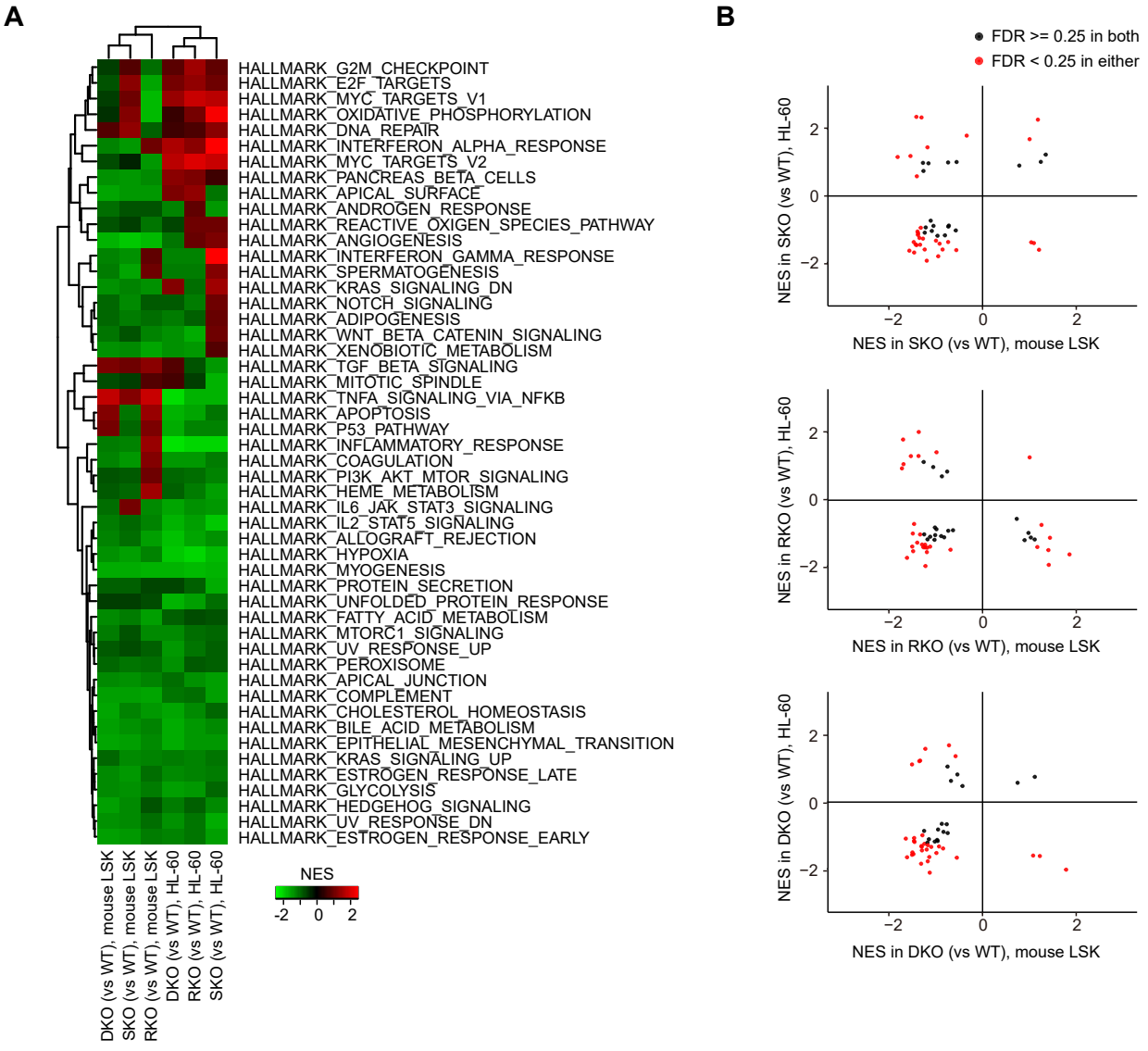
A
HALLMARK_G2M_CHECKPOINT
HALLMARK_E2F_TARGETS
HALLMARK_MYC_TARGETS_V1
HALLMARK_OXIDATIVE_PHOSPHORYLATION
HALLMARK_DNA_REPAIR
HALLMARK_INTERFERON_ALPHA_RESPONSE
HALLMARK_MYC_TARGETS_V2
HALLMARK_PANCREAS_BETA_CELLS
HALLMARK_APICAL_SURFACE
HALLMARK_ANDROGEN_RESPONSE
HALLMARK_REACTIVE_OXIGEN_SPECIES_PATHWAY
HALLMARK_ANGIOGENESIS
HALLMARK_INTERFERON_GAMMA_RESPONSE
HALLMARK_SPERMATOGENESIS
HALLMARK_KRAS_SIGNALING_DN
HALLMARK_NOTCH_SIGNALING
HALLMARK_ADIPOGENESIS
HALLMARK_WNT_BETA_CATENIN_SIGNALING
HALLMARK_XENOBIOTIC_METABOLISM
HALLMARK_TGF_BETA_SIGNALING
HALLMARK_MITOTIC_SPINDLE
HALLMARK_TNFA_SIGNALING_VIA_NFKB
HALLMARK_APOPTOSIS
HALLMARK_P53_PATHWAY
HALLMARK_INFLAMMATORY_RESPONSE
HALLMARK_COAGULATION
HALLMARK_PI3K_AKT_MTOR_SIGNALING
HALLMARK_HEME_METABOLISM
HALLMARK_IL6_JAK_STAT3_SIGNALING
HALLMARK_IL2_STAT5_SIGNALING
HALLMARK_ALLOGRAFT_REJECTION
HALLMARK_HYPOXIA
HALLMARK_MYOGENESIS
HALLMARK_PROTEIN_SECRETION
HALLMARK_UNFOLDED_PROTEIN_RESPONSE
HALLMARK_FATTY_ACID_METABOLISM
HALLMARK_MTORC1_SIGNALING
HALLMARK_UV_RESPONSE_UP
HALLMARK_PEROXISOME
HALLMARK_APICAL_JUNCTION
HALLMARK_COMPLEMENT
HALLMARK_CHOLESTEROL_HOMEOSTASIS
HALLMARK_BILE_ACID_METABOLISM
HALLMARK_EPITHELIAL_MESENCHYMAL_TRANSITION
HALLMARK_KRAS_SIGNALING_UP
HALLMARK_ESTROGEN_RESPONSE_LATE
HALLMARK_GLYCOLYSIS
HALLMARK_HEDGEHOG_SIGNALING
HALLMARK_UV_RESPONSE_DN
HALLMARK_ESTROGEN_RESPONSE_EARLY
DKO (vs WT), mouse LSK
SKO (vs WT), mouse LSK
RKO (vs WT), mouse LSK
DKO (vs WT), HL-60
RKO (vs WT), HL-60
SKO (vs WT), HL-60
NES
-2 0 2
B
FDR >= 0.25 in both
FDR < 0.25 in either
NES in SKO (vs WT), HL-60
NES in SKO (vs WT), mouse LSK
NES in RKO (vs WT), HL-60
NES in RKO (vs WT), mouse LSK
NES in DKO (vs WT), HL-60
NES in DKO (vs WT), mouse LSK

Supplementary Figure 14. Transcriptome analysis in HL-60 cell lines and mouse LSK cells.

A, Heatmap of NES values in GSEA analysis of SKO/RKO/DKO-mouse LSK cells or HL-60 cell lines compared with WT using hallmark gene sets. **B**, Scatterplots of NES values comparing SKO/RKO/DKO with WT in HL-60 cell lines and mouse LSK cells. Gene sets with FDR < 0.25 in either HL-60 cell lines or mouse LSK cells are indicated in red color.

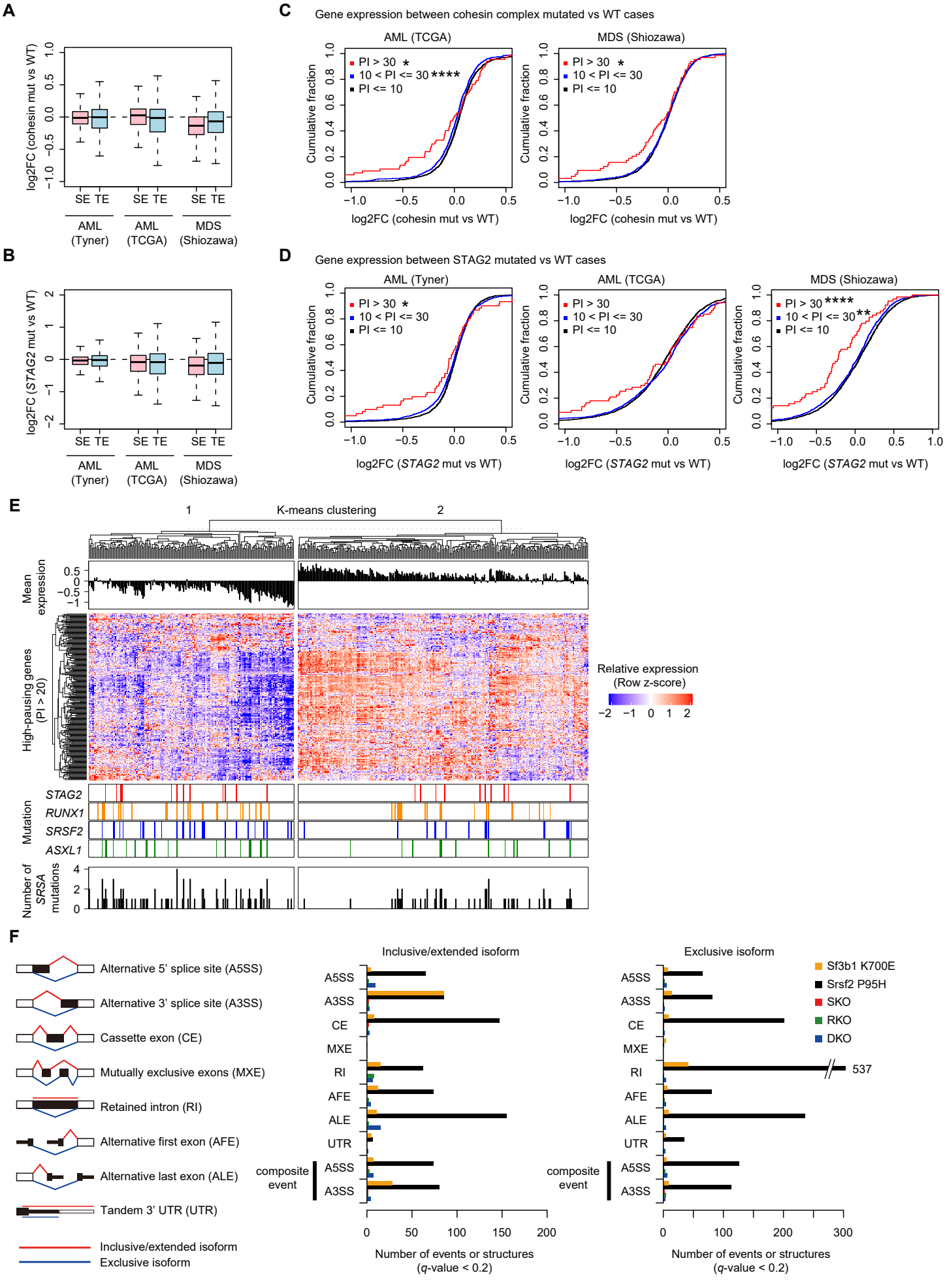
A
log2FC (cohesin mut vs WT)
SE TE SE TE SE TE
AML (Tyner)
AML (TCGA)
MDS (Shiozawa)
B
log2FC (STAG2 mut vs WT)
C
Gene expression between cohesin complex mutated vs WT cases
AML (TCGA)
MDS (Shiozawa)
PI > 30 *
10 < PI <= 30 ****
PI <= 10
Cumulative fraction
log2FC (cohesin mut vs WT)
D
Gene expression between STAG2 mutated vs WT cases
AML (Tyner)
AML (TCGA)
MDS (Shiozawa)
PI > 30 ****
10 < PI <= 30 **
log2FC (STAG2 mut vs WT)
E
K-means clustering
1
2
Mean expression
High-pausing genes (PI > 20)
Relative expression (Row z-score)
Mutation
STAG2
RUNX1
SRSF2
ASXL1
Number of SRSA mutations
F
Alternative 5' splice site (A5SS)
Alternative 3' splice site (A3SS)
Cassette exon (CE)
Mutually exclusive exons (MXE)
Retained intron (RI)
Alternative first exon (AFE)
Alternative last exon (ALE)
Tandem 3' UTR (UTR)
Inclusive/extended isoform
Exclusive isoform
Inclusive/extended isoform
Exclusive isoform
A5SS
A3SS
CE
MXE
RI
AFE
ALE
UTR
composite event
Number of events or structures (q-value < 0.2)
537
Sf3b1 K700E
Srsf2 P95H
SKO
RKO
DKO

Supplementary Figure 15. An association between cohesin mutation and Pol II pausing in human MDS/AML and analysis of alternative splicing events in Stag2/Runx1 deficient LSK cells.

A-B, Box plots showing expression changes of SE- and TE-associated genes identified in human CD34-positive HSPCs in cohesin (**A**) or *STAG2*-mutated (**B**) cases compared with WT cases in RNA-seq datasets from three independent MDS/AML cohorts. The vertical axis represents the log2(FC) in the indicated gene sets. **C-D**, Cumulative probability distributions of expression changes (log2FC) of genes grouped by pausing indices in cohesin-mutated cases (vs WT) (**C**) or *STAG2*-mutated cases (vs WT) (**D**) in RNA-seq datasets of MDS (Shiozawa et al., 2017) and AML (Ley et al., 2013; Tyner et al., 2018). *P*-values (vs genes with PI no more than 10) were calculated by one-sided Wilcoxon rank-sum test. **E**, K-means clustering analysis of RNA-seq dataset of AML (Tyner et al., 2018) using expression of genes with PI >20. Each row and column represent each gene and case, respectively. The Color scales are normalized along each row. Mean expression of genes (PI >20) is shown in the above of the heatmap, and presence or absence of each mutation and number of SRSA mutations are shown in the below. **F**, Numbers of alternative splicing events identified between SKO/RKO/DKO-derived LSK cells and WT cells. Numbers of alternative splicing events identified in cells having Sf3b1 K700E and Srsf2 P95H, major mutations in splicing factors, are also shown. * $P < 0.05$; ** $P < 0.01$; *** $P < 0.001$; **** $P < 0.0001$.

Inventory of Supplementary Tables

Supplementary Table S1. Diagnosis of patients with MDS/AML in correlation analysis.

Supplementary Table S2. Characteristics of MDS patients with STAG2, RUNX1, SRSF2, and/or ASXL1 mutations.

Supplementary Table S3. Correlations between mutations in patients with MDS/AML.

Supplementary Table S4. The antibodies used in the FACS experiments.

Supplementary Table S5. sgRNA sequences used for gene knockout and PCR primers for confirmation.

Supplementary Table S6. Genotypes of CRISPR-KO HL-60 clones.

Supplementary Table S7. Mutations in human MDS/AML RNA-seq datasets.

Supplementary Table S8. Up-regulated genes in RNA-seq of SKO LSK cells (vs WT, edgeR; FDR < 0.05).

Supplementary Table S9. Down-regulated genes in RNA-seq of SKO LSK cells (vs WT, edgeR; FDR < 0.05).

Supplementary Table S10. Up-regulated genes in RNA-seq of SKO LSK cells in BMT experiments (vs WT, edgeR; FDR < 0.05).

Supplementary Table S11. Down-regulated genes in RNA-seq of SKO LSK cells in BMT experiments (vs WT, edgeR; FDR < 0.05).

Supplementary Table S12. Up-regulated genes in RNA-seq of RKO LSK cells in BMT experiments (vs WT, edgeR; FDR < 0.05).

Supplementary Table S13. Down-regulated genes in RNA-seq of RKO LSK cells in BMT experiments (vs WT, edgeR; FDR < 0.05).

Supplementary Table S14. Up-regulated genes in RNA-seq of DKO LSK cells in BMT experiments (vs WT, edgeR; FDR < 0.05).

Supplementary Table S15. Down-regulated genes in RNA-seq of DKO LSK cells in BMT experiments (vs WT, edgeR; FDR < 0.05).

Supplementary Table S16. Gained peaks in ATAC-seq of SKO LSK cells (vs WT, edgeR; FDR < 0.05).

Supplementary Table S17. Lost peaks in ATAC-seq of SKO LSK cells (vs WT, edgeR; FDR < 0.05).

Supplementary Table S18. Gained peaks in ATAC-seq of SKO CMP cells (vs WT, edgeR; FDR < 0.05).

Supplementary Table S19. Lost peaks in ATAC-seq of SKO CMP cells (vs WT, edgeR; FDR < 0.05).

Supplementary Table S20. Super-enhancers of mouse HSPCs identified using H3K27ac ChIP-seq of WT HSPCs.

Supplementary Table S21. Information about the external ChIP-seq datasets used in this study.